

MASTERARBEIT
im Studiengang *Physik*

Renormalization group analysis
of momentum-dependent four-fermion interactions

Lennart Dabelow
15. September 2017

Überarbeitete Fassung vom 24. Oktober 2017



FRIEDRICH-SCHILLER-
UNIVERSITÄT
JENA

Renormalization group analysis of momentum-dependent four-fermion interactions

Using functional renormalization group methods, we investigate (2+1)-dimensional relativistic fermion systems with momentum-dependent couplings, which serve as effective theories in condensed matter or as toy models in high-energy physics. While derivative expansions of such models with pointlike interactions have been studied extensively in the literature, little is known about the vertex functions' momentum dependence. After a general analysis of momentum-dependent flow equations, we work out dominant interaction channels and determine renormalization group fixed points and critical exponents of Gross-Neveu- and Thirring-type models using pseudospectral methods. In the limit of infinite flavor number, we can even derive an analytic solution. The observed fixed point structure is qualitatively similar to the pointlike limit, but shows clear indications for the importance of momentum dependence for small flavor numbers. We also compare our findings quantitatively to previous results obtained by different approaches.

Mittels Methoden der funktionalen Renormierungsgruppe untersuchen wir (2+1)-dimensionale, relativistische Fermion-Systeme mit impulsabhängigen Kopplungen. Diese dienen als effektive Theorien in Modellen der kondensierten Materie oder als Spielzeugmodelle in der Hochenergiephysik. Während Ableitungsentwicklungen solcher Modelle mit punktförmigen Wechselwirkungen in der Literatur bereits ausgiebig studiert wurden, ist über die Impulsabhängigkeit der Vertex-Funktionen wenig bekannt. Nach einer allgemeinen Analyse impulsabhängiger Flussgleichungen arbeiten wir dominante Wechselwirkungskanäle heraus und bestimmen Renormierungsgruppen-Fixpunkte und kritische Exponenten von Gross-Neveu- und Thirring-artigen Modellen mittels pseudospektraler Methoden. Im Limes unendlicher Flavor-Zahl leiten wir eine analytische Lösung her. Die beobachtete Fixpunktstruktur ist qualitativ ähnlich derjenigen im punktförmigen Limes, zeigt jedoch klare Anzeichen für die Wichtigkeit von Impulsabhängigkeiten bei kleinen Flavor-Zahlen. Ebenso vergleichen wir unsere Ergebnisse quantitativ mit durch andere Herangehensweisen erhaltenen, früheren Resultaten.

Abschlussarbeit im Studiengang *Physik*

zur Erlangung des akademischen Grades
Master of Science (M.Sc.)

eingereicht am 15. September 2017

von

B.Sc. Lennart Justin Dabelow

geboren am 04.06.1992 in Gießen

lennart.dabelow@uni-jena.de

Matrikelnr.: 128 530

Gutachter:

1. Prof. Dr. Holger Gies / TPI
2. Dr. Omar Zanusso / TPI

Ich versichere, dass ich vorliegende Masterarbeit selbstständig und nur unter Verwendung der angegebenen Hilfsmittel und Quellen verfasst sowie Zitate und gedankliche Übernahmen kenntlich gemacht habe. Die Arbeit ist nicht anderweitig als Prüfungsleistung verwendet und nicht in englischer oder einer anderen Sprache veröffentlicht worden.

Jena, 15. September 2017

Lennart Dabelow

Contents

Introduction	5
1 Renormalization group flow	7
1.1 Quantum field theory	7
1.2 Functional renormalization group	8
1.3 Fixed points, universality, and asymptotic safety	11
2 Momentum-dependent four-fermion vertices	15
2.1 Symmetries and Fierz transformations	15
2.2 Flow equations for the coupling functions	17
2.3 Anomalous dimension function	23
3 Gross-Neveu model	25
3.1 Flow of the four-point function	25
3.2 Partial bosonization	26
3.3 <i>s</i> -Channel approximation	28
3.4 Large- N_f limit	31
3.5 Fixed points for finite flavor numbers	34
3.6 Spectrum of the nontrivial fixed point	41
4 Thirring model	48
4.1 Flow of the coupling functions	48
4.2 Limiting cases	49
4.3 Finite- N_f fixed points and spectra	52
4.4 Connection to the bosonized formulation	59
5 Conclusions	61
Acknowledgments	65
A Abbreviations and conventions	66
B Computational details	69
B.1 Gamma matrices	69
B.2 Loop integrals with spherical symmetry	70
B.3 Flow equations	70
B.4 Anomalous dimension function	73
B.5 Gross-Neveu model	73
B.6 Gross-Neveu-Thirring model	75
C Chebyshev functions and the pseudospectral method	78
C.1 Chebyshev polynomials of the first kind	78
C.2 Chebyshev polynomials of the second kind	79
C.3 Chebyshev rational functions	79
D Newton-Raphson iteration	81
E Remarks on the source code	83
E.1 Compiling and running the program	83
E.2 Auxiliary libraries	84
E.3 File structure	85
E.4 Interactive computing script interface	87
E.5 Example scripts	95
References	97

Introduction

If you will, this thesis is a study of elementary particle billiards. The game of billiards is a classical example of a momentum-dependent four-body interaction: Its fundamental process involves two incoming balls or *particles* with momenta p_1 and p_2 that collide and separate again with momenta p'_1 and p'_2 as illustrated in Fig. 1a. Besides the balls' momenta, the interaction generally depends on other internal degrees of freedom such as the types of balls colliding or their angular momenta. To model the game mathematically, we can parametrize the intensity of the interaction as a function of the configuration of balls in much the same way as we will do in the case of more fundamental particles later in this work.

The billiards picture can serve to illustrate other aspects of the intended analysis, too, namely the influence of fluctuations and the separation of scales. In order to make predictions about the behavior of a physical system such as our billiard balls, it usually suffices to consider fluctuations on the order of the typical scales of its constituents, say millimeters to meters in our example. Neither do we need to take care of all the individual atoms and molecules that make up the balls and keep track of their complicated interactions, nor do the location of our pool table on the surface of the earth or the earth's relative position in the solar system matter to describe the game's dynamics. Then again, a strong gust of wind or bumps in the table's surface will change these dynamics significantly.

The idea of the renormalization group (RG), the underlying toolkit of our investigation, is to study the effect of fluctuations scale by scale and to systematically coarsen the description by averaging them out. This allows one to keep track of the relevant degrees of freedom in a natural way, in principle connecting, *e.g.*, molecules to billiard balls, although there are practical limitations. The generality of this framework renders it useful in a variety of contexts with applications found in quantum field theory, statistical physics, fluid dynamics, and more [1–3]. Of great theoretical importance is the explanation the RG offers for the phenomenon of universality, the observation that very distinct physical systems may exhibit similar macroscopic properties irrespective of their microscopic structure and dynamics. A prominent example are phase transitions in thermodynamics and quantum physics [2].

The functional RG (FRG) in particular additionally provides a refreshing view on the historically awkward renormalization procedure in quantum field theories. In this regard, it naturally explains emerging divergences and ways to deal with them, and also clarifies why physical theories are usually described by a relatively small number of important parameters. Not least, it extends our understanding of renormalizability and enables new, nonperturbative ways of renormalization by means of the asymptotic safety scenario [4], potentially permitting, *e.g.*, to renormalize quantum gravity [5], a long-standing problem on the way towards a joint description of fundamental forces.

This brings us to the multifarious world of elementary particles, whose typical scales are more than 15 orders of magnitude smaller than those of classical billiards. The to date most precise description of those fundamental constituents of matter and their interactions is provided by the Standard Model [1, 6, 7], which at the lowest level distinguishes two types of particles, bosons and fermions. Both of these are classified into further subgroups, but for the time being we shall be content with the observation that fermions are the elementary building blocks of matter and

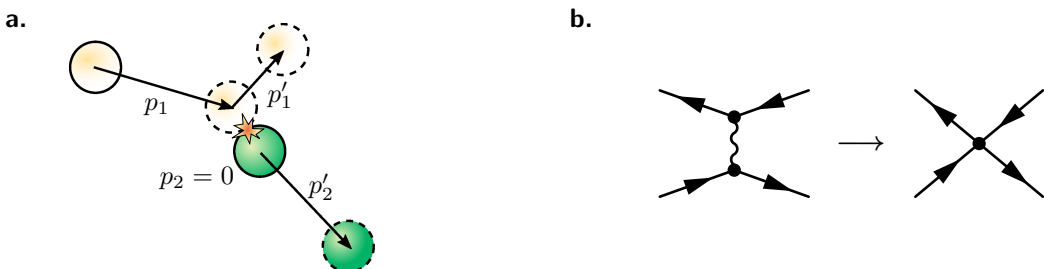


Figure 1: (a) Illustration of a four-body interaction; (b) four-fermion scattering mediated by an exchange particle and the corresponding effective vertex, where the dynamics of the exchange particle are neglected.

bosons mediate the interactions between them or, in case of the Higgs, generate masses for other elementary particles.

While the Standard Model itself does not know any direct four-fermion interactions, such models are used as effective theories in various fields whenever the dynamics of the exchange particle can be neglected, sketched in Fig 1b. Examples include many condensed matter systems such as conventional superconductors [8] and trapped atomic gases [9], precursors of the weak interaction [10, 11], or low-energy models of quantum chromodynamics (QCD), the theory of strong interactions [12–14]. In this work, we will be mostly dealing with relativistic fermion systems in (2+1) spacetime dimensions, which describe, *e.g.*, electrons in graphene [15–20] or cuprates [21–23], or provide toy models for asymptotic safety scenarios and spontaneous chiral symmetry breaking in high-energy physics [24–33].

Regarding graphene, for instance, a tight-binding approximation with one mobile electron per carbon atom leads to a linear dispersion relation for low-energy excitations at two independent Dirac points [16, 34, 35] where the electrons are effectively massless and relativistic even though the Fermi velocity $v_F \approx c/300$ is two orders of magnitude smaller than the speed of light [16]. The latter fact implies that the electron–electron interaction mediated by photons is essentially instantaneous. Moreover, and despite the relatively small fine-structure constant $\alpha \simeq 1/137$ that governs the strength of the electronic interactions, it means that the effective coupling $\alpha_{\text{eff}} = \alpha c/v_F$ is of order one, reinforcing the need for a nonperturbative computation scheme. Besides such concrete applications, models of four-fermion interactions are also intrinsically interesting due to a surprisingly rich phenomenology despite their (superficial) theoretical simplicity. One aspect concerns the already mentioned spontaneous symmetry breaking and the dynamical generation of fermion masses in originally massless theories.

In the main part of this thesis, we will be investigating two specific, popular models of four-fermion interactions, the Gross-Neveu [14] and Thirring [36] models. Both have been the subject of numerous studies before, using various approaches such as perturbation theory [37–44], Dyson-Schwinger equations [24, 45, 46], lattice simulations [25, 28, 29, 33, 47–55], conformal bootstrap [56–59], and the FRG [26, 27, 30–32, 60, 61]. Nevertheless, and in particular for small flavor numbers, *i.e.* systems with only few types of different fermions, no consensus has yet been reached about some of their properties like critical exponents or the formation of fermion condensates. These questions will be part of our investigation.

The principle purpose of this work, however, is to gain a deeper insight into the momentum dependence of interactions in these models. Most studies, especially the FRG approaches examined so far, employed momentum-independent, pointlike interactions between the participating particles. Some of the momentum dependence can then be restored by derivative expansions or bosonization techniques, but it is not *a priori* clear whether these truncations cover all essential effects. As the momentum dependence is expected to become increasingly important for small flavor numbers, we will take a different approach here and incorporate the momenta of the interacting particles directly in the coupling functions characterizing the interaction strength. This strategy has been employed for related nonrelativistic condensed matter systems [62–65], but for relativistic fermions, although first steps in this direction can be found in the literature [66], the present work is the first extensive study of vertex expansions for these models. Comparing to previous results will allow us to work out the strengths and weaknesses of this approach and to extend the understanding of four-fermion theories.

* * *

The thesis is organized as follows. In Section 1 we will begin with a compilation of general notions and concepts about quantum field theories and the functional renormalization group that are relevant for the ensuing analysis. Section 2 will then kick off the study of momentum-dependent four-fermion interactions from a rather abstract perspective. In particular, we will present a general derivation of renormalization group flow equations for arbitrary momentum-dependent four-fermion vertices and identify occurring interaction channels. Thereafter, we will turn to the two aforementioned and related models, namely the Gross-Neveu model in Section 3 and the Thirring model in Section 4. In both cases, we will analyze the RG flow of these systems in a momentum-dependent setting. Finally, we will summarize and assess our findings in Section 5.

1 Renormalization group flow

Generally speaking, the *renormalization group* (RG) is a concept to explore fluctuations in the parameters of physical systems at various length or energy scales. The *functional renormalization group* (FRG) offers a toolkit to systematically conduct this analysis for systems described by field theories. In the context of quantum field theory, it allows us to study the influence of quantum fluctuations on the interactions between fundamental particles. The aim of this section is to collect the essential results that the subsequent sections of this thesis are based upon. Details and derivations can be found in numerous reviews and books on the topic [3, 63, 67–72].

1.1 Quantum field theory

To motivate the key quantities of the FRG formalism, let us begin by introducing some basic notions of field theory.

Particles and interactions. As far as we know today, quantum field theories provide the most fundamental description of the dynamics and interactions of elementary and composite particles. These basic degrees of freedom are encoded in *fields*, which link spacetime to an abstract mathematical space or, more colloquially, a set of numbers, and whose excitations describe the actual particles. There are two types of fields to be distinguished at the fundamental level. *Bosons*, on the one hand, take real or complex values, have integer spin, and satisfy Bose-Einstein statistics [73–75]. *Fermions*, on the other hand, are anticommuting in character, reflecting Fermi-Dirac statistics and half-integer spin [73–75]. In $d = (2+1)$ spacetime dimensions, *anyons* with arbitrary nonnegative spin quantum number generalize this classification in principle [76, 77], but will not be of concern for our investigations.

At high energy scales, on the level of elementary particles as described by the Standard Model, the constituents of matter are all fermions whereas their interactions are mediated by bosons. However, this differentiation becomes blurry as soon as one considers lower energies and effective theories, where an even number of fermions may form a bosonic bound state (or a rigid billiard ball) and interactions need not necessarily involve an exchange of bosons. In particular, this is the typical case in condensed matter systems where energies are naturally much lower than in particle physics.

Let us consider a generic quantum field $\Phi = \Phi(x)$ that may contain both bosonic and fermionic degrees of freedom. A field-theoretic model of these is specified by an *action* $S[\Phi]$ which details the dynamics of the individual constituents as well as the allowed interaction processes between them. An example is the *Gross-Neveu-Yukawa model*, which we will re-encounter in Section 3.2. It features a scalar bosonic field ϕ and two fermionic fields ψ and $\bar{\psi}$, *i.e.* $\Phi = (\phi, \psi^\top, \bar{\psi})^\top$. The action reads

$$S[\Phi] = \int d^d x \left[\frac{1}{2} \partial_\mu \phi(x) \partial^\mu \phi(x) + \frac{1}{2} \bar{m}^2 \phi(x)^2 + \bar{\psi}(x) i \not{\partial} \psi(x) + i \bar{h} \phi(x) \bar{\psi}(x) \psi(x) \right]. \quad (1.1)$$

The first two terms describe the dynamics of the boson, the third term covers the fermion dynamics. The last term describes an interaction between the boson and the two fermions, for instance allowing a boson to decay into a fermion and an antifermion. Note also that we will be working in natural units with $\hbar = c = 1$ throughout this thesis, so that actions are dimensionless and the dimensions of mass, energy, or momentum are reciprocal to those of time and length.

Correlation functions and effective action. Eventually, a physical theory is supposed to make predictions about actual phenomena and processes in nature. Examples of such predictions are cross sections of scattering experiments, decay rates of certain particles to others, or phase diagrams and classifications of phase transitions. All this information is naturally encoded in the *correlation functions* [1, 2, 68, 75], which can be computed as a (regularized) path integral over all possible configurations of the fields,

$$\langle \Phi_{\alpha_1}(x_1) \cdots \Phi_{\alpha_n}(x_n) \rangle = \frac{\int \mathcal{D}\Phi \Phi_{\alpha_1}(x_1) \cdots \Phi_{\alpha_n}(x_n) e^{-S[\Phi]}}{\int \mathcal{D}\Phi e^{-S[\Phi]}}. \quad (1.2)$$

The index α here labels the individual constituents of the collective field variable Φ . We remark that we will be working exclusively in the *Euclidean* formalism as indicated by the real exponential weight factor above. The spacetime metric is thus $\delta_{\mu\nu}$, which has an all-positive signature as opposed to the metric of real-world spacetime. The components of Euclidean spacetime points, vectors, *etc.* are labeled by Greek indices $\mu, \nu, \dots \in \{1, \dots, d\}$. Analytic continuation from Euclidean to Minkowski space is in principle possible by a *Wick rotation* mapping the Minkowski time $t \equiv x^0$ onto Euclidean time $\tau \equiv x^d = -it$ [78]. We will assume that this is also practically possible in the cases studied throughout this thesis. The generating functional

$$\mathcal{Z}[J] := \int \mathcal{D}\Phi e^{-S[\Phi] + \int d^d x J(x)^\top \Phi(x)} \quad (1.3)$$

can be used to compute correlation functions by functional differentiation with respect to the source field J . Directly related to \mathcal{Z} is the Schwinger functional $\mathcal{W}[J] := \ln \mathcal{Z}[J]$, whose derivatives generate the *connected* correlation functions [1].

A more efficient storage of physical information, however, is the *effective action*, defined as the Legendre transform of the Schwinger functional,

$$\Gamma[\Phi_{\text{cl}}] := \sup_J \left(\int d^d x J(x)^\top \Phi_{\text{cl}}(x) - \mathcal{W}[J] \right). \quad (1.4)$$

The relevance of the effective action stems from its direct connection to experimentally accessible quantities because its derivatives include all quantum fluctuations: The first functional derivative yields the equations of motion for the vacuum expectation values, which also explains the label Φ_{cl} standing for the *classical field*. The second derivative gives the full inverse propagators of the constituent fields, and higher order derivatives generate the full one-particle irreducible vertices, which are precisely the matrix elements entering the computation of scattering amplitudes and the like [1]. Unfortunately, a direct calculation of the generating functional (1.3) and its Legendre transform (1.4) is virtually impossible in all but very special cases (*e.g.* free theories where $\Gamma = S$). In practice, we thus have to find other approaches or approximations to access the effective action. The historically first and to date most precise calculations of, *e.g.*, scattering cross sections are based on *perturbation theory*. Here the idea is to expand the effective action around the free theory by assuming interaction terms to be sufficiently small [1, 75]. Unfortunately, this formalism is doomed to break down for strongly interacting systems. A different approach is offered by the FRG, which provides a systematic way to interpolate between a bare, microscopic action like (1.1) and the associated effective action.

1.2 Functional renormalization group

The bare action S describes a classical theory we wish to quantize. It is related to some fundamental high energy scale Λ up to which fluctuations are to be included, *e.g.* the Planck energy in particle physics or the inverse lattice spacing in condensed matter. The underlying idea of the RG as first systematically developed by Kadanoff [79] and Wilson [80] is to integrate out these fluctuations step-by-step and establish a continuous transformation from the microscopic level to the effective theory.

Effective average action. To this end, we introduce a momentum scale k that keeps track of our progress in integrating out fluctuations. Our aim is to define an *effective average action* $\Gamma_k[\Phi_{\text{avg}}]$ that includes fluctuations with $p^2 \gtrsim k^2$ [81, 82], such that it interpolates between the bare action S at $k = \Lambda$ and the full effective action Γ at $k = 0$. Hence its argument, the field Φ_{avg} , is a classical field for momenta $p^2 \gtrsim k^2$. In the following, we will drop the label ‘avg’ on the argument of Γ_k again. The idea to achieve this effect is to supplement the action with a momentum- and scale-dependent term quadratic in the fields,

$$\Delta S_k[\Phi] := \frac{1}{2} \int \frac{d^d p}{(2\pi)^d} \Phi(-p)^\top \mathcal{R}_k(p) \Phi(p), \quad (1.5)$$

in the definition of the Schwinger functional. Pictorially speaking, the *regulator* \mathcal{R}_k is to add a mass of order k to the low-energy modes with $p^2 \lesssim k^2$ to decouple them from the high-energy modes. The additional term renders the Schwinger functional scale-dependent, too:

$$e^{\mathcal{W}_k[J]} := \int \mathcal{D}\Phi e^{-S[\Phi] - \Delta S_k[\Phi] + \int_p J(-p)^\top \Phi(p)}. \quad (1.6)$$

Note that we changed to momentum space in the above expression for convenience. Our conventions for Fourier transformations can be found in Appendix A. The shorthand $\int_p \equiv \int \frac{d^d p}{(2\pi)^d}$ is understood. Regarding the momentum dependence of collective fields containing Hermitian or Grassmann conjugates, we follow the conventions of Ref. [72], namely $\Phi(p) := (\phi(p), \psi(p)^\top, \bar{\psi}(-p)^\top)^\top$. The effective average action is then defined as a modified Legendre transform of \mathcal{W}_k [68, 72, 82],

$$\Gamma_k[\Phi] := \sup_J \left(\int_p J(-p)^\top \Phi(p) - \mathcal{W}_k[J] \right) - \Delta S_k[\Phi]. \quad (1.7)$$

Regulators. To ensure that Γ_k has the desired properties, the regulator must satisfy three conditions [67, 68, 72],

$$\lim_{p^2/k^2 \rightarrow 0} \mathcal{R}_k(p) > 0, \quad \lim_{k^2/p^2 \rightarrow 0} \mathcal{R}_k(p) = 0, \quad \text{and} \quad \lim_{k \rightarrow \Lambda} \mathcal{R}_k(p) = \infty. \quad (1.8)$$

Note that \mathcal{R}_k receives an extra minus sign for fermions in order to comply with the kinetic term in our chiral conventions, as will become clear from the explicit form below. The first condition implements the screening of low-energy modes, regularizing the functional integral in the infrared (IR). The second condition ensures the correct IR limit, $\Gamma_{k \rightarrow 0} = \Gamma$, while the third condition takes care of the ultraviolet (UV) limit, $\Gamma_{k \rightarrow \Lambda} = S$. We remark that for most common choices of \mathcal{R}_k , the latter condition is only achieved as $\Lambda \rightarrow \infty$. In general, it is also desirable that the regulator preserve the symmetries of the theory because this is expected to improve convergence of approximation schemes [68]. Due to the fact that mass terms take different forms for boson and fermion fields, we also have to use different forms of regulators for the two. Quite generally, we may choose

$$\mathcal{R}_k^\phi(p) = p^2 Z_k^\phi(p^2) r_k^{(B)}(p^2) \quad \text{and} \quad \mathcal{R}_k^\Psi(p) = - \begin{pmatrix} 0 & \Psi^\top \\ \Psi & 0 \end{pmatrix} Z_k^\Psi(p^2) r_k^{(F)}(p^2) \quad (1.9)$$

for a (scalar) bosonic field ϕ and a fermionic field $\Psi = (\psi, \bar{\psi}^\top)^\top$, respectively. Notice that we introduced and included a momentum-dependent wave function renormalization Z_k for both types of fields. We also remark that this form of the fermionic regulator preserves chiral symmetry. As for the dimensionless *regulator shape functions* $r_k^{(B)}$ and $r_k^{(F)}$, there exist plenty of popular choices in the literature. In this thesis, we will be using three different types depending on the particular problem. The linear regulator advocated by Litim [83, 84] is defined by

$$r_k^{(B)}(x) = \left(\frac{k^2}{x} - 1 \right) \Theta(k^2 - x), \quad r_k^{(F)}(x) = \left(\frac{k}{\sqrt{x}} - 1 \right) \Theta(k^2 - x). \quad (1.10)$$

Its advantage is that it allows to compute occurring integrals symbolically in many cases, thus giving access to analytic solutions. However, since it is not a smooth function of its argument, it is inconvenient in series expansions or numerical studies of momentum-dependent quantities. In these cases, we will usually implement the exponential regulator of Ref. [67] (cf. Eq. (7.22) therein),

$$r_k^{(B)}(x) = \frac{1}{e^{x/k^2} - 1}, \quad r_k^{(F)}(x) = \frac{1}{\sqrt{1 - e^{-x/k^2}}} - 1. \quad (1.11)$$

For our purposes, it proved to have sufficiently stable numerics and offered decent convergence properties. To cross-check results and estimate their regulator dependence, we also used the family of exponential regulators put forward in Ref. [61],

$$r_k^{(B)}(x) = \left(\frac{k^2}{x} \right) \frac{1}{2 \exp \left[\left(\frac{x}{k^2} \right)^\alpha \right] - 1}, \quad r_k^{(F)}(x) = \left(\frac{k}{\sqrt{x}} \right) \frac{1}{2 \exp \left[\left(\frac{x}{k^2} \right)^\alpha \right] - 1}, \quad (1.12)$$

where $\alpha > 0$ is a free parameter. In the following, we will usually omit the superscripts B or F for bosonic or fermionic regulators if there is no danger of confusion.

FRG flow equation. With all relevant quantities at hand, we can finally flesh out the interpolation that Γ_k is to provide between the microscopic and effective actions. By the very definition, every action functional is the mathematical expression of a physical system or *theory*. A successful theory should describe the relevant degrees of freedom of a system as well as their interactions. However, both the degrees of freedom and the strength of interactions may and will change as we lower the scale k from the microscopic level to experimentally accessible regimes. As an example, consider QCD. At very high energies, the dynamical fields are quarks and gluons, and their interaction becomes ever weaker with increasing energy, a phenomenon known as asymptotic freedom [85, 86]. Nevertheless, when going to lower energies, we will only observe bound states of the microscopic constituents like protons, neutrons, and pions, indicating that the relevant degrees of freedom have indeed changed. Hence the behavior at different scales will be described by different theories or, equivalently, action functionals. By continuously lowering the scale k , we thus expect the effective average action Γ_k to follow a trajectory in the space of all theories admissible by the symmetries of the system.

To explore the dynamics of this flow in theory space, one usually defines a *renormalization group time* $t := \ln(k/\Lambda)$. Differentiating the definition (1.7) with respect to t and re-expressing the right-hand side in terms of Γ_k , one can derive the Wetterich equation [82, 87–89], a flow equation for the effective average action,

$$\partial_t \Gamma_k = \frac{1}{2} \text{STr} \left[\left(\Gamma_k^{(2)} + \mathcal{R}_k \right)^{-1} \partial_t \mathcal{R}_k \right]. \quad (1.13)$$

This relation is the cornerstone of the FRG in the effective average action formulation. It is a one-loop exact functional integro-differential equation governing the transition from the microscopic action to the full effective action. By $\Gamma_k^{(2)}$ we denote the second functional derivative of Γ_k , or more precisely

$$\Gamma_k^{(2)}[\Phi](q, q') = \frac{\overrightarrow{\delta}}{\delta \Phi^\Gamma(-q)} \Gamma_k[\Phi] \frac{\overleftarrow{\delta}}{\delta \Phi(q')} \quad (1.14)$$

in momentum space, with one derivative acting from the left and one from the right [72]. The supertrace on the right-hand side of (1.13) includes the contraction of all internal field indices (*i.e.* color, flavor, Dirac, ...) as well as an operator trace, which in momentum space is a simple integral over the loop momentum. In addition, it assigns a minus sign to all anticommuting, fermionic field components.

Truncations. Although Eq. (1.13) is in principle an exact equation relating the microscopic to the effective action, it is unfortunately not exactly solvable in full generality. Nevertheless, the huge benefit of the FRG formalism is that it allows for *nonperturbative* approximation schemes, opening up whole new regions of theory space. The most common approaches to reduce complexity are the *derivative* and *vertex expansions*, both of which restrict the analysis to a subset of theories by omitting certain interaction terms.

The idea of the derivative expansion is to expand the effective average action in powers of external momenta (or derivatives in position space). For a scalar field, a typical ansatz would be

$$\Gamma_k[\phi] = \int d^d x \left[V_k(\phi) + \frac{1}{2} Z_k(\phi) (\partial_\mu \phi)^2 + \mathcal{O}(\partial^4) \right], \quad (1.15)$$

where the effective potential V_k , the wave function renormalization Z_k , and potential higher-order coefficients depend on the homogeneous field. Consequently, all interactions are local and pointlike. Concerning the fermionic systems we will be investigating in this thesis, numerous studies have constantly increased the order of derivative expansions over the past few years [26, 27, 30, 60, 61]. On the contrary, complementary vertex expansions of fermionic theories have only been investigated very little and predominantly for nonrelativistic condensed matter systems [62–65]. The application to relativistic fermions in $(2+1)$ Euclidean dimensions will be the focus of this work. In a vertex expansion, the effective average action is expanded in powers of the fields, *e.g.*

$$\Gamma_k[\phi] = \frac{1}{2} \int_p \Gamma_k^{(2)}(p) \phi(-p) \phi(p) + \frac{1}{6} \int_{p_1, p_2} \Gamma_k^{(3)}(p_1, p_2) \phi(-p_1 - p_2) \phi(p_1) \phi(p_2) + \mathcal{O}(\phi^4), \quad (1.16)$$

but the inverse propagator $\Gamma^{(2)}$ as well as the vertex functions $\Gamma_k^{(n \geq 3)}$ retain their full momentum dependence. This scheme is closely related to the method of Dyson-Schwinger equations, which essentially follow from a vertex expansion of the full effective action [90].

In practice, further approximations within either derivative or vertex expansions are common. In the derivative expansions, the coefficient functions V_k, Z_k, \dots are often truncated at some order of the fields, whereas in the vertex expansion a restriction of the vertices' momentum dependence may be employed. One problem is to find a consistent closing scheme for the infinite hierarchy of coupled integro-differential equations for the vertex functions. Ideas have been developed for bosonic systems [91–93], but are largely missing for systems with fermions, so that one usually relies on simple truncations [63].

For actual calculations using vertex expansions, it will be advantageous to decompose $\Gamma_k^{(2)} + \mathcal{R}_k$ into a field-independent part \mathcal{P}_k (“propagator”) and a field-dependent part \mathcal{F}_k , such that $\Gamma_k^{(2)} + \mathcal{R}_k = \mathcal{P}_k + \mathcal{F}_k$. We can then expand the right-hand side of Eq. (1.13) in powers of the field:

$$\partial_t \Gamma_k = \frac{1}{2} \text{STr} [\tilde{\partial}_t \ln (1 + \mathcal{P}_k^{-1} \mathcal{F}_k)] = -\frac{1}{2} \tilde{\partial}_t \sum_{n=1}^{\infty} \frac{(-1)^n}{n} \text{STr} [(\mathcal{P}_k^{-1} \mathcal{F}_k)^n]. \quad (1.17)$$

Here the derivative $\tilde{\partial}_t$ acts only on the k -dependence of the regulator \mathcal{R}_k , *i.e.*

$$\tilde{\partial}_t := \sum_{\chi \text{ in } \Phi} \int dy \frac{\partial_t [Z_k^{\chi}(y) r_k^{\chi}(y)]}{Z_k^{\chi}(y)} \frac{\delta}{\delta r_k^{\chi}(y)}, \quad (1.18)$$

with χ cycling through the various fields contained in Φ . Note that we omitted an unimportant, field-independent constant $\frac{1}{2} \tilde{\partial}_t \text{STr} \ln \mathcal{P}_k$ in Eq. (1.17). In an explicit calculation, the right-hand side of this equation can then be truncated at the maximum power of the field considered in the ansatz for Γ_k .

1.3 Fixed points, universality, and asymptotic safety

A particular model of a physical system is characterized by its degrees of freedom (the fields) and a set of symmetries that interactions between the fields have to obey. All action functionals consistent with the required symmetries form the *theory space* of the model, which defines the dynamical environment for the renormalization group flow. In practice, one usually parametrizes the theory space by *couplings* g_1, g_2, \dots that multiply the admissible interaction vertices.* The example (1.1), for instance, features two couplings, \bar{m}^2 and \bar{h} , parametrizing a mass term and a Yukawa interaction, respectively. Hence the vertices define coordinate axes in theory space, and the values of the associated couplings are the coordinates of a particular action in this space. Given a complete set of vertices, the Wetterich equation (1.13) then translates into a system of coupled differential equations for the couplings,

$$\partial_t g_A = \beta_A[g_1, g_2, \dots], \quad (A = 1, 2, \dots). \quad (1.19)$$

Notice that we do not denote the scale dependence of the couplings explicitly in order to keep the notation slim. Provided with some initial values for the couplings at $t = 0$ ($k = \Lambda$), *i.e.* a bare action, we can then in principle integrate these flow equations down to $t = -\infty$ ($k = 0$) and obtain the corresponding effective action.

Fixed points and critical exponents. The practical use of this view on renormalization, however, is not so much the computation of flows for a particular microscopic model, but rather the ability to classify regimes in theory space by their IR or UV behavior and to extract universal properties. In particular, the functional renormalization group allows us to probe regions of theory space that are inaccessible to perturbative quantum field theory due to large coupling values.

*We will employ a rather general understanding of the term *coupling* in the discussion of this section and include masses, wave function renormalizations, *etc.* in the definition. Basically any scalar multiplying a product of fields in the action will be referred to as a coupling.

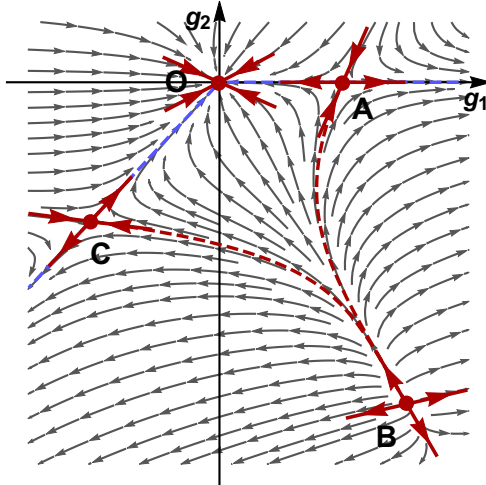


Figure 2: Example theory space with two couplings g_1 and g_2 and four fixed points. Red arrows indicate the eigendirections at each fixed point. The Gaussian fixed point at the origin has two irrelevant directions, the fixed points A and C have one relevant and one irrelevant, and the fixed point B has two relevant directions. For the fixed points A and C, separatrices of IR (red) and UV (blue) regimes are plotted as dashed lines.

The key to analyzing the topology of the renormalization group flow are its fixed points, corresponding to RG-invariant theories. This is equivalent to the condition $\beta_A[g_1, \dots] = 0$ for all A if we choose the couplings to be dimensionless and renormalized, which we can always do by rescaling with appropriate powers of the RG scale k and the wave function renormalizations Z_k . Consequently, if we start with a fixed point action at the microscopic scale, we will be left with the same action after all fluctuations have been integrated out, meaning that bare and effective actions coincide. The free theory with just kinetic terms is always scale-invariant and is known as the *Gaussian fixed point*.

As with any dynamical system, RG fixed points may either be attractive or repulsive along a particular direction in theory space. If we start within the domain of attraction of a certain fixed point, all couplings corresponding to attractive directions will approach the fixed point values as the renormalization scale is lowered. Such couplings are called *irrelevant* because their values in the effective action do not depend on the precise initial conditions, but are entirely determined by the closest fixed point in theory space. On the contrary, couplings associated with repulsive directions are called *relevant*, and their initial values will in general affect the resulting effective theory.

A theory space with two couplings and four fixed points is depicted in Fig. 2 along with some example flows. Fixed points with at least one relevant direction are of particular interest because they potentially describe critical points of second order phase transitions if the number of relevant operators matches the number of order parameters. The flow lines emanating from (or rather pouring into) the associated irrelevant eigendirections, indicated in the plot by red dashed lines for the fixed points A and C, are called *separatrices* and form the *IR-critical hypersurface* because they separate different regimes of IR physics and mark phase transitions. Consider, for example, the fixed point C: If we start above the separatrix, we will flow towards the Gaussian fixed point and obtain an asymptotically free effective theory, whereas starting below the separatrix takes us towards infinity and an interacting effective theory. To predict the IR behavior, we thus need to measure only one parameter because the controlling fixed point has only one relevant direction. Within the asymptotic safety scenario to be discussed below, a theory is (nonperturbatively) renormalizable and predictive if it involves only a finite number of relevant couplings, corresponding to a finite number of parameters that have to be determined by experiment.

In the vicinity of a fixed point $\mathbf{g}_* = (g_{1*}, g_{2*}, \dots)$, we can compute the relevant and irrelevant directions by linearizing the flow equations (1.19) for a small perturbation $\mathbf{g} = \mathbf{g}_* + \boldsymbol{\varepsilon}$ around the

fixed point, *i.e.*

$$\partial_t \varepsilon_A = \sum_B \frac{\partial \beta_A[\mathbf{g}]}{\partial g_B} \bigg|_{\mathbf{g}=\mathbf{g}_*} \varepsilon_B + \mathcal{O}(\varepsilon^2) . \quad (1.20)$$

The solutions of this differential equation can be written in the form $\varepsilon = \sum_i e^{-\theta_i t} c_i \mathbf{v}_i$, where θ_i are the eigenvalues of the (negative) stability matrix $(-\partial \beta_A / \partial g_B|_*)$, and \mathbf{v}_i are the corresponding right eigenvectors. The latter are indicated by red arrows in the example of Fig. 2. The eigenvalues are commonly called *critical exponents* because of their relation to thermodynamical critical exponents characterizing continuous phase transitions. We immediately infer that eigenvectors \mathbf{v}_i with $\text{Re } \theta_i > 0$ define relevant directions whereas those with $\text{Re } \theta_i < 0$ define irrelevant directions in theory space. Those with $\text{Re } \theta_i = 0$ are called *marginal* directions, and higher-order terms in Eq. (1.20) are needed to determine whether they are attractive or repulsive.

Universality. A major reason for the importance of the RG in statistical physics is the explanation it offers for the principle of *universality*. This idea is based on the observation that distinct physical systems can show similar macroscopic behavior regardless of their precise microscopic dynamics [1, 2, 70]. For instance, both the ferromagnetic–paramagnetic transition in magnets with a preferred axis and the liquid–gas transition in certain fluids fall into the so-called *Ising universality class*, ascribing them the same set of critical exponents for the corresponding thermodynamic quantities.

The reason for this phenomenon lies in the above stated insight that the macroscopic properties of a theory are essentially controlled by the closest fixed point in theory space and its relevant directions. As an example, consider Fig. 2 once again. Here a theory starting microscopically with a pure g_1 interaction left from the separatrix of the fixed point A is macroscopically indistinguishable from a theory starting with a pure g_2 interaction above the separatrix of C: In both cases, we end up with a free, noninteracting theory in the low-energy limit. By contrast, if we start on the other side of the separatrices, respectively, we end up in different IR regimes as noted above, such that the interacting fixed points with (at least) one relevant direction are linked to phase transitions.

In the models we are considering here, fixed points with exactly one relevant direction mark critical points of a continuous second-order phase transition. In this case, the inverse of the relevant eigenvalue θ_1 is just the corresponding thermodynamic correlation length exponent $\nu = 1/\theta_1$ [2, 69]: Approaching such a critical point, the system loses separation of scales and becomes increasingly scale invariant. Precisely at the critical point, the system does not have an intrinsic scale anymore and fluctuations at all scales matter equally, meaning that the correlation length ξ of the order parameter two-point function diverges as $\xi \sim |c_1|^{-\nu}$, where c_1 is the coefficient of the relevant perturbation, a generalized reduced temperature. Consequently, the two-point function decays only power-law-like with the spatial separation, and the corresponding exponent may receive corrections to the expected canonical scaling, parametrized by the anomalous dimension η [69, 70], which is obtained from the wave function renormalization Z via $\eta = -\partial_t \ln Z$. Under quite general assumptions, so-called scaling relations link ν and η to the other thermodynamic critical exponents associated with the behavior of order parameters, susceptibility, source field, *etc.* [2, 69, 70]. Hence the macroscopic properties of the phase transition are essentially determined by computing two of the critical exponents, *e.g.* ν and η .

Asymptotic safety. Functional renormalization group studies are not only useful to derive macroscopic from microscopic properties. Instead, we can also ask the opposite question about the underlying fundamental theory of a model and investigate the RG flow for increasing energies. This is especially interesting for models that are not perturbatively renormalizable because the number of required counterterms to cancel divergences as $k \rightarrow \Lambda \rightarrow \infty$ is infinite, as it is the case, *e.g.*, in quantum gravity. For such models, salvation may be found in the asymptotic safety scenario [5, 71] first proposed by Weinberg in 1976 [4].

The idea is a generalization of asymptotic freedom [85, 86], which describes theories such as QCD that become noninteracting at high energies, meaning that the UV limit is governed by the Gaussian fixed point. Asymptotic safety assumes that the microscopic model is controlled by an *interacting* fixed point instead. Let us take yet another look at Fig. 2, this time thinking of the flow lines as being reversed such that they describe the evolution towards higher energies. This way, IR-relevant directions become attractive to the RG flow towards the UV, whereas IR-irrelevant directions

become repulsive. Different UV scenarios are now separated by the IR-relevant directions, which form the *UV-critical hypersurface* of a fixed point, shown as blue dashed lines in the figure.

We observe that if the flow starts on a UV-critical hypersurface, we will eventually flow into the associated fixed point as $k \rightarrow \Lambda \rightarrow \infty$, meaning that the fixed point describes the microscopic theory in the continuum limit. More importantly, all couplings will then take the fixed point values and hence remain finite, so that the theory is free of divergences and *asymptotically safe*.

These thoughts reveal a generalized view on renormalization and renormalizability. Renormalization of a theory merely means a projection onto the UV-critical hypersurface, so that all couplings take finite values in the continuum limit. The projection constrains the IR-irrelevant vertices, but their values do not matter anyway as far as the effective, low-energy theory is concerned. To determine the position of a renormalized theory, we thus have to measure as many parameters as there are relevant directions to the controlling fixed point. Consequently, a theory is nonperturbatively renormalizable if the number of relevant couplings of the corresponding fixed point is finite. Incidentally, this projection also happens when perturbatively renormalizing an asymptotically free theory via the introduction of counterterms [5]. In general, however, perturbative and nonperturbative renormalizability as introduced here describe different concepts, where neither is a subset of the other [5, 69].

* * *

This completes our short introduction to the functional renormalization group framework and its applications. In what follows, we will explore the theory space of relativistic four-fermion interactions along the lines established in this section. In the next section, we will study general aspects of the RG flow of such models, before we will turn to concrete examples in the subsequent sections. There, finding and characterizing fixed points within these particular settings will be our main objective.

2

Momentum-dependent four-fermion vertices

We begin with a rather general discussion of abstract four-fermion interactions, which includes the specific models we are going to study in Sections 3 and 4. We will investigate properties of their renormalization group flow, analyze the structure of the underlying theory space and report the effect of symmetries constraining the choice of admissible vertices. In the remainder of this section, our aim will then be to derive the flow equations for the associated momentum-dependent coupling functions.

Let us consider N_f flavors of fermions described by the Grassmann-valued spinor fields $\psi^i, \bar{\psi}^i$, $i = 1, \dots, N_f$. To fix the spinor space, we have to choose a representation of gamma matrices $\gamma_1, \dots, \gamma_d \in \mathbb{C}^{d_\gamma \times d_\gamma}$ satisfying the anticommutation relations

$$\{\gamma_\mu, \gamma_\nu\} = 2\delta_{\mu\nu}, \quad (2.1)$$

which generate the associated Clifford algebra. The spinors are then vectors in the d_γ -dimensional Dirac space. In this setting, a rather general four-fermion vertex takes the form

$$\int d^d x \bar{g} \bar{\psi}^i(x) \mathcal{O}_1 \psi^i(x) \bar{\psi}^j(x) \mathcal{O}_2 \psi^j(x),$$

where \mathcal{O}_1 and \mathcal{O}_2 are $(d_\gamma \times d_\gamma)$ -dimensional matrices in Dirac space and summation over repeated flavor indices is understood. We do not consider flavor-mixing even though this is possible along the same lines in principle. The coupling \bar{g} parametrizes the strength of the interaction and will in general depend on the renormalization scale k . We notice that this vertex includes each of the fields ψ and $\bar{\psi}$ exactly twice, a consequence of the conservation of particle number, as can be seen from the fact that, roughly speaking, ψ annihilates and $\bar{\psi}$ creates a particle, or vice versa for antiparticles. Furthermore, the above vertex has a flavor-singlet structure, where one could in principle also define flavor nonsinglets such as $\bar{\psi}^i \mathcal{O}_1 \psi^j \bar{\psi}^j \mathcal{O}_2 \psi^i$. However, these can always be transformed into flavor singlets via so-called *Fierz transformations* as we will see below. By means of a Fourier transformation, we can equally express the above vertex in momentum space,

$$\int_{p_1, p_2, p_3, p_4} (2\pi)^d \delta(p_1 + p_2 + p_3 + p_4) \bar{g} \bar{\psi}^i(-p_1) \mathcal{O}_1 \psi^i(p_2) \bar{\psi}^j(-p_3) \mathcal{O}_2 \psi^j(p_4), \quad (2.2)$$

as depicted in Fig. 3. Our convention is that all momenta are measured as flowing into the vertex. Eventually, we will allow the coupling \bar{g} to depend on the momenta of the involved particles, rendering the interaction nonlocal.

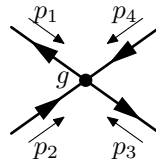


Figure 3: Feynman diagram for a generic four-fermion interaction with coupling g . In our convention, all momenta are measured as flowing into the vertex.

2.1 Symmetries and Fierz transformations

Symmetries. A *symmetry* of a theory is a transformation $\psi, \bar{\psi} \mapsto \psi', \bar{\psi}'$ of the fields that leaves the action of the theory invariant, *i.e.* $S[\psi', \bar{\psi}'] = S[\psi, \bar{\psi}]$. In particular, the interaction vertices have to be invariant under this transformation. As a first example, we introduce unitary rotations in flavor space, $\psi^i \mapsto U^{ij} \psi^j$ and $\bar{\psi}^i \mapsto \bar{\psi}^j (U^\dagger)^{ji}$ with $U \in U(N_f)$. These already form a symmetry of the general vertex (2.2) because the matrices \mathcal{O}_i as introduced above are trivial in flavor space. However, requiring additional symmetries that transform the Dirac space structure of the fields can restrict the admissible choices for the matrices \mathcal{O}_1 and \mathcal{O}_2 . Since the symmetry transformations

will involve similar matrices themselves, it is convenient to define a basis of the Dirac space and discuss the implications of symmetries for the basis elements.

In a d_γ -dimensional representation of the Dirac algebra, a basis of the space of Dirac matrices consists of d_γ^2 linearly independent matrices. Besides the d matrices $\{\gamma_\mu\} = \{\gamma_1, \dots, \gamma_d\}$ generating the Clifford algebra, there are thus always $d_\gamma^2 - d$ additional matrices to complete a basis set of $\mathbb{C}^{d_\gamma \times d_\gamma}$. Let us denote a particular example of such a basis by $\{\gamma_A\}$. The most general matrix \mathcal{O} entering a fermion bilinear in (2.2) can then be written as a linear combination of basis matrices, $\mathcal{O} \in \text{span}\{\gamma_A\}$.

In this thesis, we are especially interested in (2+1)-dimensional relativistic fermions in the reducible representation of the Clifford algebra. For the remainder of this paragraph, we will therefore assume $d = 3$ and $d_\gamma = 4$. An exhaustive discussion of the symmetries of such systems and compatible four-fermion vertices can be found in Refs. [17, 24, 32, 60, 94, 95]. The analysis there is restricted to pointlike, momentum-independent interactions, but the additional assumption of momentum-dependent couplings does not affect the general result. Therefore, we will only state the main implications relevant for our analysis and point to these references for details.

A reducible representation of the γ matrices in $d = 3$ can be derived from an irreducible representation in $d = 4$, but we only need, *e.g.*, γ_1 , γ_2 , and γ_3 to generate the Clifford algebra (2.1). Hence there are now two additional Dirac matrices, γ_4 and γ_5 , that anticommute with the three γ_μ and with each other. In addition to these five matrices, we will assume that our basis $\{\gamma_A\}$ contains the elements $\gamma_{\mu\nu} := \frac{i}{2} [\gamma_\mu, \gamma_\nu]$ ($\mu < \nu$), which generate Lorentz transformations, as well as the product $\gamma_{45} := i\gamma_4\gamma_5$, which generates a continuous transformation $\psi \mapsto e^{i\alpha\gamma_{45}}\psi$, $\bar{\psi} \mapsto \bar{\psi}e^{-i\alpha\gamma_{45}}$. The combination of flavor rotations and these continuous transformations leads to the group $U(N_f) \times U(N_f)$ because each of the generators of the $U(N_f)$ flavor transformations may be joined with either the identity $\mathbf{1}_\gamma$ or the generator γ_{45} .

There is also one independent *discrete* chiral transformation that may be modeled by multiplying ψ by either γ_4 or γ_5 and $\bar{\psi}$ by its Hermitian conjugate. Multiplication with the other of these two matrices can then be composed from the continuous γ_{45} transformations above and multiplications with the first one. Further discrete symmetries, in particular parity, time reversal, and charge conjugation, are implemented in a similar fashion [31].

The defining vertex of the *Gross-Neveu model* [14], which will be our subject of study in Section 3, is a scalar flavor singlet $(\bar{\psi}^i\psi^i)^2$. All of the transformations mentioned so far leave this vertex invariant, so that they are symmetries of the model. One can show that there is no (non-derivative) two-fermion term consistent with all these symmetries; in particular, a mass term is ruled out by the discrete chiral symmetry [95]. On the level of four-fermion vertices, however, there are, up to Fierz transformations, three additional terms that share all the symmetries of the Gross-Neveu vertex. A complete set of four-fermion interaction terms for the Gross-Neveu model consists, for instance, of [95]

$$(\bar{\psi}^i\psi^i)^2, \quad (\bar{\psi}^i\gamma_{45}\psi^i)^2, \quad (\bar{\psi}^i\gamma_\mu\psi^i)^2, \quad (\bar{\psi}^i\gamma_{\mu\nu}\psi^i)^2. \quad (2.3)$$

The vector-type interaction $(\bar{\psi}^i\gamma_\mu\psi^i)^2$ is also the defining vertex of the *Thirring model* [36] to be studied in Section 4. Contrary to the Gross-Neveu vertex, it is additionally invariant under *continuous* chiral transformations generated by γ_4 and γ_5 , $\psi \mapsto e^{i\alpha\gamma_{4,5}}\psi$, $\bar{\psi} \mapsto \bar{\psi}e^{i\alpha\gamma_{4,5}}$. This leads to the larger symmetry group $U(2N_f)$ of combined flavor and chiral transformations [31]. Of the vertices (2.3), the pseudoscalar term also satisfies this symmetry, hence the vertices compatible with the Thirring model are [32]

$$(\bar{\psi}^i\gamma_{45}\psi^i)^2 \quad \text{and} \quad (\bar{\psi}^i\gamma_\mu\psi^i)^2. \quad (2.4)$$

Fierz transformations. In the introduction to this section, we claimed that it was sufficient to study four-fermion vertices with a flavor-singlet structure. The reason for this is that we can use Fierz transformations to rewrite nonsinglet vertices in terms of singlet terms. Without loss of generality, we can choose our Dirac space basis matrices γ_A to be orthogonal with respect to the inner product $\gamma_A \cdot \gamma_B := \text{tr}(\gamma_A\gamma_B)$, *i.e.*

$$\text{tr}(\gamma_A\gamma_B) = d_\gamma \delta_{AB}. \quad (2.5)$$

Using this orthogonality relation and the fact that the γ_A form a basis, we can expand any matrix $\mathcal{O} \in \mathbb{C}^{d_\gamma \times d_\gamma}$ as

$$\mathcal{O} = \frac{1}{d_\gamma} \sum_{A=1}^{d_\gamma^2} \text{tr}(\mathcal{O} \gamma_A) \gamma_A. \quad (2.6)$$

The most general two-spinor vertex thus takes the form $\sum_A m_A \bar{\psi}^i \gamma_A \psi^i$. For four-fermion vertices, we can in principle combine any of the two-spinor terms. Moreover, we can implement them in a flavor-singlet or flavor-nonsinglet form, namely

$$\text{singlet: } \bar{\psi}^i \gamma_A \psi^i \bar{\psi}^j \gamma_B \psi^j, \quad \text{nonsinglet: } \bar{\psi}^i \gamma_A \psi^j \bar{\psi}^j \gamma_B \psi^i. \quad (2.7)$$

These two forms are, however, related via Fierz transformations: Using the completeness property (2.6), we can expand the Dirac matrix $\psi^j \bar{\psi}^j$ appearing in the nonsinglet term and obtain a flavor-singlet structure:

$$\bar{\psi}^i \gamma_A \psi^j \bar{\psi}^j \gamma_B \psi^i = \frac{1}{d_\gamma} \sum_C \bar{\psi}^i \gamma_A \text{tr}(\psi^j \bar{\psi}^j \gamma_C) \gamma_C \gamma_B \psi^i = -\frac{1}{d_\gamma} \sum_C \bar{\psi}^i \gamma_A \gamma_C \gamma_B \psi^i \bar{\psi}^j \gamma_C \psi^j. \quad (2.8)$$

Hence it suffices to consider, for example, only the singlet terms. Together with the symmetry considerations from the previous paragraph, this constrains the types of vertices generated by the RG flow for a specific model.

Momentum dependence. As the aim of this work is a study of four-fermion interactions in a vertex expansion, we need to consider the momentum dependence of the couplings parametrizing the vertices of our models. To this end, we promote the couplings like \bar{g} in Eq. (2.2) to functions of the external momenta, $\bar{g} = \bar{g}(p_1, p_2, p_3, p_4)$. Consequently, the interaction becomes nonlocal. Due to momentum conservation, only three of those vectors are independent. Moreover, the requirement of Lorentz invariance restricts the possible dependences further. In general, N vectors allow for $\frac{N(N+1)}{2}$ linearly independent invariants, *e.g.*, the N squared norms and $\frac{N(N-1)}{2}$ dot products of two different vectors. Consequently, the coupling functions here can effectively only depend on up to six real, linearly independent Lorentz invariants that can be constructed from three independent momentum vectors.

Additional symmetries of the coupling function may be implied by the symmetries of the associated vertex. For instance, a vertex with $\mathcal{O}_1 = \mathcal{O}_2$ requires the coupling to satisfy $\bar{g}(p_1, p_2, p_3, p_4) = \bar{g}(p_3, p_4, p_1, p_2)$. This will hold for all models considered in this thesis and will also be assumed in our study of rather general properties of the flow of momentum-dependent couplings coming up next.

2.2 Flow equations for the coupling functions

In this section we develop a scheme to compute flow equations for an arbitrary number of momentum-dependent four-fermion interactions. To this end, let

$$\Gamma_k[\psi, \bar{\psi}] = - \int_p Z(p^2) \bar{\psi}(p) \psi(p) + \sum_A \int_{p_2, p_3, p_4} \frac{\bar{g}_A(p_1, p_2, p_3, p_4)}{2\tilde{N}} \bar{\psi}(-p_1) \mathcal{O}_A \psi(p_2) \bar{\psi}(-p_3) \mathcal{O}_A \psi(p_4) \quad (2.9)$$

be a generic model effective action featuring multiple interaction vertices with coupling functions g_A and Dirac space matrices \mathcal{O}_A . Here and in the following, $p_1 \equiv -p_2 - p_3 - p_4$, and $\tilde{N} := N_f d_\gamma$. As explained above, momentum conservation and Lorentz invariance imply that this function can effectively depend only on six real, Lorentz invariant parameters. However, we will stick to the redundant notation of Eq. (2.9) because it allows us to keep track of the flow of loop momenta in the Wetterich equation (1.13) and sorts well with the pictorial language of Feynman diagrams.

We also included a momentum-dependent wave function renormalization $Z(p^2)$, whose scale dependence is likewise suppressed. By analogy with the pointlike limit, we define a generalized anomalous dimension function

$$\eta(p^2) := -\partial_t \ln Z(p^2). \quad (2.10)$$

The general form (2.9) of the effective average action includes a large class of physically interesting cases [95]. In particular, the Gross-Neveu and Thirring models to be investigated in detail in Sections 3 and 4 are recovered for $\mathcal{O}_0 = \mathbf{1}$, $g_0 = g_{\text{GN}}$ and $\mathcal{O}_\mu = \gamma_\mu$, $g_\mu = g_{\text{Th}}$ ($\mu = 1, 2, 3$). Note that we restrict the analysis to flavor singlet structures because any flavor nonsinglet can be re-expressed in terms of flavor singlets via Fierz transformations as shown in the previous section.

Dimensionless couplings and momenta. A key step in the classification of the considered theory space are fixed point actions corresponding to theories that are invariant under the renormalization group (*cf.* Section 1.3). In order to find such scale-invariant theories, we need to parametrize our theory space in terms of dimensionless quantities. In particular, we need to switch to dimensionless momenta and coupling functions by measuring all quantities with respect to the renormalization scale k . This transformation will produce additional scaling terms that supplement the fluctuation-induced contributions.

To keep track of the various origins of scale dependences, let us be very explicit regarding the arguments of the coupling functions in this paragraph. A general coupling function of a four-fermion vertex depends on the renormalization scale and the four momenta, $\bar{g} = \bar{g}(k; p_1, p_2, p_3, p_4)$. Its canonical (mass) dimension is $[\bar{g}] = 2 - d$, as can be read off from the effective action (2.9) because $[\Gamma_k] = 0$. We renormalize the fields, $\psi_R(p) := Z_k^{1/2}(p^2)\psi(p)$ and $\bar{\psi}_R(p) := Z_k^{1/2}(p^2)\bar{\psi}(p)$, and rescale the couplings according to

$$g(k; p_i) := k^{d-2} \left[Z^{(4)}(p_1^2, p_2^2, p_3^2, p_4^2) \right]^{-2} \bar{g}(k; p_i) \quad \text{with} \quad Z^{(n)}(p_i^2) = \left[\prod_{j=1}^n Z(p_j^2) \right]^{1/n}. \quad (2.11)$$

This renders g dimensionless and absorbs the wave function renormalization into the coupling. Moreover, we need to introduce dimensionless momenta $\tilde{p} = p/k$, *etc.*, such that $\tilde{g}(k; \tilde{p}_i) := g(k; \tilde{p}_i k)$ is the coupling function of interest. Taking the logarithmic derivative with respect to the scale at fixed \tilde{p}_i , we then obtain

$$\begin{aligned} \partial_t \tilde{g}(k; \tilde{p}_i) &= \partial_t \left\{ k^{d-2} \left[Z^{(4)}(p_i^2) \right]^{-2} \bar{g}(k; \tilde{p}_i k) \right\} \\ &= \left[d - 2 + 2 \tilde{\eta}^{(4)}(\tilde{p}_i^2) \right] \tilde{g}(k; \tilde{p}_i) + \sum_{j=1}^4 \tilde{p}_j \cdot \nabla_{\tilde{p}_j} \tilde{g}(k; \tilde{p}_i) + k^{d-2} \left[Z^{(4)}(p_i^2) \right]^{-2} \partial_t \bar{g}(k; p_i) \Big|_{p_i = \tilde{p}_i k} \end{aligned} \quad (2.12)$$

with the definition

$$\tilde{\eta}^{(4)}(\tilde{p}_1^2, \tilde{p}_2^2, \tilde{p}_3^2, \tilde{p}_4^2) := \frac{1}{4} \sum_{j=1}^4 \eta(\tilde{p}_j^2 k^2). \quad (2.13)$$

In the following, we will drop all tildes denoting dimensionless quantities again and only distinguish dimensionful coupling functions by an overbar from their dimensionless counterparts. The momentum arguments entering either of the two are silently assumed to be either dimensionful or dimensionless, respectively. Furthermore, we will suppress the dependence on the renormalization scale k again. To summarize, the general flow equation of any dimensionless four-fermion coupling function thus takes the form

$$\partial_t g(p_i) = \left[d - 2 + 2\eta^{(4)}(p_i^2) \right] g(p_i) + \sum_{j=1}^4 p_j \cdot \nabla_{p_j} g(p_i) + (\text{quantum fluctuations}), \quad (2.14)$$

where the quantum fluctuations correspond to the last term in Eq. (2.27) and are obtained from the flow of the dimensionful quantities according to the Wetterich equation (1.13).

P-F decomposition. To derive these quantum contributions, we proceed according to the algorithm suggested in Section 1.2 by decomposing the regularized inverse propagator $\Gamma_k^{(2)} + \mathcal{R}_k$ into field-independent and -dependent components \mathcal{P}_k and \mathcal{F}_k , respectively. For the field-independent part, we find

$$\mathcal{P}_k(q, q') = -\frac{F(q^2)}{q^2} \begin{pmatrix} 0 & \not{q}^\text{T} \\ \not{q} & 0 \end{pmatrix} (2\pi)^d \delta(q - q'), \quad F(q^2) = Z(q^2)q^2 [1 + r_k(q^2)], \quad (2.15)$$

where r_k is the fermionic regulator shape function. The field-dependent part is given by

$$\mathcal{F}_k(q, q') = \begin{pmatrix} \mathcal{F}_{\psi\psi} & \mathcal{F}_{\psi\bar{\psi}} \\ \mathcal{F}_{\bar{\psi}\psi} & \mathcal{F}_{\bar{\psi}\bar{\psi}} \end{pmatrix} \quad (2.16)$$

with components

$$\mathcal{F}_{\psi\psi}(q, q') = -\frac{1}{\tilde{N}} \sum_A \int_p \bar{g}_A(q-q'-p, -q, p, q') \mathcal{O}_A^\top \bar{\psi}^\top(-q+q'+p) \bar{\psi}(-p) \mathcal{O}_A \quad (2.17a)$$

$$\begin{aligned} \mathcal{F}_{\psi\bar{\psi}}(q, q') = & \frac{1}{\tilde{N}} \sum_A \int_p \left[-\bar{g}_A(q-q'-p, p, q', -q) \bar{\psi}^\top(-q+q'+p) \mathcal{O}_A \psi(p) \mathcal{O}_A^\top \right. \\ & \left. + \bar{g}_A(q-q'-p, -q, q', p) \mathcal{O}_A^\top \bar{\psi}^\top(-q+q'+p) \psi^\top(p) \mathcal{O}_A^\top \right] \end{aligned} \quad (2.17b)$$

$$\begin{aligned} \mathcal{F}_{\bar{\psi}\psi}(q, q') = & \frac{1}{\tilde{N}} \sum_A \int_p \left[\bar{g}_A(q-q'-p, p, -q, q') \bar{\psi}^\top(-q+q'+p) \mathcal{O}_A \psi(p) \mathcal{O}_A \right. \\ & \left. + \bar{g}_A(q-q'-p, q', -q, p) \mathcal{O}_A \psi(p) \bar{\psi}(-q+q'+p) \mathcal{O}_A \right] \end{aligned} \quad (2.17c)$$

$$\mathcal{F}_{\bar{\psi}\bar{\psi}}(q, q') = -\frac{1}{\tilde{N}} \sum_A \int_p \bar{g}_A(-q, q-q'-p, q', p) \mathcal{O}_A \psi(q-q'-p) \psi^\top(p) \mathcal{O}_A^\top. \quad (2.17d)$$

Note that we have indicated already contracted pairs of spinors to guide the eye. Such contractions behave like a c-number, *i.e.* they commute with any other objects in the above formulae. The building block of the field expansion (1.17) is the product $\mathcal{P}_k^{-1} \mathcal{F}_k$, whose components in our case are

$$\begin{aligned} (\mathcal{P}_k^{-1} \mathcal{F}_k)_{\psi\psi}(q, q') = & \frac{1}{\tilde{N} F(q^2)} \sum_A \int_p \left[-\bar{g}_A(q-q'-p, p, -q, q') \bar{\psi}^\top(-q+q'+p) \mathcal{O}_A \psi(p) \not{q} \mathcal{O}_A \right. \\ & \left. - \bar{g}_A(q-q'-p, q', -q, p) \not{q} \mathcal{O}_A \psi(p) \bar{\psi}(-q+q'+p) \mathcal{O}_A \right] \end{aligned} \quad (2.18a)$$

$$(\mathcal{P}_k^{-1} \mathcal{F}_k)_{\psi\bar{\psi}}(q, q') = \frac{1}{\tilde{N} F(q^2)} \sum_A \int_p \bar{g}_A(-q, q-q'-p, q', p) \not{q} \mathcal{O}_A \psi(q-q'-p) \psi^\top(p) \mathcal{O}_A^\top \quad (2.18b)$$

$$(\mathcal{P}_k^{-1} \mathcal{F}_k)_{\bar{\psi}\psi}(q, q') = \frac{1}{\tilde{N} F(q^2)} \sum_A \int_p \bar{g}_A(q-q'-p, -q, p, q') \not{q}^\top \mathcal{O}_A^\top \bar{\psi}^\top(-q+q'+p) \bar{\psi}(-p) \mathcal{O}_A \quad (2.18c)$$

$$\begin{aligned} (\mathcal{P}_k^{-1} \mathcal{F}_k)_{\bar{\psi}\bar{\psi}}(q, q') = & \frac{1}{\tilde{N} F(q^2)} \sum_A \int_p \left[\bar{g}_A(q-q'-p, p, q', -q) \bar{\psi}^\top(-q+q'+p) \mathcal{O}_A \psi(p) \not{q}^\top \mathcal{O}_A^\top \right. \\ & \left. - \bar{g}_A(q-q'-p, -q, q', p) \not{q}^\top \mathcal{O}_A^\top \bar{\psi}^\top(-q+q'+p) \psi^\top(p) \mathcal{O}_A^\top \right]. \end{aligned} \quad (2.18d)$$

To extract the flow equations of the couplings \bar{g}_A , we have to evaluate the diagonal elements of the square of this expression and add them (with the additional fermionic minus sign) to obtain the supertrace of $(\mathcal{P}_k^{-1} \mathcal{F}_k)^2$. After some algebra as well as relabeling and shifting of momenta, we

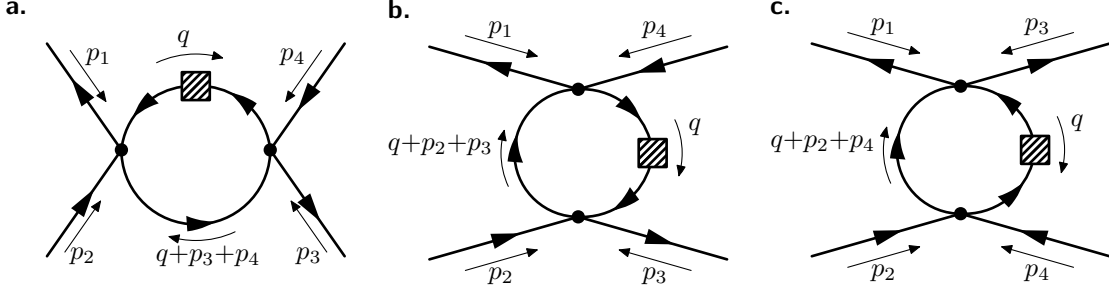


Figure 4: Feynman diagrams for the three channels of regularized one-loop processes contributing to the RG flow of a generic four-fermion interaction vertex. The shaded boxes denote the regulator insertions. By convention, the three channels are parametrized in terms of the Mandelstam variables, which encode the momenta transferred across the loops. Diagram (a) corresponds to the s -channel, diagram (b) to the t -channel, and diagram (c) to the u -channel.

find

$$\begin{aligned}
& \text{STr} [(\mathcal{P}_k^{-1} \mathcal{F}_k)^2] \\
&= -\frac{2}{\tilde{N}^2} \int_{q,p_2,p_3,p_4} [F(q^2)]^{-1} \sum_{A,B} \left[[F(q'^2)]^{-1} \bar{g}_A(p_1, p_2, q', -q) \bar{g}_B(q, -q', p_3, p_4) \right. \\
&\quad \times \text{N_f} \text{tr}(\not{q}' \mathcal{O}_A \not{q} \mathcal{O}_B) \bar{\psi}(-p_1) \mathcal{O}_A \psi(p_2) \bar{\psi}(-p_3) \mathcal{O}_B \psi(p_4) \Big|_{q' = q+p_3+p_4} \\
&\quad - [F(q'^2)]^{-1} \bar{g}_A(p_1, p_2, q', -q) \bar{g}_B(p_3, -q', q, p_4) \\
&\quad \times \bar{\psi}(-p_1) \mathcal{O}_A \psi(p_2) \bar{\psi}(-p_3) \mathcal{O}_B \not{q}' \mathcal{O}_A \not{q} \mathcal{O}_B \psi(p_4) \Big|_{q' = q+p_3+p_4} \\
&\quad - [F(q'^2)]^{-1} \bar{g}_B(p_1, p_2, q', -q) \bar{g}_A(p_3, -q', q, p_4) \\
&\quad \times \bar{\psi}(-p_1) \mathcal{O}_B \psi(p_2) \bar{\psi}(-p_3) \mathcal{O}_A \not{q}' \mathcal{O}_B \not{q} \mathcal{O}_A \psi(p_4) \Big|_{q' = q+p_3+p_4} \\
&\quad - [F(q'^2)]^{-1} \bar{g}_A(p_1, q', -q, p_4) \bar{g}_B(-q', p_2, p_3, q) \\
&\quad \times \bar{\psi}(-p_1) \mathcal{O}_A \not{q}' \mathcal{O}_B \psi(p_2) \bar{\psi}(-p_3) \mathcal{O}_B \not{q} \mathcal{O}_A \psi(p_4) \Big|_{q' = q+p_2+p_3} \\
&\quad + [F(q'^2)]^{-1} \bar{g}_A(p_1, q', p_3, -q) \bar{g}_B(-q', p_2, q, p_4) \\
&\quad \times \bar{\psi}(-p_1) \mathcal{O}_B \not{q}' \mathcal{O}_A \psi(p_2) \bar{\psi}(-p_3) \mathcal{O}_B \not{q} \mathcal{O}_A \psi(p_4) \Big|_{q' = q+p_2+p_4} \Big]. \tag{2.19}
\end{aligned}$$

This result discloses the general one-loop structure of the Wetterich equation for the considered diagrams. There are four interacting fermions with momenta p_1 through p_4 . The one-loop process features two interactions, each of which pairs up two external and two loop fermions as can be seen from the arguments entering the coupling functions. Between these two interactions, the loop fermions are propagated by the $\not{q}/F(p^2)$ factors for $p = q, q'$, which are just the regularized fermion propagators.

Interaction channels and diagram functionals. Eq. (2.19) reveals that there are in principle four types of diagrams or *channels* contributing to the flow of the four-fermion vertices. They are characterized by the momentum transferred across the loop and can be parametrized conveniently in terms of the *Mandelstam variables* [96]

$$s := (p_1 + p_2)^2 = (p_3 + p_4)^2, \quad t := (p_1 + p_4)^2 = (p_2 + p_3)^2, \quad u := (p_1 + p_3)^2 = (p_2 + p_4)^2. \tag{2.20}$$

These interaction channels are depicted in Fig. 4. Note that our definition (2.20) of the Mandelstam variables differs from the standard (see, *e.g.*, Ref. [1]) due to the fact that we defined all momenta as incoming whereas the classical definition assumes two incoming and two outgoing particles. Equality is achieved by letting $p_3 \rightarrow -p_3, p_4 \rightarrow -p_4$.

By convention, we associate the s -channel with those interactions that involve at least one fully contracted pair of spinors $\bar{\psi}\psi$ entering the vertex, *i.e.* either (or both) of $\bar{\psi}(p_1)\psi(p_2)$ and $\bar{\psi}(p_3)\psi(p_4)$.

In fact the \mathfrak{s} -channel process in Fig. 4a can happen in two ways, depending on whether or not the incoming particles form composite states (*i.e.* a contracted pair of Dirac spinors). In the first variant, corresponding to the first term of the integral in Eq. (2.19), there are two incoming composite states, whereas in the second variant, given by the second and third terms in Eq. (2.19), there are one composite state and two individual fermions interacting. The fourth term in Eq. (2.19) corresponds to a \mathfrak{t} -channel interaction as shown in Fig. 4b, and the last term describes a \mathfrak{u} -channel process, depicted in Fig. 4c.

In order to formalize these observations, we introduce *diagram functionals* that parametrize the processes mathematically. These will be defined in terms of the dimensionless quantities introduced above, hence we switch to dimensionless momenta and couplings as well as renormalized fields. Taking the $\tilde{\partial}_t$ derivative of the supertrace in Eq. (2.19) then leads to

$$\begin{aligned} & \tilde{\partial}_t \text{STr} [(\mathcal{P}_k^{-1} \mathcal{F}_k)^2] \left(-\frac{1}{4} \right) k^{2(d+1)} \\ &= \frac{1}{2\tilde{N}} \int_{q,p_2,3,4} \sum_{A,B} \left[-b^{\mathfrak{s}2}[g_A, g_B](p_i, q) N_f \text{tr}(\not{q}' \mathcal{O}_A \not{q} \mathcal{O}_B) \bar{\psi}(-p_1) \mathcal{O}_A \psi(p_2) \bar{\psi}(-p_3) \mathcal{O}_B \psi(p_4) \Big|_{q' = q+p_3+p_4} \right. \\ & \quad + b^{\mathfrak{s}1}[g_A, g_B](p_i, q) \bar{\psi}(-p_1) \mathcal{O}_A \psi(p_2) \bar{\psi}(-p_3) \mathcal{O}_B \not{q}' \mathcal{O}_A \not{q} \mathcal{O}_B \psi(p_4) \Big|_{q' = q+p_3+p_4} \\ & \quad + b^{\mathfrak{s}1}[g_B, g_A](p_i, q) \bar{\psi}(-p_1) \mathcal{O}_B \psi(p_2) \bar{\psi}(-p_3) \mathcal{O}_A \not{q}' \mathcal{O}_B \not{q} \mathcal{O}_A \psi(p_4) \Big|_{q' = q+p_3+p_4} \\ & \quad + b^{\mathfrak{t}}[g_A, g_B](p_i, q) \bar{\psi}(-p_1) \mathcal{O}_A \not{q}' \mathcal{O}_B \psi(p_2) \bar{\psi}(-p_3) \mathcal{O}_B \not{q} \mathcal{O}_A \psi(p_4) \Big|_{q' = q+p_2+p_3} \\ & \quad \left. - b^{\mathfrak{u}}[g_A, g_B](p_i, q) \bar{\psi}(-p_1) \mathcal{O}_B \not{q}' \mathcal{O}_A \psi(p_2) \bar{\psi}(-p_3) \mathcal{O}_B \not{q} \mathcal{O}_A \psi(p_4) \Big|_{q' = q+p_2+p_4} \right]. \end{aligned} \quad (2.21)$$

The *diagram functional integrands* $b^{\mathfrak{m}}$ are a precursor of the desired diagram functionals. To specify their definition, we need to introduce the *threshold kernel*, which encodes the propagation of loop fermions and is given by

$$\begin{aligned} & \stackrel{a_1}{a_2} K_1^{(F)}(p, q; \eta) \\ &:= \left[\frac{(a_1 + a_2)q^2 + a_1(q \cdot p) - a_2 \frac{(q \cdot p)^2}{p^2}}{q^2(q + p)^2} \right] \frac{\partial_t r_1(q^2) - \eta(q^2)r_1(q^2)}{[1 + r_1(q^2)]^2 [1 + r_1([q + p]^2)]} \sim \text{Diagram} \quad (2.22) \end{aligned}$$

where p is the momentum transfer and q the loop momentum. The precise meaning of the parameters a_1 and a_2 will become clear later when we derive the flow equations of specific models. Roughly speaking, they correspond to different momentum modes in the propagation of loop fermions. The threshold kernel is a momentum-dependent generalization of the *threshold function* $\ell_1^{(F)}$ familiar from the pointlike limit (see, *e.g.*, Ref. [32]). The connection is established by the relation

$$\int_q \stackrel{a_1}{a_2} K_1^{(F)}(0, q; \eta) = 2v_d \left(a_1 + \frac{d-1}{d} a_2 \right) \ell_1^{(F)}(0; \eta), \quad (2.23)$$

which is verified straightforwardly using relation (B.9) for integrals of spherically symmetric functions. The diagram functional integrands occurring in Eq. (2.21) are then defined by

$$\begin{aligned} b^{\mathfrak{s}2}[g_1, g_2; \eta](p_i, q) &:= \frac{1}{\tilde{N}} {}_0^0 K_1^{(F)}(p_3 + p_4, q; \eta) [g_1(p_1, p_2, q', -q) g_2(q, -q', p_3, p_4) \\ & \quad + (q \longleftrightarrow -q')]_{q' = q+p_3+p_4}, \end{aligned} \quad (2.24a)$$

$$\begin{aligned} b^{\mathfrak{s}1}[g_1, g_2; \eta](p_i, q) &:= \frac{1}{\tilde{N}} {}_0^0 K_1^{(F)}(p_3 + p_4, q; \eta) [g_1(p_1, p_2, q', -q) g_2(p_3, -q', q, p_4) \\ & \quad + (q \longleftrightarrow -q')]_{q' = q+p_3+p_4}, \end{aligned} \quad (2.24b)$$

$$\begin{aligned} b^{\mathfrak{t}}[g_1, g_2; \eta](p_i, q) &:= \frac{1}{\tilde{N}} {}_0^0 K_1^{(F)}(p_2 + p_3, q; \eta) [g_1(p_1, q', -q, p_4) g_2(-q', p_2, p_3, q) \\ & \quad + (q \longleftrightarrow -q')]_{q' = q+p_2+p_3}, \end{aligned} \quad (2.24c)$$

$$b^u[g_1, g_2; \eta](p_i, q) := \frac{1}{N} {}_0^0 K_1^{(F)}(p_2 + p_4, q; \eta) [g_1(p_1, q', p_3, -q) g_2(-q', p_2, q, p_4) + (q \longleftrightarrow -q')]_{q' = q + p_2 + p_4}. \quad (2.24d)$$

The notation “ $+(q \longleftrightarrow -q')$ ” here means that all previous terms on the same bracket level have to be added with q and $-q'$ interchanged. The link to the diagrams of Fig. 4 is evident if we associate g_1 with the left or top vertex and g_2 with the right or bottom vertex. The definitions (2.24) merely follow the flow of momenta through the vertices g_1 and g_2 , propagating the loop momenta via the threshold kernel.

The remaining step in the derivation of flow equations is now to project the four-fermion vertices in Eq. (2.21) onto the ones present in the ansatz (2.9) for the effective average action that describes the desired model. Seeing as this requires knowledge of the precise form of the Dirac matrices \mathcal{O}_A and is thus model-specific, we cannot advance much further within the general setting proposed for this section. Nevertheless, at least for the models studied in this thesis, the individual processes contributing can all be expressed in terms of the diagram functionals

$${}_{a_2}^{a_1} B^m[g_1, g_2; \eta](p_i) := \int_q \left[(a_1 + a_2)q^2 + a_1(q \cdot p^m) - a_2 \frac{(q \cdot p^m)^2}{(p^m)^2} \right] b^m[g_1, g_2; \eta](p_i, q), \quad (2.25)$$

where m stands for any of the interaction channels $\mathfrak{s}2$, $\mathfrak{s}1$, t , u , and p^m is the momentum transfer vector of the m -channel, *i.e.* $p^s = p_3 + p_4$, $p^t = p_2 + p_3$, $p^u = p_2 + p_4$. Note that the additional factor in front of the b^m integrands is just the mode-selecting term of the threshold kernel (2.22), and the values of a_1 and a_2 are determined from the products and traces of Dirac matrices in Eq. (2.21). We can therefore rewrite the diagram functionals without reference to the b^m as

$${}_{a_2}^{a_1} B^{\mathfrak{s}2}[g_1, g_2; \eta](p_i) = \frac{1}{\tilde{N}} \int_q {}_{a_2}^{a_1} K_1^{(F)}(p_3 + p_4, q; \eta) [g_1(p_1, p_2, q', -q) g_2(q, -q', p_3, p_4) + (q \longleftrightarrow -q')]_{q' = q + p_3 + p_4}, \quad (2.26a)$$

$${}_{a_2}^{a_1} B^{\mathfrak{s}1}[g_1, g_2; \eta](p_i) = \frac{1}{\tilde{N}} \int_q {}_{a_2}^{a_1} K_1^{(F)}(p_3 + p_4, q; \eta) [g_1(p_1, p_2, q', -q) g_2(p_3, -q', q, p_4) + (q \longleftrightarrow -q')]_{q' = q + p_3 + p_4}, \quad (2.26b)$$

$${}_{a_2}^{a_1} B^t[g_1, g_2; \eta](p_i) = \frac{1}{\tilde{N}} \int_q {}_{a_2}^{a_1} K_1^{(F)}(p_2 + p_3, q; \eta) [g_1(p_1, q', -q, p_4) g_2(-q', p_2, p_3, q) + (q \longleftrightarrow -q')]_{q' = q + p_2 + p_3}, \quad (2.26c)$$

$${}_{a_2}^{a_1} B^u[g_1, g_2; \eta](p_i) = \frac{1}{\tilde{N}} \int_q {}_{a_2}^{a_1} K_1^{(F)}(p_2 + p_4, q; \eta) [g_1(p_1, q', p_3, -q) g_2(-q', p_2, q, p_4) + (q \longleftrightarrow -q')]_{q' = q + p_2 + p_4}. \quad (2.26d)$$

Having established these definitions, the quantum fluctuations contributing to the flow equation (2.14) can be written as a linear combination of diagram functionals, so that the overall general form of the four-fermion coupling flow equation is

$$\partial_t g_C(p_i) = \left[d - 2 + 2\eta^{(4)}(p_i^2) \right] g_C(p_i) + \sum_{j=1}^4 p_j \cdot \nabla_{p_j} g_C(p_i) + \sum_{A,B} \sum_m {}_{a_{m,2}}^{a_{m,1}} {}_{a_{m,2}}^{CAB} B^m[g_A, g_B; \eta](p_i). \quad (2.27)$$

For the theories considered in Sections 3 and 4, the factors $a_{m,1/2}^{CAB}$ are worked out in detail in Appendix B.3.

Pointlike limit. An important special case known as the *pointlike limit* is the one of constant coupling, for which diverse models of this type have already been studied in an FRG context. Setting $p_i \equiv 0$ and using the relation (2.23), we conclude that all diagram functionals reduce to the same limit,

$${}_{a_2}^{a_1} B^m[g_1, g_2; \eta](0) = \frac{4v_d}{\tilde{N}} \left(a_1 + \frac{d-1}{d} a_2 \right) \ell_1^{(F)}(0; \eta) g_1 g_2. \quad (2.28)$$

Hence the flow equation (2.27) becomes

$$\partial_t g_C = (d-2) g_C + \frac{4v_d}{\tilde{N}} \ell_1^{(F)}(0;0) \sum_{A,B} \sum_{\mathfrak{m}} \left(a_{\mathfrak{m},1}^{CAB} + \frac{d-1}{d} a_{\mathfrak{m},2}^{CAB} \right) g_A g_B, \quad (2.29)$$

where we used that the anomalous dimension vanishes for pointlike, purely fermionic interactions at this level of the truncation, as will become clear in the next section.

2.3 Anomalous dimension function

The anomalous dimension function expresses deviations from the canonical scaling of the propagator. By its definition (2.10), it describes the flow of the wave function renormalization, and we can use the Wetterich equation to relate it to the coupling functions.

Projection of the flow equation at second order in the fields. From the left-hand side of Eq. (1.17), we find

$$\partial_t \Gamma_k[\psi, \bar{\psi}] = - \int_p [\partial_t Z(p^2)] \bar{\psi}(p) \not{p} \psi(p) + \mathcal{O}([\bar{\psi} \psi]^2) = \int_p \eta(p^2) Z(p^2) \bar{\psi}(p) \not{p} \psi(p) + \mathcal{O}([\bar{\psi} \psi]^2) \quad (2.30)$$

While the renormalization of four-fermion vertices required the evaluation of the supertrace on the right-hand side of Eq. (1.17) at fourth order in the fields, the anomalous dimension is governed by diagrams of second order in the fields. We thus take the supertrace of Eq. (2.18) and obtain

$$\begin{aligned} \text{STr} [\mathcal{P}_k^{-1} \mathcal{F}_k] &= \frac{2}{\tilde{N}} \int_{p,q} \frac{1}{F(q^2)} \sum_A [\bar{g}_A(-p, p, -q, q) N_f \text{tr}(\not{q} \mathcal{O}_A) \bar{\psi}(p) \mathcal{O}_A \psi(p) \\ &\quad + \bar{g}_A(-p, -q, q, p) \bar{\psi}(p) \mathcal{O}_A \not{q} \mathcal{O}_A \psi(p)]. \end{aligned} \quad (2.31)$$

Next we evaluate the $\tilde{\partial}_t$ -derivative and switch to dimensionless momenta and couplings as well as renormalized fields again, such that

$$\begin{aligned} \frac{1}{2} \tilde{\partial}_t \text{STr} [\mathcal{P}_k^{-1} \mathcal{F}_k] &= - \frac{k^{d+1}}{\tilde{N}} \int_{p,q} \frac{\partial_t r_1(q^2) - \eta(q^2) r_1(q^2)}{Z(p^2)^{-1} q^2 [1 + r_1(q^2)]^2} \sum_A [g_A(-p, p, -q, q) N_f \text{tr}(\not{q} \mathcal{O}_A) \bar{\psi}(p) \mathcal{O}_A \psi(p) \\ &\quad + g_A(-p, -q, q, p) \bar{\psi}(p) \mathcal{O}_A \not{q} \mathcal{O}_A \psi(p)]. \end{aligned} \quad (2.32)$$

To extract a relation for η , we have to compare this to the left-hand side of Eq. (2.30), which becomes

$$\partial_t \Gamma_k[\psi, \bar{\psi}] = k^{d+1} \int_p Z(p^2) \eta(p^2) \bar{\psi}(p) \not{p} \psi(p) + \mathcal{O}([\bar{\psi} \psi]^2) \quad (2.33)$$

after rescaling of fields and momenta. To project out the relevant contributions, we take the second functional derivative and multiply by the momentum argument \not{P} , leading to

$$\frac{k^{-d-1}}{Z(P^2)} \not{P} \frac{\overrightarrow{\delta}}{\delta \bar{\psi}(P)} \partial_t \Gamma_k[\psi, \bar{\psi}] \frac{\overleftarrow{\delta}}{\delta \psi(P')} \Big|_{\psi, \bar{\psi}=0} = (2\pi)^d \delta(P - P') \eta(P^2) P^2 \mathbf{1}_\gamma, \quad (2.34)$$

where $\mathbf{1}_\gamma$ denotes the identity matrix in Dirac space. Let us perform the same transformation steps on Eq. (2.32). Here we obtain

$$\begin{aligned} &\frac{k^{-d-1}}{Z(P^2)} \not{P} \frac{\overrightarrow{\delta}}{\delta \bar{\psi}(P)} \frac{1}{2} \tilde{\partial}_t \text{STr} [\mathcal{P}_k^{-1} \mathcal{F}_k] \frac{\overleftarrow{\delta}}{\delta \psi(P')} \Big|_{\psi, \bar{\psi}=0} \\ &= - \frac{(2\pi)^d \delta(P - P')}{\tilde{N}} \int_q \frac{\partial_t r_1(q^2) - \eta(q^2) r_1(q^2)}{q^2 [1 + r_1(q^2)]^2} \sum_A [g_A(-P, P, -q, q) N_f \text{tr}(\not{q} \mathcal{O}_A) \not{P} \mathcal{O}_A \\ &\quad + g_A(-P, -q, q, P) \not{P} \mathcal{O}_A \not{q} \mathcal{O}_A]. \end{aligned} \quad (2.35)$$

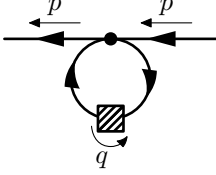


Figure 5: Self-energy diagram encoding the contributions from the four-fermion coupling that enter the anomalous dimension function.

Using the orthogonality property (2.5), we can pick out the contribution proportional to the identity, so that a comparison of (2.34) and (2.35) yields

$$\begin{aligned} \eta(p^2) = -\frac{1}{\tilde{N}} \int_q \frac{\partial_t r_1(q^2) - \eta(q^2) r_1(q^2)}{p^2 q^2 [1 + r_1(q^2)]^2} \sum_A \left[N_f \text{tr}(\not{p} \mathcal{O}_A) \frac{\text{tr}(\not{p} \mathcal{O}_A)}{d_\gamma} g_A(-p, p, -q, q) \right. \\ \left. + \frac{\text{tr}(\not{p} \mathcal{O}_A \not{q} \mathcal{O}_A)}{d_\gamma} g_A(-p, -q, q, p) \right]. \end{aligned} \quad (2.36)$$

The remaining Dirac-space traces on the right-hand side must then be evaluated for the particular model under study.

Self-energy diagram functionals. We can compactify the notation similarly to the case of the coupling functions by introducing diagram functionals for the two processes in Eq. (2.36). A pictorial representation is shown in Fig. 5. Due to Lorentz invariance, the Dirac traces in Eq. (2.36) will reduce to terms proportional to $p \cdot q$. The self-energy diagram functionals are given by

$$\Sigma^1[g; \eta](p^2) := -\frac{1}{\tilde{N}} \int_q \left(\frac{q \cdot p}{q^2 p^2} \right) \frac{\partial_t r_1(q^2) - \eta(q^2) r_1(q^2)}{[1 + r_1(q^2)]^2} g(-p, -q, q, p), \quad (2.37a)$$

$$\Sigma^2[g; \eta](p^2) := -\frac{1}{\tilde{N}} \int_q \left(\frac{q \cdot p}{q^2 p^2} \right) \frac{\partial_t r_1(q^2) - \eta(q^2) r_1(q^2)}{[1 + r_1(q^2)]^2} g(-p, p, -q, q). \quad (2.37b)$$

Observe that due to Lorentz invariance, these can only depend on p^2 even though the vector quantities enter on the right-hand side. With this definition, the anomalous dimension function in its general form can be written as

$$\eta(p^2) = \sum_A \{ a_1^A \Sigma^1[g_A; \eta](p^2) + a_2^A \Sigma^2[g_A; \eta](p^2) \}, \quad (2.38)$$

where the coefficients a_1^A and a_2^A are obtained from the Dirac traces in Eq. (2.36). In the pointlike limit, where g does not depend on the external momenta, the integrand is odd in q so that both diagram functionals vanish and consequently $\eta = 0$.

* * *

Our abstract analysis of momentum-dependent four-fermion interactions in this section revealed that there are in general four different types of processes or diagrams in terms of which the four-fermion vertices mutually contribute to their RG flows. We characterized them by the associated momentum transfer across the β function fermion loop and labeled them by the corresponding Mandelstam variables \mathfrak{s} , \mathfrak{t} , and \mathfrak{u} . As for the \mathfrak{s} -channel, we found in fact two distinct diagrams involving either one or two composite states of fermions, respectively. Regarding the generalized anomalous dimension, we observed that there exist in principle two different diagrams by which the four-fermion vertices contribute, involving either contracted or uncontracted propagating fermions.

In the following, we will apply these general findings to the Gross-Neveu and Thirring models, which were already briefly touched during the discussion of symmetries in the beginning of this section. We will begin with the Gross-Neveu model in the next section, which is the simplest type of four-fermion models and can serve as a testbed for the explicit analysis of momentum-dependent interactions.

3 Gross-Neveu model

The Gross-Neveu model [14] is a massless fermion system with a scalar four-fermion interaction, described by the microscopic action

$$S[\psi, \bar{\psi}] = \int d^d x \left[\bar{\psi}(x) i \not{d} \psi(x) + \frac{\bar{g}}{2N_f d_\gamma} (\bar{\psi}(x) \psi(x))^2 \right] \quad (3.1)$$

$$= - \int_p \bar{\psi}(p) \not{p} \psi(p) + \int_{p_i} \frac{\bar{g}}{2N_f d_\gamma} \bar{\psi}(-p_1) \psi(p_2) \bar{\psi}(-p_3) \psi(p_4) (2\pi)^d \delta(p_1 + p_2 + p_3 + p_4). \quad (3.2)$$

Originally introduced in its $(1+1)$ -dimensional form as a toy model for QCD [14], it has since been studied in a variety of contexts. Here we will be mostly interested in the $(2+1)$ -dimensional version, which has been used to examine, *e.g.*, models of graphene [15, 17–20] and high-temperature superconducting cuprates [21] in condensed matter physics, or asymptotic safety scenarios [30] and spontaneous chiral symmetry breaking [26, 27] in high-energy physics. Despite being the simplest model of four-fermion interactions, it has some intriguing properties and most notably a nontrivial, critical RG fixed point. In the following, we will mainly investigate its UV physics as sketched in the previous sections.

3.1 Flow of the four-point function

Effective action. We promote the couplings to functions of the external momenta, thus establishing a vertex expansion of the effective action. Moreover, we assume a momentum-dependent wave function renormalization again. Our ansatz for the effective average action in this section then reads

$$\Gamma_k[\psi, \bar{\psi}] = - \int_p Z(p^2) \bar{\psi}(p) \not{p} \psi(p) + \int_{p_2, p_3, p_4} \frac{\bar{g}(p_1, p_2, p_3, p_4)}{2\tilde{N}} \bar{\psi}(-p_1) \psi(p_2) \bar{\psi}(-p_3) \psi(p_4). \quad (3.3)$$

In principle, all the other vertices (2.3) compliant with the symmetries of the Gross-Neveu model will also be generated by the RG flow. In the pointlike approximation, it is a peculiarity of the Gross-Neveu vertex that this does in fact not happen when starting from a pure Gross-Neveu action like (3.3), *i.e.* the Gross-Neveu vertex forms an invariant subspace [31, 32, 95]. Although this changes for momentum-dependent interactions, the corrections are very small and will be explored in more detail in Section 4. For the time being, we stick with the reduced ansatz (3.3).

Flow equation. Plugging our ansatz (3.3) into the Wetterich equation (1.13), we can extract a flow equation for the dimensionless coupling function g according to the procedure described in Section 2.2. A detailed derivation is presented in Appendix B.3. We obtain

$$\partial_t g(p_i) = \left[d - 2 + 2\eta^{(4)}(p_i^2) + \sum_j p_j \cdot \nabla_{p_j} \right] g(p_i) - \tilde{N}_0 B^{\mathfrak{s}2}[g, g; \eta](p_i) + {}_0^2 B^{\mathfrak{s}1}[g, g; \eta](p_i). \quad (3.4)$$

At this point, we already notice that only the \mathfrak{s} -channel contributes to the flow of the Gross-Neveu coupling, although this is another peculiarity of the truncation and will change when we incorporate other interaction vertices (*cf.* Section 4). In a similar fashion, the Wetterich equation implies a relation between the generalized anomalous dimension and the coupling function as shown in Section 2.3. The computational details are collected in Appendix B.4, and we find that

$$\eta(p^2) = - \frac{1}{\tilde{N}} \int_q \frac{p \cdot q}{p^2 q^2} \frac{\partial_t r_1(q^2) - \eta(q^2) r_1(q^2)}{[1 + r_1(q^2)]^2} g(-p, -q, q, p) = \Sigma^1[g; \eta](p^2). \quad (3.5)$$

Eqs. (3.4) and (3.5) form a system of coupled integro-differential equations, whose general solution is unfortunately not known to us. Nevertheless, reducing its complexity by assuming certain dominant interaction channels will allow us to compute fixed point solutions and critical exponents of the momentum-dependent model.

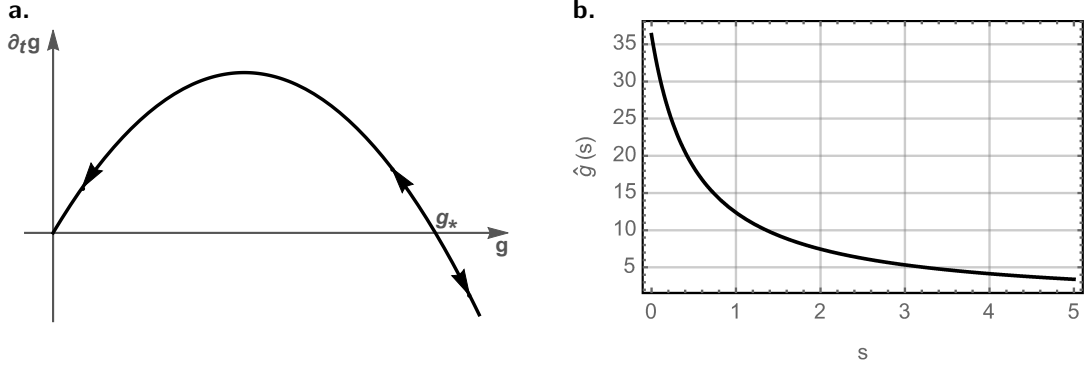


Figure 6: (a) Sketch of the β function of the Gross-Neveu coupling in the pointlike limit with arrows indicating the flow towards the infrared. Besides the Gaussian, there is one more nontrivial fixed point at some finite value $g_* > 0$; (b) effective four-fermion coupling at the Gross-Neveu fixed point in the bosonized formulation with $d = 3$, $\tilde{N} = 8$ as a function of the Mandelstam variable s .

Pointlike limit. The simplest approximation possible is of course the one of constant coupling, meaning that g does not depend on the external momenta. As shown in Eq. (2.29), this leaves us with the so-called pointlike limit, where $\eta = 0$ and

$$\partial_t g = (d-2)g - 4v_d \ell_1^{(F)d}(0;0) \frac{\tilde{N}-2}{\tilde{N}} g^2. \quad (3.6)$$

This β function is plotted in Fig. 6a. To extract fixed points of the model, we set the left-hand side to zero. Besides the trivial Gaussian fixed point, we find another, nontrivial fixed point where the coupling takes the value

$$g_* = \frac{d-2}{4v_d \ell_1^{(F)d}(0;0)} \frac{\tilde{N}}{\tilde{N}-2}. \quad (3.7)$$

Solving the linearized flow equation as described in Section 1.3, we find the associated critical exponent $\theta = d-2$. Hence the fixed point is IR-relevant in $d > 2$, as already apparent from the β function in Fig. 6a. On the other hand, the critical exponent of the Gaussian fixed point is $2-d$. Thus the nontrivial fixed point separates two different IR regimes, namely a weakly interacting one for theories starting at $g < g_*$ and a strongly interacting one for $g > g_*$, where in particular the chiral symmetry may be broken dynamically.

Let us point out once again that within the present truncation, only s -channel processes contribute to the flow of the Gross-Neveu coupling. In the next section, we will show that the s -channel is also the type of momentum dependence restored in a partially bosonized formulation of the pointlike model. Hence we will investigate the reduction of Eq. (3.4) to a pure s -channel dependence in great detail in the ensuing sections. Within this approximation, we will be able to solve the associated fixed point equation numerically and compute the corresponding spectra. In the limit of large N_f , we will even be able to derive the nontrivial fixed point solution and its spectrum analytically.

3.2 Partial bosonization

Before we study the momentum-dependent, purely fermionic model further, let us quickly summarize some literature results [19, 26, 27, 30, 61, 72] from derivative expansions in a partially bosonized version of the action (3.2). As we will see, this procedure allows one to partially recover the momentum dependence of the four-fermion vertex. Moreover, it gives direct access to the chiral condensate $\langle \bar{\psi} \psi \rangle$, making it particularly useful to address questions of dynamical symmetry breaking.

Hubbard-Stratonovich transformation. Correlation functions of the purely fermionic Gross-Neveu model (3.1) take the form

$$\langle A \rangle = \int \mathcal{D}\psi \mathcal{D}\bar{\psi} A \exp \left\{ - \int d^d x \left[\bar{\psi} i \not{\partial} \psi + \frac{\bar{g}}{2\bar{N}} (\bar{\psi} \psi)^2 \right] \right\}, \quad (3.8)$$

where A is an arbitrary operator of the fields ψ , $\bar{\psi}$. Here and in the following, we assume the integration measure to be properly normalized, such that $\langle 1 \rangle = 1$. Introducing a scalar, real-valued auxiliary field ϕ , we can equivalently express the correlator as

$$\langle A \rangle = \int \mathcal{D}\phi \mathcal{D}\psi \mathcal{D}\bar{\psi} A \exp \left\{ - \int d^d x \left[\bar{\psi} i \not{\partial} \psi + \frac{1}{2} \bar{m}^2 \phi^2 + i \bar{h} \bar{\psi} \phi \psi \right] \right\}. \quad (3.9)$$

Indeed, we can formally perform the Gaussian integral over ϕ in this equation and get back (3.8) upon identifying $\bar{g} = \bar{N} \bar{h}^2 / \bar{m}^2$. The step from Eq. (3.8) to Eq. (3.9) is known as a *Hubbard-Stratonovich transformation* [97, 98]. On the microscopic level, our model can thus be described equivalently by a mixed fermionic and bosonic theory characterized by the action

$$S[\phi, \psi, \bar{\psi}] = \int d^d x \left[\bar{\psi}(x) i \not{\partial} \psi(x) + \frac{1}{2} \bar{m}^2 \phi(x)^2 + i \bar{h} \bar{\psi}(x) \phi(x) \psi(x) \right] \quad (3.10)$$

$$= \int_p \left[\frac{1}{2} \bar{m}^2 \phi(-p) \phi(p) - \bar{\psi}(p) \not{\partial} \psi(p) \right] + \int_{p,p'} i \bar{h} \bar{\psi}(-p) \phi(-p - p') \psi(p). \quad (3.11)$$

Effective average action and flow equations. In the action (3.11), the field ϕ does not come with a kinetic term and is purely static. However, such a term will be created by the renormalization group flow as the scale k is lowered, and the auxiliary field ϕ will exhibit its own dynamics. As a matter of fact, it will eventually become the relevant degree of freedom in the IR regime, where it becomes the above mentioned order parameter for chiral symmetry breaking. Regarding our current interest in studying the momentum-dependent Gross-Neveu interaction, promoting ϕ to a dynamical field in the effective average action will allow it to carry momentum between pairs of $\psi\bar{\psi}$. This induces a momentum dependence of the resulting effective four-fermion interaction whose precise form we will investigate below. Therefore, our truncation of the effective average action for the partially bosonized model takes the form

$$\Gamma_k[\phi, \psi, \bar{\psi}] = \int_p \left[\frac{1}{2} \phi(-p) (Z_\phi p^2 + \bar{m}^2) \phi(p) - Z_\psi \bar{\psi}(p) \not{\partial} \psi(p) \right] + \int_{p,p'} i \bar{h} \bar{\psi}(-p) \phi(-p - p') \psi(p'). \quad (3.12)$$

This corresponds to the Gross-Neveu-Yukawa model in the *improved local potential approximation* (LPA'), where we only keep the very lowest order of the effective potential, namely the mass term $\bar{m}^2 \phi^2 / 2$. Of course, in order to increase precision, one would have to include higher truncations of the effective potential [30] or higher-order derivatives [61], but the present form suffices for the argument we are going to make.

Substituting the ansatz (3.12) into the Wetterich equation (1.13) leads to the β functions for the dimensionless coupling constants $m^2 := k^{-2} Z_\phi^{-1} \bar{m}^2$ and $h := k^{\frac{d-4}{2}} Z_\phi^{-1/2} Z_\psi^{-1} \bar{h}$ [30, 72],

$$\partial_t m^2 = (-2 + \eta_\phi) m^2 + 4 v_d \ell_1^{(F)d}(0; \eta_\psi) \bar{N} h^2, \quad (3.13a)$$

$$\partial_t h^2 = (d - 4 + \eta_\phi + 2\eta_\psi) h^2 + 8 v_d \ell_{1,1}^{(FB)d}(0, \tilde{m}^2; \eta_{\psi,k}, \eta_{\phi,k}) h^4. \quad (3.13b)$$

We also find the following relations for the anomalous dimensions of the boson and fermion fields:

$$\eta_\phi := -\partial_t \ln Z_\phi = \frac{8v_d}{d} \bar{N} m_4^{(F)d}(0, \eta_\psi) h^2, \quad (3.14)$$

$$\eta_\psi := -\partial_t \ln Z_\psi = \frac{8v_d}{d} m_{1,2}^{(FB)d}(0, m^2; \eta_\psi, \eta_\phi) h^2. \quad (3.15)$$

For the threshold functions $\ell_{n_1 n_2 \dots}^{(FB\dots)}$ and $m_{n_1 n_2 \dots}^{(FB\dots)}$, which encode the regularized propagation of virtual loop particles, we use the definitions and conventions of Ref. [32] again.

Fixed points. In order to find fixed points of the renormalization group flow, we set the left-hand sides of Eqs. (3.13a) and (3.13b) to zero and solve them together with Eqs. (3.14) and (3.15) for the anomalous dimensions. Besides the trivial Gaussian fixed point, we find a second, nontrivial fixed point with positive mass and Yukawa coupling. For instance, in $d = 3$ with $N_f = 2$ and $d_\gamma = 4$ using the linear regulator (1.10) we obtain

$$m_*^2 = 0.5168, \quad h_*^2 = 2.344, \quad \eta_{\phi,*} = 0.7829, \quad \eta_{\psi,*} = 0.0277. \quad (3.16)$$

Connection to the purely fermionic formulation. On the level of bare actions (3.2) and (3.11), we observed above that the connection between the fermionic and partially bosonized descriptions is made by identifying $\bar{g} = \tilde{N}h^2/\bar{m}^2$. This relation is expected to receive modifications due to the boson dynamics. To quantify them, we compute the equations of motion of the boson field, $\delta\Gamma_k/\delta\phi(q) = 0$, and find

$$\phi(-q) = -\frac{i\bar{h}_k}{Z_{\phi,k}q^2 + \bar{m}_k^2} \int_p \bar{\psi}(q+p)\psi(p). \quad (3.17)$$

Plugging this back into the Gross-Neveu-Yukawa action (3.12), we obtain a mean field approximation of the same structure as the fermionic Gross-Neveu action:

$$\begin{aligned} \Gamma_k[\bullet, \psi, \bar{\psi}] \simeq & - \int_p Z_\psi \bar{\psi}(p)\psi(p) \\ & + \frac{1}{2} \int_{p_2, p_3, p_4} \frac{\bar{h}^2}{Z_\phi(p_3 + p_4)^2 + \bar{m}^2} \bar{\psi}(p_2 + p_3 + p_4)\psi(p_2)\bar{\psi}(-p_3)\psi(p_4). \end{aligned} \quad (3.18)$$

Comparing to the purely fermionic description, we see that we need to identify

$$\hat{\bar{g}} = \frac{\tilde{N}\bar{h}^2}{Z_\phi(p_3 + p_4)^2 + \bar{m}^2} \quad \text{or, in dimensionless quantities,} \quad \hat{g}(\mathfrak{s}) = \frac{\tilde{N}h^2}{\mathfrak{s} + m^2}, \quad (3.19)$$

in order to reach equality. Thus the bosonized formulation indeed enhances the pointlike interaction by a transfer of momentum across the \mathfrak{s} -channel. For the fixed point parameters (3.16), the resulting coupling function is plotted in Fig. 6b.

3.3 s -Channel approximation

In its most general form, the coupling g will be a function of up to six linearly independent Lorentz invariants. However, of all possible choices, the Mandelstam variable $\mathfrak{s} = (p_1 + p_2)^2 = (p_3 + p_4)^2$ stands out for two reasons. On the one hand, we saw in Section 3.1 that it is the only contribution from the external momenta entering the loops in (3.4). In our present truncation, the t - and u -channels are suppressed. On the other hand, it is the natural encoding of momentum dependence in the bosonized model featuring a Gross-Neveu-Yukawa coupling [72], as we showed in Section 3.2. In the remainder of this section, we will therefore consider a coupling function $g = g(\mathfrak{s})$.

Diagram functionals and momentum configurations. First, let us have a look at the diagram functionals (2.26) again and work out what they become in the \mathfrak{s} -channel approximation. We choose the coordinate system for the loop integrals such that p^m points along the z -axis and switch to spherical coordinates. The threshold kernel $\frac{a_1}{a_2} K_1^{(F)}$ defined in Eq. (2.22) then only depends on the square of the momentum transfer and the angle between q and p , which we parametrize as $u := \cos \sphericalangle(p, q)$. Absorbing an additional factor of $1/(2\pi)^d$, we define the abbreviation

$$\begin{aligned} \frac{a_1}{a_2} K(\mathfrak{m}, q, u; \eta) := & \frac{1}{(2\pi)^d} \left[\frac{(a_1 + a_2)q^2 + a_1 q\sqrt{\mathfrak{m}}u - a_2 q^2 u^2}{q^2(q^2 + \mathfrak{m} + 2q\sqrt{\mathfrak{m}}u)} \right] \\ & \times \frac{\partial_t r_1(q^2) - \eta(q^2)r_1(q^2)}{[1 + r_1(q^2)]^2 [1 + r_1(q^2 + \mathfrak{m} + 2q\sqrt{\mathfrak{m}}u)]} \end{aligned} \quad (3.20)$$

for the threshold kernel. In an abuse of notation, we use the same symbol q for both the loop momentum vector and its magnitude, but the meaning should be clear from the context and can

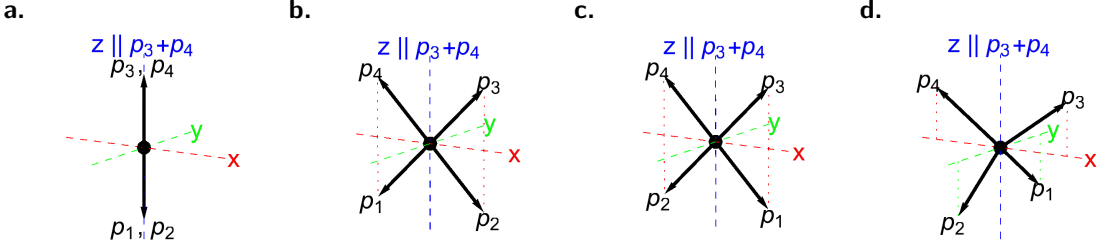


Figure 7: Example momentum configurations used in the computation of loop integrals in the \mathfrak{s} -channel approximation. All momenta have equal magnitude. In the parallel configuration (a), the momenta are aligned along the same direction. In the two orthogonal configurations (b) and (c), all momenta lie in one plane (the x - z plane), and one of the Mandelstam variables t or u vanishes. We refer to (b), where $u = 0$, as the t -favored, and to (c) with $t = 0$ as the u -favored orthogonal configuration. In the symmetric configuration (d), the angle between any two momentum vectors is the same, known as the tetrahedral angle $\arccos(-\frac{1}{3}) \approx 109.47^\circ$.

be read off the measure of the associated loop integral. If the coupling functions depend solely on \mathfrak{s} , the diagram functionals become

$$\frac{a_1}{a_2} B^{\mathfrak{s}2}[g_1, g_2; \eta](p_i) = \frac{2}{\tilde{N}} g_1(\mathfrak{s}) g_2(\mathfrak{s}) \sigma_{d-2} \int d(q, u) \frac{a_1}{a_2} K(\mathfrak{s}, q, u; \eta), \quad (3.21a)$$

$$\frac{a_1}{a_2} B^{\mathfrak{s}1}[g_1, g_2; \eta](p_i) = \frac{1}{\tilde{N}} g_1(\mathfrak{s}) \int d(q, u, \Omega) \frac{a_1}{a_2} K(\mathfrak{s}, q, u; \eta) [g_2([q + p_3]^2) + g_2([q + p_4]^2)], \quad (3.21b)$$

$$\begin{aligned} \frac{a_1}{a_2} B^t[g_1, g_2; \eta](p_i) &= \frac{1}{\tilde{N}} \int d(q, u, \Omega) \frac{a_1}{a_2} K(t, q, u; \eta) \\ &\quad \times [g_1([q - p_1]^2) g_2([q + p_2]^2) + g_1([q - p_4]^2) g_2([q + p_3]^2)], \end{aligned} \quad (3.21c)$$

$$\begin{aligned} \frac{a_1}{a_2} B^u[g_1, g_2; \eta](p_i) &= \frac{1}{\tilde{N}} \int d(q, u, \Omega) \frac{a_1}{a_2} K(u, q, u; \eta) \\ &\quad \times [g_1([q - p_1]^2) g_2([q + p_2]^2) + g_1([q - p_3]^2) g_2([q + p_4]^2)]. \end{aligned} \quad (3.21d)$$

For the measure of integration, we introduced the shorthand

$$\int d(q, u, \Omega) \equiv \int_0^\infty dq q^{d-1} \int_{-1}^1 du (1 - u^2)^{\frac{d-3}{2}} \int_{S_{d-2}} d\Omega \quad (3.22)$$

with Ω being the solid angle of the $(d-2)$ -dimensional unit sphere. We also defined $\sigma_d := 2\pi^{(d+1)/2}/\Gamma(\frac{d+1}{2})$ as the surface of the d -dimensional unit sphere.

We observe that the $\mathfrak{s}1$, t , and u diagram functionals are not closed under the reduction to pure \mathfrak{s} -channel dependence. Via the arguments entering g under the integral sign, there remains a dependence on other Lorentz invariant combinations of the external momenta, which we fix by choosing a particular configuration for them. To ensure meaningfulness of the approximation, results should of course be stable upon variation of the configuration. We will address this issue again in Section 3.5. In particular, we will use the four configurations depicted in Fig. 7, which are chosen in order to work out the influences of the different channels as clearly as possible. The magnitude of all momenta is the same in any of them, $p_i^2 = p^2 = \frac{\mathfrak{s}}{2+2\cos\angle(p_3, p_4)}$. In the parallel configuration in Panel (a), $t = u = 0$, leading to the “purest” \mathfrak{s} -dependence. The orthogonal configurations in Panels (b) and (c) accentuate either of the t - or u -channels against the other: In the t -favored configuration (b), we have $t = \mathfrak{s}$ and $u = 0$, whereas in the u -favored one (c), $t = 0$ and $u = \mathfrak{s}$. In the symmetric configuration in Panel (d), the angle between any two momentum vectors is the same, *i.e.* $\cos\angle(p_i, p_j) = -\frac{1}{3}$ ($i \neq j$), so that $\mathfrak{s} = t = u$.

As far as the self-energy diagram functionals (2.37b) are concerned, we notice that $\Sigma^2 \equiv 0$ in the \mathfrak{s} -channel approximation. For the other diagram we obtain

$$\Sigma^1[g; \eta](p^2) = \frac{1}{\tilde{N}} \int_q M(p^2, q, u; \eta) g\left(q^2 + p^2 + 2q\sqrt{p^2}u\right) \quad (3.23)$$

with kernel

$$M(p^2, q, u; \eta) := -\frac{\sigma_{d-2}}{(2\pi)^d} \left(\frac{u}{\sqrt{p^2}q} \right) \frac{\partial_t r_1(q^2) - \eta(q^2)r_1(q^2)}{[1 + r_1(q^2)]^2}. \quad (3.24)$$

We remark that there is no ambiguity regarding the momentum configuration here because the self-energy depends on one parameter p^2 only and is therefore closed under the \mathfrak{s} -channel reduction.

Flow equations. Plugging in the diagram functionals in the \mathfrak{s} -channel approximation, the flow equation (3.4) for the Gross-Neveu coupling reads

$$\begin{aligned} \partial_t g(\mathfrak{s}) &= \left[d - 2 + 2\eta^{(4)}(p_i^2) \right] g(\mathfrak{s}) + 2\mathfrak{s}g'(\mathfrak{s}) \\ &\quad - \frac{2}{\tilde{N}} g(\mathfrak{s}) \int d(q, u, \Omega) {}_0^1 K(\mathfrak{s}, q, u; \eta) [\tilde{N} g(\mathfrak{s}) - g([q+p_3]^2) - g([q+p_4]^2)]. \end{aligned} \quad (3.25)$$

Similarly, we apply the \mathfrak{s} -channel reduction of g to Eq. (3.5) for the anomalous dimension function and obtain

$$\eta(p^2) = \frac{1}{\tilde{N}} \int d(q, u) M(p^2, q, u; \eta) g\left(q^2 + p^2 + 2q\sqrt{p^2}u\right). \quad (3.26)$$

Finding and characterizing renormalization group fixed points of the system defined by these two coupled integro-differential equations will be our aim in the next two sections. In the limit of infinite flavor number N_f , we will derive the exact analytic solution in Section 3.4. For finite N_f , unfortunately, we will not be able to solve the associated fixed point equations analytically, but will compute numerical solutions using pseudospectral methods in Section 3.5. Before we turn to finding such solutions, we would like to add a few remarks regarding their asymptotic behavior.

Asymptotics of the fixed point solution. Fixed points of the renormalization group flow are characterized by invariant coupling functions, *i.e.* $\partial_t g_* = 0$. As usual, we are interested in nontrivial fixed point solutions of Eqs. (3.25) and (3.26). To investigate their asymptotics, we first take a look at the g -kernel (3.20). As $\mathfrak{s} \rightarrow \infty$,

$$\begin{aligned} \frac{a_1}{a_2} K(\mathfrak{s}, q, u; \eta) &\sim \frac{1}{(2\pi)^d} \frac{\partial_t r_1(q^2) - \eta(q^2)r_1(q^2)}{[1 + r_1(q^2)]^2 [1 + r_1(q^2 + \mathfrak{s} + 2q\sqrt{\mathfrak{s}}u)]} \\ &\times \left[\frac{a_1 u}{q} \mathfrak{s}^{-1/2} + (a_1(1 - 2u^2) + a_2(1 - u^2)) \mathfrak{s}^{-1} \right. \\ &\quad - (a_1(3 - 4u^2) + 2a_2(1 - u^2)) uq\mathfrak{s}^{-3/2} \\ &\quad \left. + (a_1(1 - 8u^2 + 8u^4) + a_2(1 - 5u^2 + 4u^4)) q^2\mathfrak{s}^{-2} + \dots \right] \end{aligned} \quad (3.27)$$

Although this relation still depends on the precise form of the regulator shape function r_k , we have $r_k(x \rightarrow \infty) = 0$ in any case, so that the leading order of the kernel will decay as $\mathfrak{s}^{-1/2}$, and in general all subsequent powers of $\mathfrak{s}^{-1/2}$ will occur.

Let us assume that the fixed point coupling g_* is a bounded function of the Mandelstam variable \mathfrak{s} , which is suggested by partial bosonization as well as the large- N_f behavior to be studied in the next section, and also hinted at by general considerations regarding the large-momentum behavior of vertex functions [99–102]. For bounded g_* , the above expansion of the kernel implies that the fluctuation term in (3.25) is suppressed by at least $\mathfrak{s}^{-1/2}$ compared to the scaling term. In addition, the η -kernel $M(p^2, q, u; \eta) \sim (p^2)^{-1/2}$, *cf.* Eq. (3.24). Relation (3.26) then tells us that $\eta(p^2) \rightarrow 0$ in the limit $p^2 \rightarrow \infty$. All in all, we obtain an asymptotic relation for fixed point solutions g_* ,

$$2\mathfrak{s}g'_*(\mathfrak{s}) \sim (2 - d)g_*(\mathfrak{s}) \quad (\mathfrak{s} \rightarrow \infty), \quad (3.28)$$

which immediately leads to

$$g_*(\mathfrak{s}) \sim \mathfrak{s}^{\frac{2-d}{2}} \quad (\mathfrak{s} \rightarrow \infty). \quad (3.29)$$

This is in contrast to the mean-field result in the partially bosonized formulation, where we found $\hat{g}_*(\mathfrak{s}) \sim \mathfrak{s}^{-1}$ regardless of the dimension, and which only agrees with the above result in $d = 4$. In $d = 3$, which is the case of most interest to us, we get $g_*(\mathfrak{s}) \sim \mathfrak{s}^{-1/2}$.

Regarding the anomalous dimension function (3.26), its asymptotic behavior follows from the asymptotics of the kernel M and the coupling function, implying

$$\eta_*(p^2) \sim (p^2)^{\frac{1-d}{2}}. \quad (3.30)$$

In $d = 3$, we thus have $\eta_*(p^2) \sim p^{-2}$.

Connection to the bosonized formulation. Let us quickly come back to the partially bosonized model and explore how the flow equations (3.13a) and (3.13b) for the boson mass and Yukawa coupling connect to the purely fermionic flow (3.25) in the \mathfrak{s} -channel approximation. We already observed in the previous section that the bosonized formulation studied there encodes some of the \mathfrak{s} -channel dependence of the coupling, *cf.* Eq. (3.19). We can compute the inherited flow of this effective g -coupling by taking the ∂_t -derivative and substituting the β functions (3.13) of m^2 and h^2 , leading to

$$\begin{aligned} \partial_t \hat{g}(\mathfrak{s}) &= \tilde{N} \left[\frac{\partial_t h^2}{\mathfrak{s} + m^2} - \frac{h^2 \partial_t m^2}{(\mathfrak{s} + m^2)^2} \right] \\ &= \left[d - 4 + \eta_\phi + 2\eta_\psi + \frac{2 - \eta_\phi}{1 + \frac{\mathfrak{s}}{m^2}} \right] \hat{g}(\mathfrak{s}) + \frac{1}{\tilde{N}} \tilde{\partial}_t \int_q \frac{\tilde{N} \hat{g}(\mathfrak{s})^2 - 2\hat{g}(\mathfrak{s})\hat{g}\left(q^2[1 + r_1^{(B)}(q^2)]\right)}{q^2 \left[1 + r_1^{(F)}(q^2)\right]^2}. \end{aligned} \quad (3.31)$$

The $\tilde{\partial}_t$ -derivative here acts on both $r_k^{(F)}$ and $r_k^{(B)}$. In order to reach the purely fermionic limit, we need to decouple the boson from the theory by letting $m^2 \rightarrow \infty$ while keeping \hat{g} fixed. This leads back to the static Hubbard-Stratonovich transformation (3.11). At the same time, we let $r_k^{(B)} \rightarrow 0$ because there is no dynamical boson to be regularized any longer. Consequently, we are left with

$$\partial_t \hat{g}(\mathfrak{s}) = (d - 2 + 2\eta_\psi) \hat{g}(\mathfrak{s}) + \frac{1}{\tilde{N}} \tilde{\partial}_t \int_q \frac{1}{q^2 \left[1 + r_1^{(F)}(q^2)\right]^2} [\tilde{N} \hat{g}(\mathfrak{s})^2 - 2\hat{g}(\mathfrak{s})\hat{g}(q^2)], \quad (3.32)$$

where the $\tilde{\partial}_t$ -derivative now acts on $r_k^{(F)}$ exclusively. Comparing to (3.25), we see that this is indeed the \mathfrak{s} -channel flow equation of the purely fermionic model in the limit $\mathfrak{s} \ll 1$. In a similar fashion, we can re-express relation (3.15) for the fermion anomalous dimension in the bosonized model in terms of the effective coupling \hat{g} :

$$\eta_\psi = \frac{2}{\tilde{N}} \tilde{\partial}_t \int_q \frac{(p \cdot q)^2}{p^2 q^2} \frac{\hat{g}'\left(q^2[1 + r_1^{(B)}(q^2)]\right)}{1 + r_1^{(F)}(q^2)}. \quad (3.33)$$

At the same time, we can evaluate the anomalous dimension (3.26) in the purely fermionic model as $p^2 \rightarrow 0$ and find

$$\eta(0) = \frac{2}{\tilde{N}} \tilde{\partial}_t \int d(q, u) \frac{\sigma_{d-2}}{(2\pi)^d} u^2 \frac{g'(q^2)}{1 + r_1^{(F)}(q^2)}. \quad (3.34)$$

Letting $r_k^{(B)} \rightarrow 0$ in (3.33) yields a match of both equations, thus establishing the connection between the purely fermionic and the partially bosonized description also for the anomalous dimension function.

3.4 Large- N_f limit

Fixed point solution. The limit of infinite flavor number, $N_f \rightarrow \infty$ (and hence $\tilde{N} \rightarrow \infty$), is a convenient starting point for the computation of fixed point solutions because it simplifies Eq. (3.25) dramatically. Considering the flow of g , we observe that only the $\mathfrak{s}2$ -diagram survives as $\tilde{N} \rightarrow \infty$. Moreover, we immediately infer from Eq. (3.26) that $\eta(p^2) = 0$ in this limit. The flow equation (3.25) becomes

$$\partial_t g(\mathfrak{s}) = (d - 2)g(\mathfrak{s}) + 2\mathfrak{s}g'(\mathfrak{s}) - 2\frac{a_1}{a_2}K(\mathfrak{s})g(\mathfrak{s})^2, \quad (3.35)$$

where we introduced yet another reduction of the threshold kernel by integrating over the loop momentum, *i.e.*

$$\int d(q, u) \frac{a_1}{a_2} K(\mathfrak{s}, q, u; 0). \quad (3.36)$$

In the present case, $a_1 = 1$ and $a_2 = 0$ in Eq. (3.35). Nevertheless, we consider the more general situation with arbitrary (real) a_1 and a_2 as it will turn out useful later when studying the large- N_f limit of the Gross-Neveu-Thirring model. The associated fixed point equation is

$$2\mathfrak{s} g'_*(\mathfrak{s}) + (d-2)g_*(\mathfrak{s}) - 2\frac{a_1}{a_2} K(\mathfrak{s}) g_*(\mathfrak{s})^2 = 0. \quad (3.37)$$

The solution of this nonlinear differential equation is

$$g_*(\mathfrak{s}) = \frac{\mathfrak{s}^{-\frac{d-2}{2}}}{g_\infty + \int_{\mathfrak{s}}^\infty dx x^{-d/2} \frac{a_1}{a_2} K(x)}, \quad (3.38)$$

as can be verified straightforwardly by plugging it back into Eq. (3.37). For the current model, $g_\infty > 0$ is an *a priori* arbitrary constant, meaning that we obtain a one-parameter family of potential fixed-point solutions. In fact, even the value $g_\infty = 0$ leads to a well-defined coupling function for all $\mathfrak{s} \geq 0$, but its asymptotic behavior changes qualitatively because $g_*(\mathfrak{s}) \sim \mathfrak{s}$ if $g_\infty = 0$ whereas $g_*(\mathfrak{s}) \sim \mathfrak{s}^{-\frac{d-2}{2}}$ if $g_\infty > 0$. For $g_\infty < 0$, due to positivity of the integral, the expression would develop a pole. At $\mathfrak{s} = 0$, we obtain

$$g_*(0) = \frac{d-2}{2\frac{a_1}{a_2} K(0)} = \frac{d-2}{4v_d (a_1 + \frac{d-1}{d} a_2) \ell_1^{(F)}(0; 0)}, \quad (3.39)$$

making use of (2.23) in the second equality. This coincides with the fixed point position for $N_f = \infty$ in the pointlike limit (*cf.* Eq. (3.7)). For the linear regulator (1.10), the remaining integral in (3.37) can be evaluated analytically; we will give the solution in $d = 3$ and for $a_1 = 1$, $a_2 = 0$ here. The Heaviside function inside the regulator requires us to split the domain into three regions. For $0 \leq \mathfrak{s} < 1$, we find

$$g_*(\mathfrak{s}) = \frac{144\pi^2 \sqrt{\mathfrak{s}}}{3(\pi^2(48g_\infty-3)+1)\mathfrak{s}-36\mathfrak{s} \text{Li}_2(-\sqrt{\mathfrak{s}})+4\mathfrak{s}^{3/2}+6(4\mathfrak{s}^{3/2}+3\mathfrak{s}+1) \ln(\sqrt{\mathfrak{s}}+1)-18\mathfrak{s}^2+42\sqrt{\mathfrak{s}}}; \quad (3.40a)$$

for $1 \leq \mathfrak{s} < 4$,

$$g_*(\mathfrak{s}) = \frac{144\pi^2 \sqrt{\mathfrak{s}}}{3(\pi^2(48g_\infty-3)+1)\mathfrak{s}-36\mathfrak{s} \text{Li}_2(-\sqrt{\mathfrak{s}})-4\mathfrak{s}^{3/2}+24\mathfrak{s}^{3/2} \ln\left(\frac{1}{\sqrt{\mathfrak{s}}}+\frac{1}{\mathfrak{s}}\right)+6\mathfrak{s}^2+18\sqrt{\mathfrak{s}}+6(3\mathfrak{s}+1) \ln(\sqrt{\mathfrak{s}}+1)+8}; \quad (3.40b)$$

and for $\mathfrak{s} \geq 4$,

$$g_*(\mathfrak{s}) = \frac{24\pi^2 \sqrt{\mathfrak{s}}}{2\left(12\pi^2g_\infty\mathfrak{s}-6\mathfrak{s} \text{Li}_2\left(\frac{1}{\sqrt{\mathfrak{s}}}\right)+4\mathfrak{s}^{3/2} \text{arccoth}(1-2\mathfrak{s})+5\sqrt{\mathfrak{s}}+(3\mathfrak{s}+1) \text{arccoth}(\sqrt{\mathfrak{s}})\right)+3\mathfrak{s} \text{Li}_2\left(\frac{1}{\mathfrak{s}}\right)}. \quad (3.40c)$$

Arguably, this is not very enlightening at first glance. The symbol Li_2 denotes the polylogarithm of order 2. Example plots of the solution for different choices of g_∞ are shown in Fig. 8. An important observation is that the solution (3.40) is not analytic in \mathfrak{s} . In particular, expanding around $\mathfrak{s} = 0$, we find

$$\begin{aligned} g_*(\mathfrak{s}) = & 3\pi^2 + \frac{9\pi^4}{16}(1-16g_\infty)\mathfrak{s}^{1/2} + \frac{3\pi^2}{256} [9\pi^4(1-16g_\infty) - 320] \mathfrak{s} \\ & + \frac{9\pi^2}{4096} [384 - \pi^2(1-16g_\infty)(640 + 9\pi^4(1-16g_\infty)^2)] \mathfrak{s}^{3/2} + \mathcal{O}(\mathfrak{s}^2). \end{aligned} \quad (3.41)$$

Crucially, this is not a peculiarity caused by the non-analyticity of the regulator as one might think at first sight. Instead, the kernel (3.20) produces half-integer powers of \mathfrak{s} regardless of the regulator shape function. The decisive part is the square bracket in the first line of this equation. We can expand this term around $\mathfrak{m} = \mathfrak{s} = 0$ and obtain

$$\begin{aligned} \frac{(a_1 + a_2)q^2 + a_1 q \sqrt{\mathfrak{s}} u - a_2 q^2 u^2}{q^2 (q^2 + \mathfrak{s} + 2q\sqrt{\mathfrak{s}}u)} \sim & [a_1 + (1-u^2)a_2] \frac{1}{q^2} - [a_1 + 2(1-u^2)a_2] u \frac{\sqrt{\mathfrak{s}}}{q^3} \\ & - [(1-2u^2)a_1 + (1-5u^2+4u^4)a_2] \frac{\mathfrak{s}}{q^4} \\ & + [(3-4u^2)a_1 + (4-12u^2+8u^4)a_2] u \frac{\mathfrak{s}^{3/2}}{q^5} + \mathcal{O}(\mathfrak{s}^2). \end{aligned} \quad (3.42)$$

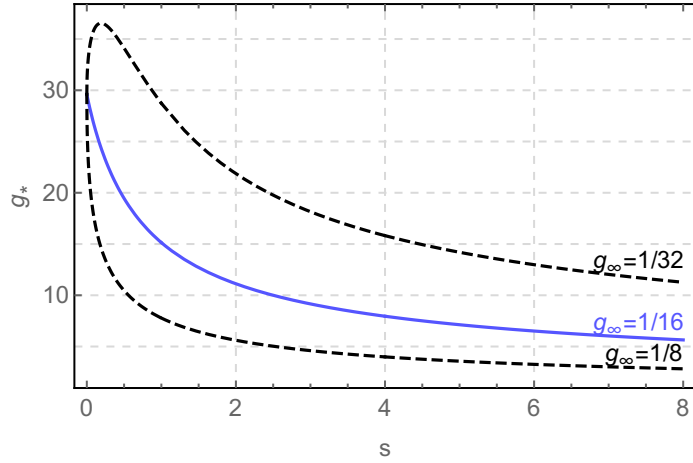


Figure 8: Large- N_f solutions for the nontrivial fixed point in the Gross-Neveu model for three different choices of the parameter g_∞ . The value $g_\infty = \frac{1}{16}$ stands out because it renders g_* maximally regular at $s = 0$ and defines the pointwise largest solution that does not develop a local maximum for $s > 0$.

Hence the expansion necessarily involves half-integer powers of the Mandelstam variable s . We observe that these half-integer powers always come with odd powers of the angular cosine u . Nevertheless, this does not imply that the terms vanish upon integration because the series (3.42) is not integrable term-by-term. Rather every additional power of \sqrt{s} in the numerator implies a complementary power of q in the denominator, so that the loop integrals of the individual terms diverge beyond linear order.

Up to linear order, on the contrary, the integrals are saved by the regulator terms in the second line of Eq. (3.20). Generically, the fermionic regulator shape function goes like $r_1(q^2) \sim 1/q$ for $q^2 \ll 1$. The overall contribution of the regulator terms is thus of order q^2 for small loop momenta. Along with the dimensional q^2 term from the integration measure, this removes the divergences up to the order s term in Eq. (3.42). This also explains the maximum regularity property satisfied by the numerical finite- N_f solutions to be computed below and enforced in the large- N_f limit because the term of order \sqrt{s} then indeed vanishes due to the corresponding integrand being odd in u .

The non-analyticity of g_* at $s = 0$ may seem a bit inconvenient because we intuitively connect it to the pointlike limit. However, we remember that the momentum-dependent couplings render the interaction nonlocal. Moreover, the variable s itself becomes rather singular as it approaches 0. In fact, even if $s = 0$, the external momenta may be arbitrarily large if p_3 and p_4 (and likewise p_1 and p_2) are aligned antiparallel. Due to the angular dependence, there is no direct connection between the Mandelstam variable s and the magnitude of the external momenta p_i^2 . In other words, $p_i^2 \rightarrow 0$ for all i implies $s \rightarrow 0$ and $s \rightarrow \infty$ implies $p_i^2 \rightarrow \infty$ for at least one i , but *not* vice versa.

Nevertheless, it is reasonable to demand a *maximum regularity* condition for the fixed point solutions by requiring as many derivatives to exist in $s = 0$ as possible. On the one hand, we will observe in the next section that this property is automatically satisfied by the numerical solutions for finite N_f . On the other hand, the integrals over the expanded kernel (3.20) with the expansion (3.42) do converge up to the power s^1 . In the present case, maximum regularity in this sense is obtained for $g_\infty = \frac{1}{16}$ such that the \sqrt{s} term vanishes. This is also the smallest value for g_∞ such that the fixed point function does not exhibit a local maximum at some finite value $s > 0$. The corresponding fixed point function is highlighted in Fig. 8.

Critical exponents. The great importance of renormalization group fixed points stems from the fact that they constitute the topology of the theory space and separate the different regimes of IR physics from each other. As we saw in Section 1.3 this is achieved by the relevant and irrelevant directions associated with the fixed point. To find the critical exponents, we perturb around the fixed point solution with an ansatz $g(s) = g_*(s) + e^{-\theta t} \varepsilon(s)$. Linearizing the flow equation (3.35) in ε yields the eigenvalue equation

$$-\theta \varepsilon(s) = (d - 2) \varepsilon(s) + 2s \varepsilon'(s) - 4 \frac{a_1}{a_2} K(s) g_*(s) \varepsilon(s), \quad (3.43)$$

whose solution is readily obtained as

$$\varepsilon(\mathfrak{s}) = C g_*(\mathfrak{s})^2 \mathfrak{s}^{\frac{d-2-\theta}{2}}, \quad C = \text{const.} \quad (3.44)$$

Requiring the solution to be finite in $\mathfrak{s} = 0$ restricts the spectrum to $\text{Re } \theta \leq d-2$. If we additionally demand for maximum regularity, the critical exponents become quantized with spacing 2, *i.e.* $\theta = 1, -1, -3, -5, \dots$, which is the same spectrum as found in the large- N_f limit of the bosonized theory except that there the eigenvalue -1 occurs twice [30]. The situation that quantization of the spectrum is only achieved after an additional analyticity requirement is also found for derivative expansions of scalar field theories [103, 104]. Linearized flow equations of the form (3.43) generically admit solutions for continuous values of θ *because* they are linear. Put differently, the seeming emergence of a continuous spectrum is an artifact of the linearization. In the field-dependent setting of Ref. [104] it is shown that the eigenperturbations must be polynomial in the field or, more generally, uniformly convergent over the entire domain for the continuum limit to be well-defined. Therefore, maximum regularity is a natural requirement for the eigenperturbations in our momentum-dependent description. We will come back to the implications of non-analytic perturbations when studying the spectra for finite flavor numbers in Section 3.6.

3.5 Fixed points for finite flavor numbers

After this digression on the limit of infinite flavor number, let us resume with the finite- N_f case described by Eqs. (3.25) and (3.26). In particular, the corresponding fixed point equation for the coupling function is

$$0 = \left[d - 2 + 2\eta^{(4)}(p_i^2) \right] g(\mathfrak{s}) + 2\mathfrak{s}g'(\mathfrak{s}) - \frac{2}{\tilde{N}} g(\mathfrak{s}) \int d(q, u, \Omega) {}_0^1 K(\mathfrak{s}, q, u; \eta) [\tilde{N} g(\mathfrak{s}) - g([q+p_3]^2) - g([q+p_4]^2)], \quad (3.45)$$

which has to be solved along with Eq. (3.26) for the anomalous dimension function. Owing to the nonvanishing anomalous dimension and the extra integrals involving the coupling, the situation is a bit more involved and we cannot provide a general analytic solution. Our aim in this section is thus to compute approximate numerical solutions. The integro-differential structure of the equation and the non-analyticity of the integral kernels constitute quite challenging premises for any numerical calculation. Notwithstanding, the pseudospectral method using Chebyshev rational functions [105, 106] turned out to be a versatile and robust tool to obtain solutions to arbitrary accuracy, at least in principle. As an example from the FRG context, it has been used successfully to obtain high-accuracy solutions of effective potentials for various model systems [61, 107–112]. Here we will focus our numerical analysis on systems in $d = 3$ spacetime dimensions. The solutions presented in this section all use the exponential-type regulator (1.11) because it showed faster decrease of the residuals with the expansion order than the regulator (1.12). The linear regulator (1.10) is not suited for the numerical studies carried out here because it implies non-smooth integrands in Eqs. (3.45).

Expansion in Chebyshev rational functions. The basic idea of our approach is to expand the coupling and anomalous dimension functions in terms of a complete set of basis functions and truncate the resulting series at some finite order. To be precise, we will use the Chebyshev rational functions R_n as our basis set on $[0, \infty)$, which are obtained from the Chebyshev polynomials of the first kind T_n by a compactification of the semi-infinite interval,

$$R_n(x) := T_n \left(\frac{x - L}{x + L} \right). \quad (3.46)$$

The parameter L is arbitrary, but fixed; it should typically be on the order of the length scales of the function to be modeled [105]. The first few of the R_n are plotted in Fig. 9a. By definition, the Chebyshev rational functions inherit some pleasant and neat properties from their polynomial parents, such as analyticity, boundedness, and orthogonality. Most importantly, the Chebyshev series is guaranteed to converge on the entire domain if the expanded function is square-integrable

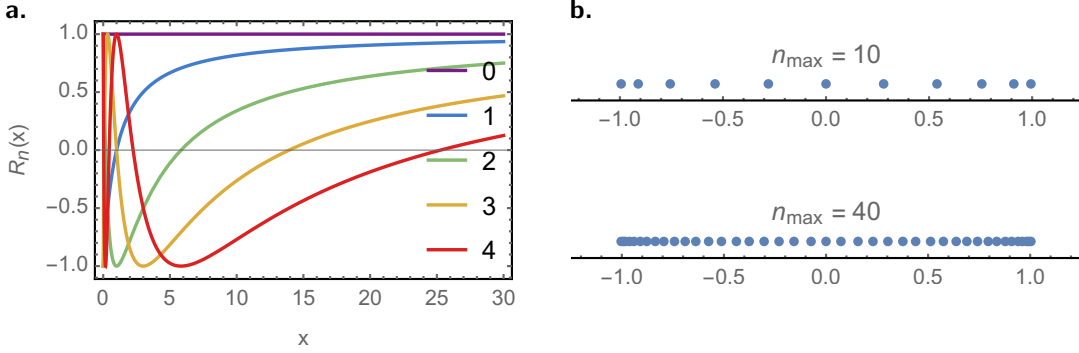


Figure 9: (a) Chebyshev rational functions R_n up to order 4; (b) compactified collocation grid points for expansion orders $n_{\max} = 10$ and $n_{\max} = 40$. The relation to the grid points for the Chebyshev rational functions is given by the compactification $x = L(1 + x_{\text{comp}})/(1 - x_{\text{comp}})$.

[105, 113], in contrast to, for instance, Taylor series, which converge only in a disc up to the closest singularity in the complex plane. We collected an overview of relevant properties and relations in Appendix C. Following the sketched idea, we expect to be able to write the coupling and anomalous dimension functions in the form

$$g_*(\mathfrak{s}) = \sum_{n=0}^{n_{\max}^g} g_n P_n(\mathfrak{s}), \quad \eta_*(p^2) = \sum_{n=0}^{n_{\max}^{\eta}} \eta_n P_n(p^2) \quad (3.47)$$

with coefficients g_n and η_n to be determined. Here the P_n may either be the Chebyshev rational functions themselves, $P_n(x) = R_n(x)$, which we will refer to as the identity (id) parametrization, or a square-root (sqrt) parametrized variant $P_n(x) = R_n(\sqrt{x})$ allowing for half-integer powers of the argument. This sqrt parametrization is obviously motivated by the large- N_f limit (3.41) and the asymptotic relation (3.29), both of which suggest that the coupling function will generally be only analytic in $\sqrt{\mathfrak{s}}$ rather than \mathfrak{s} , especially in $d = 3$. Technically, this also holds for the anomalous dimension function (3.26), but here the non-analyticity is “milder” in a sense that will become clear below. One reason is that the asymptotic behavior as $p^2 \rightarrow \infty$ is $\eta_*(p^2) \sim 1/p^2$ as found in Eq. (3.30). We will come back to the issue of choosing a parametrization later.

Computation of expansion coefficients. The remaining task is to determine the coefficient vectors $\mathbf{g} = (g_0, \dots, g_{n_{\max}^g})$ and $\boldsymbol{\eta} = (\eta_0, \dots, \eta_{n_{\max}^{\eta}})$ of the truncated series (3.47) such that Eqs. (3.45) and (3.26) are satisfied “as well as possible.” In technical terms, we need to minimize the *residual functions* corresponding to these equations,

$$\begin{aligned} \rho^g(\mathbf{g}, \boldsymbol{\eta}; \mathfrak{s}) &:= \left[d - 2 + 2\eta_*^{(4)}(p_i^2) \right] g_*(\mathfrak{s}) + 2\mathfrak{s}g'_*(\mathfrak{s}) \\ &\quad - \frac{2}{\tilde{N}} g_*(\mathfrak{s}) \int d(q, u, \Omega) {}_0^1 K(\mathfrak{s}, q, u; \eta_*) [\tilde{N} g_*(\mathfrak{s}) - g_*(q+p_3)^2] - g_*(q+p_4)^2 \end{aligned} \quad (3.48a)$$

$$\rho^{\eta}(\mathbf{g}, \boldsymbol{\eta}; p^2) := \eta_*(p^2) - \frac{1}{\tilde{N}} \int d(q, u) M(p^2, q, u; \eta_*) g_*\left(q^2 + p^2 + 2q\sqrt{p^2}u\right), \quad (3.48b)$$

where we substitute the ansatz (3.47) for g_* and η_* . Certainly, we cannot expect to obtain the exact solution with only a finite number of terms, but we can estimate the error from the decay of coefficients with increasing n [105] or by plugging the solutions back into the equations. This and the fact that we can at least in principle achieve better precision by including more terms gives us good control of the approximation error.

As minimization strategies, two approaches are commonly employed. The *Galerkin method* makes direct use of the orthogonality property of the Chebyshev rational functions (*cf.* Eq. (C.15) of Appendix C) and requires that the inner products between residuals and expansion functions vanish, *i.e.*

$$\int_0^\infty dx \sqrt{\frac{L}{x}} \frac{\rho(\mathbf{g}, \boldsymbol{\eta}; x) R_m(x)}{x + L} \stackrel{!}{=} 0, \quad m = 0, \dots, n_{\max}. \quad (3.49)$$

While some terms will simplify straightforwardly due to orthogonality, this procedure is computationally quite demanding because of the extra integration that has to be performed in addition to the integrals within the residual functions. Moreover, these integrals will become highly oscillatory with increasing m , posing further numerical challenges. The *pseudospectral* or *collocation method*, on the contrary, requires that the residual functions be satisfied on a discrete set of collocation grid points $\{x_0, \dots, x_{n_{\max}}\}$ only, *i.e.*

$$\rho(\mathbf{g}, \boldsymbol{\eta}; x_m) \stackrel{!}{=} 0, \quad m = 0, \dots, n_{\max}. \quad (3.50)$$

By an educated choice of these grid points, one can achieve that this method coincides with the spectral method if the integral in (3.49) is evaluated by an optimized quadrature rule [105]. One such optimal grid, which we will use throughout this work, consists of the roots of the Chebyshev rational function P_n of order $n_{\max} + 1$, visualized in Fig. 9b. For more details on this method as used here or pseudospectral methods in general, we refer to Appendix C and the literature [105, 114], respectively.

After choosing parametrizations and expansion orders in Eq. (3.47), we substitute the associated collocation grids $\{s_m\}$ and $\{p_m^2\}$ into the residual functions (3.48), defining a system of $n_{\max}^g + n_{\max}^\eta + 2$ algebraic equations

$$\rho_m^g(\mathbf{g}, \boldsymbol{\eta}) := \rho^g(\mathbf{g}, \boldsymbol{\eta}; s_m) = 0, \quad \rho_m^\eta(\mathbf{g}, \boldsymbol{\eta}) := \rho^\eta(\mathbf{g}, \boldsymbol{\eta}; p_m^2) = 0 \quad (3.51)$$

for the same number of unknowns g_n and η_n . To obtain a solution of these, we set up a Newton-Raphson iteration as detailed in Appendix D. To this end, we need to provide an initial guess for the coefficients g_n and η_n , which requires some intuition about the expected solution in order to achieve convergence of the algorithm.

For the actual computations, we implemented the described procedure in a C++ program. It turned out to be very useful to code the diagram functionals (3.21) in a functional form because this allows to adjust the program to other models by just a few minor modifications. The multidimensional numerical integrations were carried out using the Cuhre algorithm of the CUBA library by Thomas Hahn [115–118], which is a deterministic, high-precision integration scheme featuring globally adaptive subdivisions. As for the regularization scheme, we mostly used the exponential regulator (1.11) for our numerical studies; we will comment on the regulator dependence in more detail in Section 3.6. More information regarding the implementation of the Gross-Neveu model can also be found in Appendices B.5 and E.

Solutions. Having settled the computational approach, we are ready to discuss solutions of the fixed point problem. The principle observation is that we obtain exactly one additional bounded, nontrivial solution besides the Gaussian, which we will refer to henceforth as the Gross-Neveu fixed point. A first example is shown in Fig. 10, where both g_* and η_* were expanded to order $n_{\max}^g = n_{\max}^\eta = 47$. Here the number of flavors is $N_f = 2$, describing, for instance, the example of graphene [16, 34]. While the ansatz for g_* is in the sqrt parametrization with $P_n(\mathfrak{s}) = R_n(\sqrt{\mathfrak{s}})$, the ordinary id parametrization with $P_n(p^2) = R_n(p^2)$ is used for η_* . This will be our standard setup throughout the rest of this work; we will comment on the different parametrizations in the next paragraph.

It is reassuring to notice that there is only very little variation among the different momentum configurations. At the scale of the plot, the deviations are hardly visible and the lines corresponding to the different configurations of Fig. 7 coincide.[†] We conclude that the \mathfrak{s} -channel approximation parametrizes the momentum dependence quite satisfactorily. In particular, the fact that the reduction is not closed appears to be negligible.

Qualitatively, the finite- N_f solution for g_* looks very similar to the bosonized one (Fig. 6b) and the large- N_f one (Fig. 8). It acquires a finite maximum value at $\mathfrak{s} = 0$ and decays monotonically as \mathfrak{s} is increased. The same behavior is found for the anomalous dimension function. We point out again, however, that the asymptotic behavior $g_*(\mathfrak{s}) \sim 1/\sqrt{\mathfrak{s}}$ is different from what we observe in the bosonized formulation, where $\hat{g}(\mathfrak{s}) \sim 1/\mathfrak{s}$.

[†]Note that the two orthogonal configurations, Fig. 7b and c, are identical in the present truncation.

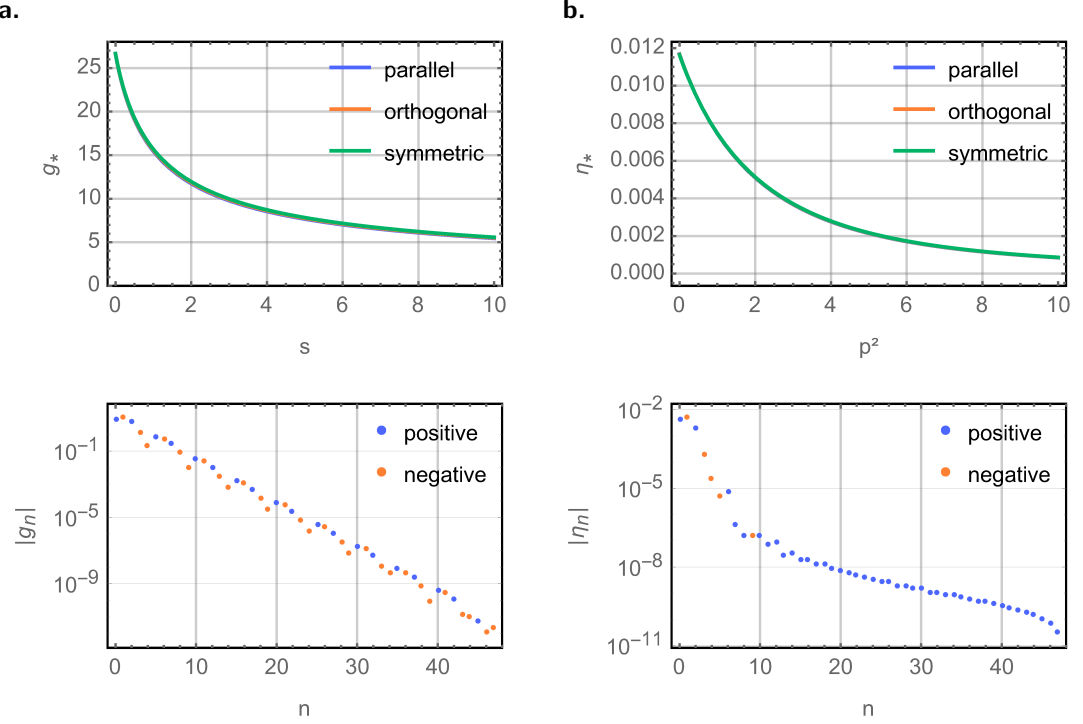


Figure 10: Fixed point solutions and corresponding Chebyshev coefficients for $\tilde{N} = 8$ ($N_f = 2$ in the reducible representation) with the coupling function g_* in (a) and the anomalous dimension function η_* in (b). The expansion order is $n_{\max} = 47$ for both. For g_* , the sqrt parametrization was used, whereas for η_* , the id parametrization was adopted. The top panels show the solutions functions for three different momentum configurations, even though the deviation is barely visible at the scale of the plot. The lower panels depict the absolute values of the associated Chebyshev coefficients (for the parallel configuration), blue dots corresponding to positive, red dots to negative ones.

Regarding the accuracy of the solutions, we first remark that the Chebyshev coefficients, plotted in the lower panels of Fig. 10, show geometric convergence for g_* as indicated by the roughly linear decay in the log-plot. Moreover we notice that the coefficients fall off more rapidly for g_* than for η_* , which is due to the fact that sqrt parametrization used for the former is better adapted to the asymptotic behavior and integral kernels than the id parametrization. Again, we will discuss these issues in detail in the next paragraph.

Seeing as we have geometric convergence for g_* , we can roughly estimate the approximation error as the magnitude of the last coefficient [105], giving an absolute error of about 10^{-11} . For η_* , the series appears to converge subgeometrically (or even algebraically only), so that we should multiply the last coefficient by the expansion order to get 10^{-10} as an estimate of the error's order of magnitude.

A more conservative way to assess the approximation error is to plug the obtained solutions back into the equations and evaluate the residuals (3.48). For our current example, these are plotted in Fig. 11. This estimates the absolute error of the coupling function to be about 10^{-10} . Also the relative error, *i.e.* the residual divided by the function value, is of the same order for moderate values of \mathfrak{s} . Its growth as $\mathfrak{s} \rightarrow \infty$ can be ascribed to the fact that $g_*(\mathfrak{s}) \rightarrow 0$ in this limit, so that the evaluation of the relative residuals becomes numerically unstable. For the anomalous dimension function, the absolute error is about 10^{-9} , and the relative error can become as big as 10^{-3} for large values of p^2 . Contrary to the case of g_* , the absolute error is not homogeneous across the domain, but grows as p^2 is increased. The reason for this and the generally worse convergence is that the id parametrization is not adapted to the asymptotics of η_* ; using a sqrt parametrization, we can improve it as we are going to show next. However, there are physical reasons to avoid parametrizing η_* as a function of $\sqrt{p^2}$ rather than p^2 , most importantly the analyticity of the propagator for small momenta.

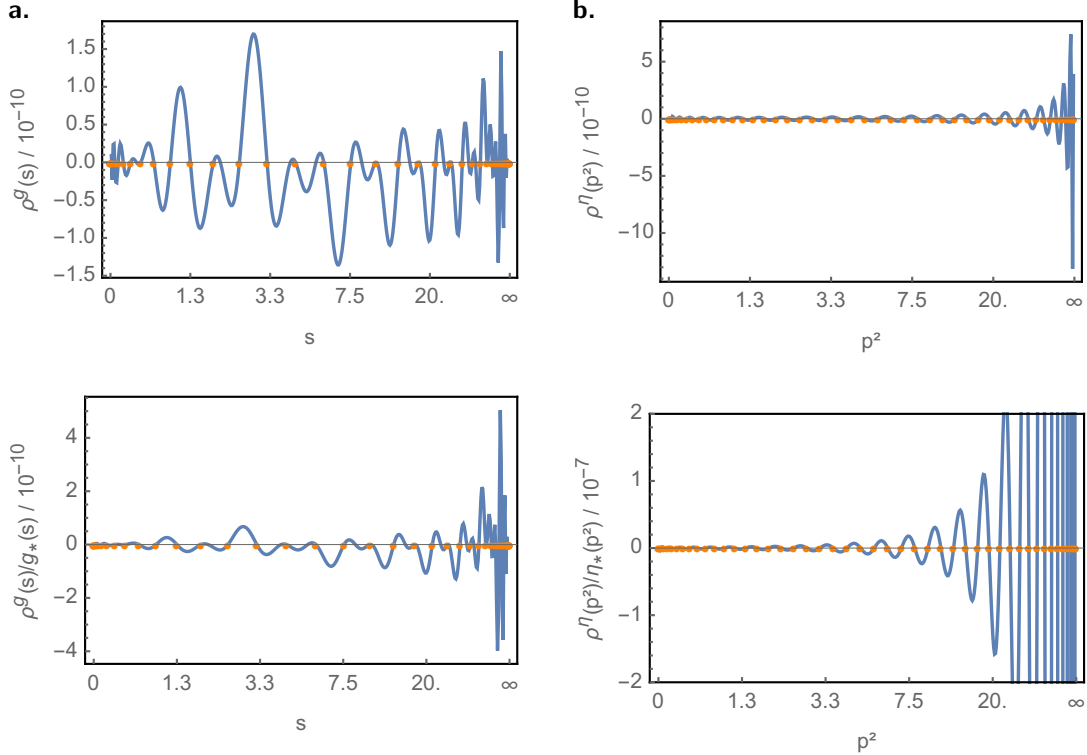


Figure 11: Absolute (top) and relative (bottom) residuals of (a) the coupling function and (b) the anomalous dimension function for $N_f = 2$. Expansions orders are $n_{\max} = 47$ for both, parametrizations are sqrt for g_* and id for η_* . The orange dots mark the collocation grid points. The s -axes in (a) have been compactified by a rational transformation $s_{\text{cmp}} = s/(s + L)$, and similarly for the p^2 -axes in (b).

Dependence on the parametrization. After all that excessive foreshadowing, let us finally investigate how different parametrizations for g_* and η_* affect convergence of the solutions. We select the parallel momentum configuration for this and begin with the anomalous dimension function, where we saw in the previous paragraph that convergence was much slower than for the coupling function. To understand that this is indeed caused by poor adaption of the parametrization to the asymptotic behavior, we also computed fixed-point solutions with both g_* and η_* in the sqrt parametrization, plotted in Fig. 12. Panel (a) shows both the id- and the sqrt-parametrized anomalous dimension function in one figure, where both functions overlap perfectly at the scale of the plot. Considering the coefficients of the sqrt-parametrized solution in (b), however, we see that convergence is improved dramatically compared to the id parametrization, and we obtain geometric convergence of the coefficients η_n now, too. This is also reflected in the absolute residuals in (c), which are reduced by more than three orders of magnitude.

A similar trend is observed for the coupling function g_* , but here the deviations are in fact much more severe in the id parametrization as can be seen in Fig. 13. In the plot of the coupling function in (a), we already encounter a visible deviation between the id and sqrt parametrizations. Looking at the coefficients in (b) then, we see that they fall off extremely slowly. Moreover, there is a distinct behavior for even and odd coefficients, where the even ones are predominantly positive and decay faster than odd ones, which in turn are all negative. This already hints at the fact that the id-parametrized guess does not pass for a solution of the fixed point equations. This is indeed confirmed by the absolute residual of about 0.04 in Panel (c). Although the collocation method ensures that the residuals vanish at the grid points, the interpolation is desperately poor between them.

To highlight the fact that this is caused by insufficient support of the asymptotic behavior, we re-expanded the sqrt-parametrized solution (Fig. 10a) in the id parametrization. Comparing the functions directly in Fig. 14a, they appear to match quite well. If we look at the coefficients of the re-expansion in Fig. 14b, however, we observe slow convergence, very similar to those of

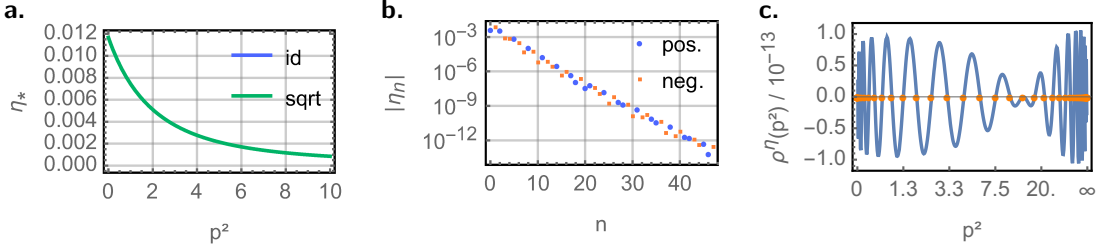


Figure 12: Solution for the anomalous dimension function in the sqrt parametrization for $N_f = 2$ and $n_{\eta}^{\eta} = 47$. In the simultaneous plot (a) of both the id- and the sqrt-parametrized solution, no difference is visible to the naked eye. The coefficients in (b), however, now show geometric convergence, too, and decay much more rapidly than in the id-parametrization. Similarly, the absolute residual in (c) decreases by more than three orders of magnitude and is now distributed homogeneously.

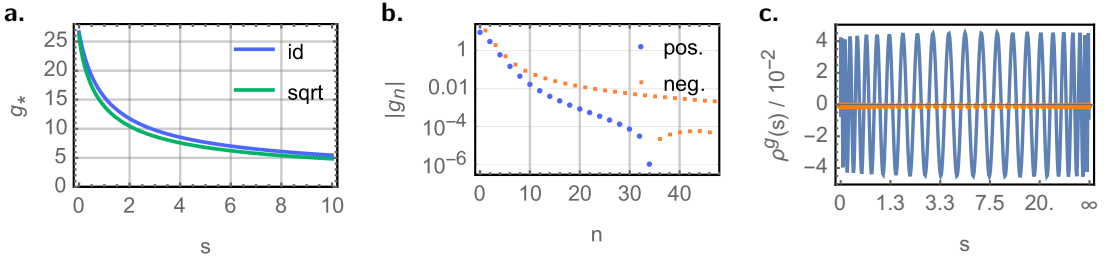


Figure 13: Attempted solution of the coupling function using the id parametrization for $N_f = 2$ and $n_g^g = 47$. The comparison to the sqrt-parametrized solution in (a) shows that the id-parametrized function deviates significantly. As for the coefficients (b), the decay is extremely slow, and appears to happen at different rates for even and odd coefficients. The absolute residual in (c) reveals that the id-parametrized function cannot be considered a solution of the fixed point equation.

the anomalous dimension function in the id parametrization (Fig. 10b). The absolute residual, Fig. 14c, starts off better for small \mathfrak{s} than in a direct id-parametrized calculation (Fig. 13), but eventually reaches the same, large order of magnitude as $\mathfrak{s} \rightarrow \infty$, which shows that it is indeed the large- \mathfrak{s} asymptotics where the id parametrization fails to work. The differences between the direct id-parametrized calculation (Fig. 13) and the re-expansion (Fig. 14) arise because the direct calculation tries to minimize the residuals uniformly across the domain, thereby failing to achieve better precision even for smaller values of \mathfrak{s} .

In hindsight, this justifies our “standard approach” using the sqrt parametrization for g_* and the id parametrization for η_* . From a physical point of view, the id parametrization is to be favored because we want solution functions that are analytic in the momenta of the interacting particles. Mathematically, though, the structure of the equations calls for a sqrt parametrization,

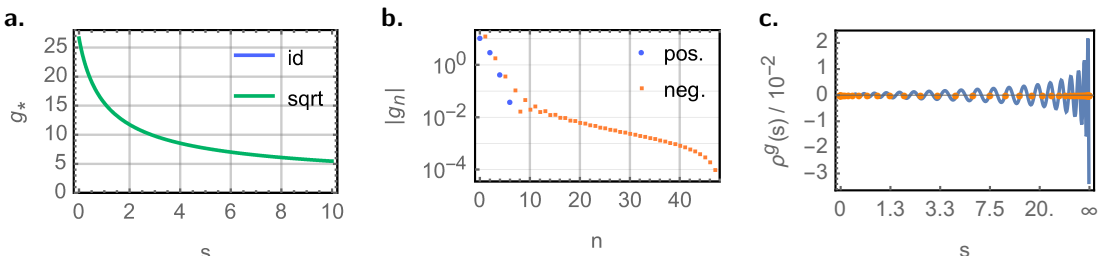


Figure 14: Re-expansion of the sqrt-parametrized solution for the coupling function in the id parametrization for $N_f = 2$ and $n_g^g = 47$. While there is no obvious difference in a direct comparison in (a), the coefficients in (b) decay slower and comparable to the id-parametrized anomalous dimension function. The absolute residual in (c) grows as $\mathfrak{s} \rightarrow \infty$, reinforcing the notion that the asymptotic behavior is insufficiently covered. The collocation points plotted belong to the sqrt parametrization of the basis solution.

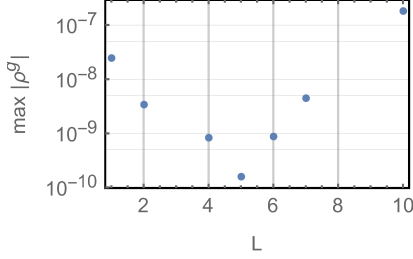


Figure 15: Maximum absolute residual of the coupling function g_* as a function of the compactification scale L for fixed expansion order $n_{\max}^g = 47$ and $N_f = 2$.

Table 1: Taylor expansions around $\mathfrak{s} = 0$ of numerically computed finite- N_f coupling functions.

N_f	$g_*(\mathfrak{s})$
1	$31.82 + 2.75 \times 10^{-6} \sqrt{\mathfrak{s}} - 38.59 \mathfrak{s} + 5.25 \mathfrak{s}^{3/2} + 54.43 \mathfrak{s}^2 + \dots$
2	$26.61 + 5.71 \times 10^{-7} \sqrt{\mathfrak{s}} - 25.14 \mathfrak{s} + 4.90 \mathfrak{s}^{3/2} + 25.99 \mathfrak{s}^2 + \dots$
4	$24.31 - 9.11 \times 10^{-9} \sqrt{\mathfrak{s}} - 20.97 \mathfrak{s} + 4.55 \mathfrak{s}^{3/2} + 19.09 \mathfrak{s}^2 + \dots$
12	$22.92 - 8.05 \times 10^{-7} \sqrt{\mathfrak{s}} - 18.79 \mathfrak{s} + 4.31 \mathfrak{s}^{3/2} + 15.87 \mathfrak{s}^2 + \dots$
24	$22.59 - 1.87 \times 10^{-6} \sqrt{\mathfrak{s}} - 18.30 \mathfrak{s} + 4.25 \mathfrak{s}^{3/2} + 15.19 \mathfrak{s}^2 + \dots$

and choosing the id parametrization instead leads to a loss of precision. While this loss is moderate and tolerable in the case of the anomalous dimension function, it leads to failure of convergence in the case of the coupling function, so that we are required to use the sqrt parametrization here in order to obtain fixed point solutions at all.

Another aspect of the parametrization dependence concerns choosing the compactification scale L (*cf.* Eq. (3.46)). This choice is not crucial, but for fixed expansion order, the accuracy of the solution may vary quite a bit depending on L . This is shown in Fig. 15, where we plot the maximum absolute residual $\sup_{\mathfrak{s} \in [0, \infty)} |\rho^g|$ for various values of L . Since we computed the suprema empirically, the data points in the figure will probably underestimate the true values, but the general trend should be unaffected. The plot suggests that the optimum choice of L lies around $L = 5$. Of course, this may change for other models with different couplings, flavors, fixed points, *etc.*, but in fact we do not expect strong deviations because the structure of equations and integrals remains the same. In the remainder of this work, we will therefore use $L = 5$ for our expansion functions. Incidentally, this was also the value used for all solutions shown above.

Dependence on the flavor number. All solutions presented so far were obtained for $N_f = 2$ flavors in the reducible representation (*i.e.* $\tilde{N} = 8$). In Fig. 16 we now compare the nontrivial fixed point solutions for various flavor numbers. The coupling functions in Panel (a) do not show much variation, but generally the coupling value tends to increase for smaller values of N_f . The plot also suggests convergence to some nontrivial function in the large- N_f limit as was found in Section 3.4. However, we point out that it is meaningless to compare the large- N_f solution in Fig. 8 to the ones presented here on a quantitative level, because the two were obtained for different regularization schemes.

Nevertheless, we would like to comment on the maximum regularity of the finite- N_f solutions. Remember that the large- N_f limit in principle allowed a family of solutions parametrized by the constant g_∞ in Eq. (3.38). We fixed this constant by requiring that the order $\sqrt{\mathfrak{s}}$ coefficient of a Taylor expansion around $\mathfrak{s} = 0$ should vanish, so that the solution becomes maximally regular. If we similarly expand the finite- N_f solutions as shown in Tab. 1, we observe that they indeed attain this property automatically as argued in the previous section.

For the anomalous dimension functions in Fig. 16b, there is a broader variation with the flavor number and the values again increase for smaller N_f . Here as well, convergence to the large- N_f limit, where $\eta_*(p^2) = 0$, is visible.

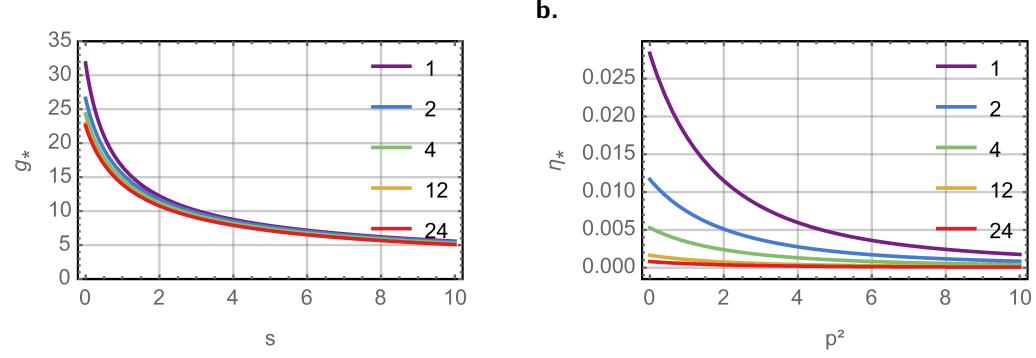


Figure 16: Fixed point solutions for various flavor numbers N_f in the reducible representation ($d_\gamma = 4$); (a) coupling functions, (b) anomalous dimension functions. All solutions were obtained for parallel momentum configuration and have expansion orders $n_{\max}^g = n_{\max}^\eta = 47$.

Another source of variation is the regularization scheme. As far as the fixed point solutions are concerned, however, quantitative deviations between different choices of regulators are expected because the precise position of the fixed points is nonuniversal. The existence of fixed point solutions as well as their qualitative behavior should of course still be independent of the regularization, and this is indeed the case as was tested for the regulators (1.10) through (1.12). A more careful analysis of the regulator dependence will be part of the next section because the critical exponents computed there are universal quantities and should thus not vary much for different regulators.

3.6 Spectrum of the nontrivial fixed point

In the spirit of the general discussion in Section 1.3, we would like to characterize the fixed points of the Gross-Neveu model by determining their eigendirections in theory space and the associated critical exponents. To this end, we perturb around the fixed point, $g(\mathfrak{s}) = g_*(\mathfrak{s}) + e^{-\theta t} \varepsilon(\mathfrak{s})$, and expand the flow equation (3.4) to first order in ε . The resulting linearized flow equation is

$$-\theta \varepsilon = \left[d - 2 + 2\eta^{(4)} + 2\mathfrak{s} \partial_{\mathfrak{s}} \right] \varepsilon - \frac{\tilde{N}}{0} B_{\leftrightarrow}^{\mathfrak{s}2}[g_*, \varepsilon] + \frac{2}{0} B_{\leftrightarrow}^{\mathfrak{s}1}[g_*, \varepsilon], \quad (3.52)$$

where $\frac{a_1}{a_2} B_{\leftrightarrow}^{\mathfrak{m}}[g_1, g_2] := \frac{a_1}{a_2} B^{\mathfrak{m}}[g_1, g_2] + \frac{a_1}{a_2} B^{\mathfrak{m}}[g_2, g_1]$ denotes symmetrized diagram functionals. Expanding the latter, we find the more explicit form

$$\begin{aligned} -\theta \varepsilon(\mathfrak{s}) = & \left[d - 2 + 2\eta_*^{(4)}(p_i^2) \right] \varepsilon(\mathfrak{s}) + 2\mathfrak{s} \varepsilon'(\mathfrak{s}) - 4 g_*(\mathfrak{s}) \varepsilon(\mathfrak{s}) \int d(q, u, \Omega) \frac{1}{0} K(\mathfrak{s}, q, u; \eta) \\ & + \frac{2}{\tilde{N}} \varepsilon(\mathfrak{s}) \int d(q, u, \Omega) \frac{1}{0} K(\mathfrak{s}, q, u; \eta) [g_*([q+p_3]^2) + g_*([q+p_4]^2)] \\ & + \frac{2}{\tilde{N}} g_*(\mathfrak{s}) \int d(q, u, \Omega) \frac{1}{0} K(\mathfrak{s}, q, u; \eta) [\varepsilon([q+p_3]^2) + \varepsilon([q+p_4]^2)]. \end{aligned} \quad (3.53)$$

To solve this eigenvalue problem and determine the eigenvalues θ and perturbations ε , we will use expansions in terms of Chebyshev rational functions again.

Asymptotic scaling relation. Before doing so, however, we will investigate the asymptotics of the linearized flow equation (3.53). As before, the quantum terms are suppressed as $\mathfrak{s} \rightarrow \infty$ because $\frac{1}{0} K_1^{(F)} \sim 1/\sqrt{\mathfrak{s}}$ and also $g_*(\mathfrak{s}) \sim \mathfrak{s}^{\frac{2-d}{2}}$. Solving the remaining asymptotic equation, we thus find that $\varepsilon(\mathfrak{s}) \sim \mathfrak{s}^a$, where the exponent a is related to the critical exponent θ via the asymptotic scaling relation

$$\text{Re } \theta + 2a = 2 - d. \quad (3.54)$$

Consequently, the asymptotic power a and the critical exponent θ balance each other: The more irrelevant the perturbation ε , the faster it grows as $\mathfrak{s} \rightarrow \infty$. Hence, in order to probe the irrelevant

part of the spectrum beyond $\text{Re } \theta = 2 - d$, we have to allow for asymptotically growing eigenperturbations. Since the Chebyshev rational functions are bounded, we multiply by a polynomial in \mathfrak{s} , leading to the ansatz

$$\varepsilon(\mathfrak{s}) = (\mathfrak{s} + L)^{a_{\max}} \sum_{n=0}^{n_{\max}^{\varepsilon}} \varepsilon_n P_n(\mathfrak{s}). \quad (3.55)$$

Regarding the value of a_{\max} , we follow two different approaches. For the first one, we set a_{\max} to a constant numerical value, thus keeping a *fixed maximum growth*. In contrast, the second approach uses a *running asymptotics* scheme where $a_{\max} = \frac{2-d-\text{Re } \theta}{2}$ is chosen according to the scaling relation (3.54).

En passant, we remark that this scaling relation determines the exact perturbations around the Gaussian fixed point $g_* = 0$ because in this case the fluctuation terms in the linearized flow equation vanish identically for all \mathfrak{s} . Therefore, the perturbations are $\varepsilon(\mathfrak{s}) = C \mathfrak{s}^{\frac{2-d-\theta}{2}}$ with normalization constant C . Requiring that they be well-defined in $\mathfrak{s} = 0$ then implies that all perturbations around the Gaussian fixed point are irrelevant with $\text{Re } \theta \leq 2 - d$.

Fixed maximum asymptotic growth. To investigate the critical behavior of the nontrivial fixed point in the fixed maximum growth scheme, we substitute the ansatz (3.55) into the linearized flow equation (3.52). Choosing a collocation grid $\{\mathfrak{s}_m\}$ like we did for the fixed point solutions, we obtain an algebraic eigenvalue equation

$$-\theta \mathbf{P} \boldsymbol{\varepsilon} = \mathbf{J}^{gg} \boldsymbol{\varepsilon}, \quad (3.56)$$

where $\boldsymbol{\varepsilon} = (\varepsilon_n)$ is the Chebyshev coefficient vector, $\mathbf{P} = (P_{mn})$ with

$$P_{mn} = (\mathfrak{s}_m + L)^{a_{\max}} P_n(\mathfrak{s}_m), \quad (3.57)$$

and $\mathbf{J}^{gg} = (J_{mn}^{gg})$ is the Jacobian of the residual function ρ^g (3.48a) that is also needed in the Newton-Raphson procedure for computing fixed point solutions (*cf.* Appendix B.5),

$$\begin{aligned} J_{mn}^{gg} &= \int_0^\infty d\mathfrak{s}' \left. \frac{\delta \rho^g[g, \eta](\mathfrak{s}_m)}{\delta g(\mathfrak{s}')} \right|_{\substack{g=g_* \\ \eta=\eta_*}} (\mathfrak{s}' + L)^{a_{\max}} P_n(\mathfrak{s}') \\ &= \left\{ \left[1 + 2 \eta^{(4)}(p_i^2) \Big|_{\mathfrak{s}_m} + \frac{2a_{\max}\mathfrak{s}_m}{\mathfrak{s}_m + L} \right] P_n(\mathfrak{s}_m) + 2\mathfrak{s} P'_n(\mathfrak{s}_m) \right\} (\mathfrak{s}_m + L)^{a_{\max}} \\ &\quad - \tilde{B}_{\leftrightarrow}^{\mathfrak{s}2} [g_*, (\cdot + L)^{a_{\max}} P_n(\cdot)](\mathfrak{s}_m) + \tilde{B}_{\leftrightarrow}^{\mathfrak{s}1} [g_*, (\cdot + L)^{a_{\max}} P_n(\cdot)](\mathfrak{s}_m). \end{aligned} \quad (3.58)$$

The ‘ \cdot ’ in the last line stands for the argument of the function entering the diagram functional. This way we reduced the task to the algebraic eigenvalue problem (3.56): In the current approximation, the critical exponents are just the eigenvalues of the matrix $(-\mathbf{P}^{-1} \mathbf{J}^{gg})$, which we determined numerically using the *GNU Scientific Library* [119] and/or the *Eigen3 Library* [120].

We restrict to $d = 3$ and begin with the case $N_f = 2$ again, for which the resulting spectra for different values of a_{\max} are plotted in Fig. 17. Note that we only show the real part of the eigenvalues, which is the decisive information to classify a perturbation as relevant or irrelevant, and distinguish purely real from complex eigenvalues by color. Here we used the id parametrization for the perturbations.

Our first observation is a numerical confirmation of the asymptotic scaling relation (3.54): The real parts of the spectrum are indeed bounded by $\text{Re } \theta \geq -1 - 2a_{\max}$. They appear to be bounded from above as well, with the most relevant eigenvalue being approximately 1. All eigenvalues with real parts exceeding the lower bound set by the asymptotics are crammed into the interval marked out by the most relevant perturbation and the asymptotic bound.

Sorted by relevance, the first four eigenvalues are found to be real. Only one of them is positive, meaning that the fixed point has one relevant direction, in accordance with the large- N_f and partially bosonized results [30, 60, 61]. As with the fixed point solution, the variation of these first critical exponents for different momentum configurations is small as we observe from the fact that the three dots for each value of a_{\max} in Fig. 17 are well aligned. Nevertheless, the fluctuations

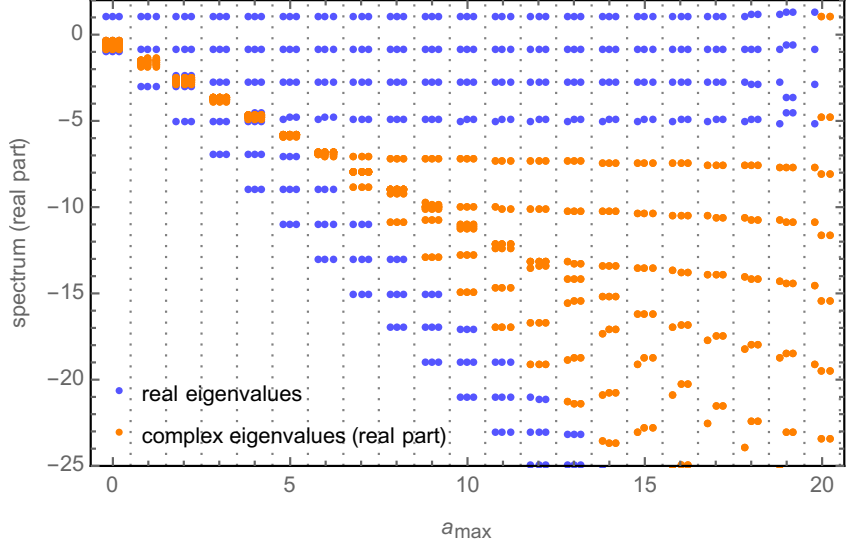


Figure 17: Spectrum of the Gross-Neveu fixed point for $N_f = 2$ as obtained for various values of constant a_{\max} . Blue dots mark real eigenvalues, orange dots mark the real part of eigenvalues with nonvanishing imaginary part. For each value of a_{\max} , there are three dots corresponding to the parallel, orthogonal, and symmetric momentum configurations (from left to right). The perturbations are id-parametrized and have expansion order $n_{\max}^{\varepsilon} = 20$.

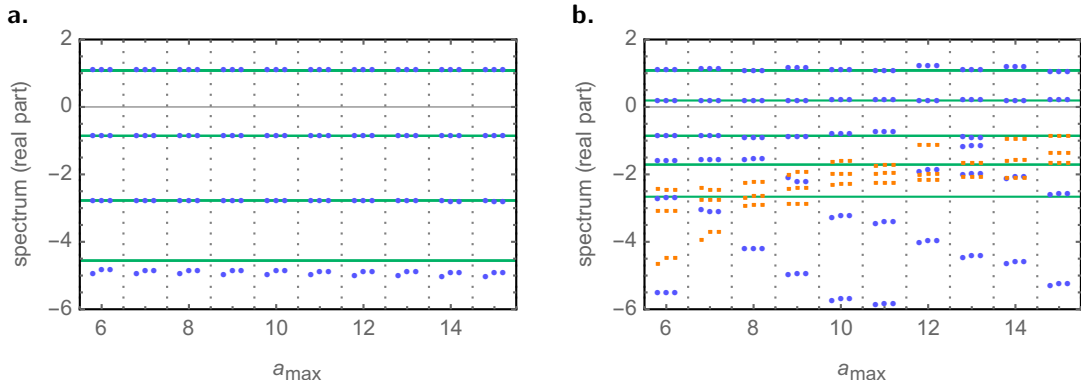


Figure 18: First four relevant critical exponents for different values of constant a_{\max} (data points) and running asymptotics (parallel momenta, green lines) for (a) id and (b) sqrt parametrization of the perturbation. Parameters: $N_f = 2$, $n_{\max}^{\varepsilon} = 20$ in (a), $n_{\max}^{\varepsilon} = 34$ in (b).

increase towards the irrelevant part of the spectrum as well as for larger values of a_{\max} . Decreasing accuracy for more irrelevant exponents is expected because the effective action (3.3) is very restrictive in terms of considered operators. The deviations for $a_{\max} \gtrsim 18$ are likewise reasonable: Consider, for instance, the case with $a_{\max} = 18$ and $\theta \approx 1$. On the one hand, the prefactor in the ansatz (3.55) grows as \mathfrak{s}^{18} for large \mathfrak{s} . On the other hand, we know from the asymptotic scaling relation (3.54) that a perturbation with $\theta \approx 1$ should decay as \mathfrak{s}^{-1} . Consequently, the Chebyshev series in (3.55) needs to fall off as \mathfrak{s}^{-19} . Since the maximum order considered here was $n_{\max}^{\varepsilon} = 20$, it can maximally decay as \mathfrak{s}^{-20} . Therefore, there really remains only one order to fine-tune the perturbation. To conclude, the fixed maximum growth scheme demands for a careful balance of the asymptotic power a_{\max} and the expansion order n_{\max}^{ε} of the perturbations in order to capture the interesting part of the spectrum reliably.

A more precise view on the first four critical exponents is given by the close-up of the region between $a_{\max} = 6$ and 15 in Fig. 18a. There again, no variation between the momentum configurations is visible for the first three eigenvalues, whose numerical values are listed in Tab. 2 below, while the fourth one shows small differences. The green lines correspond to the eigenvalues found in the running asymptotic power a_{\max} and the expansion order n_{\max}^{ε} of the perturbations in order to capture the interesting part of the spectrum reliably.

Running asymptotics. Instead of prescribing a fixed value for the power a_{\max} of the prefactor in the ansatz (3.55), we can adjust it better to the perturbation associated with some eigenvalue θ by using our knowledge about the asymptotic behavior (3.54) and setting $a_{\max} = -\frac{1+\theta}{2}$. Note that we focus on real eigenvalues in this paragraph.

Since the eigenvalue θ now also appears in the exponent on the right-hand side of Eq. (3.53), we cannot reduce it to an algebraic eigenvalue problem. Instead we use a Newton-Raphson iteration again to numerically solve for the Chebyshev coefficients ε and the eigenvalue θ simultaneously, which amount to a total of $n_{\max}^\varepsilon + 2$ variables. As usual we obtain $n_{\max}^\varepsilon + 1$ equations by requiring (3.53) to hold on the collocation grid $\{\mathfrak{s}_m\}$. In addition, we have to normalize the perturbations in some way since any multiple of a solution $\varepsilon(\mathfrak{s})$ still solves the equation. The condition we chose here, provided that $\varepsilon(0) \neq 0$, is enforced on the Chebyshev part of the ansatz (3.55),

$$\sum_{n=0}^{n_{\max}^\varepsilon} \varepsilon_n P_n(0) = \sum_{n=0}^{n_{\max}^\varepsilon} (-1)^n \varepsilon_n \stackrel{!}{=} 1. \quad (3.59)$$

This provides the necessary extra equation to match the number of variables. In practice it turned out advantageous to begin with a few iterations for *fixed* θ in order to lock the solver in the vicinity of that value. Only then would we release θ and solve the full system. Otherwise the impact of the single variable θ compared to the $n_{\max}^\varepsilon + 1$ variables ε_n was too small and the solver jumped wildly between different eigenvalues.

We already pointed to the resulting eigenvalues marked by the green lines in Fig. 18a. As can be seen, the first three are in excellent agreement with the exponents found for constant asymptotics, whereas the fourth one is estimated slightly larger from running asymptotics. These four were all eigenvalues found for initial values for θ between 10 and -12 . Comparing to the constant asymptotics calculation, this is explained by the onset of complex eigenvalues after the fourth exponent (*cf.* Fig. 17). Since we only probe for real eigenvalues in the running asymptotics scheme, these are not visible to the solver.

Dependence on the parametrization. So far we have only used the id parametrization of the Chebyshev series for the eigenperturbations $\varepsilon(\mathfrak{s})$. Remembering the implications of the previous section, where we were in fact forced to use the sqrt parametrization for the fixed point coupling function in order to find a solution at all, the question of what the situation is like for the eigenperturbations arises naturally.

To convince ourselves that the id parametrization produces solutions of the linearized flow equation (3.53), we compute the relative residual of the eigenperturbations with running asymptotics, displayed graphically in Fig. 19. For small values of \mathfrak{s} , the relative error is of order 10^{-4} , which is reasonable given the comparatively small expansion order. Moreover, it decreases significantly with increasing \mathfrak{s} , reflecting the fact that the asymptotic behavior is perfectly tailored to the respective eigenvalue. We remark that we also computed perturbations of higher expansion order, which further decreased the error. However, this did not change the value of the corresponding eigenvalues significantly; in particular, the variations were smaller than those from choosing other regularization schemes, as we will explore in the next paragraph.

Despite the reassuring error estimates, it is still informative to look at sqrt-parametrized eigenperturbations. The leading part of the resulting spectrum is shown in Fig. 18b. To compensate for the slower suppression of the asymptotic prefactor in (3.55), we used higher order expansions with $n_{\max}^\varepsilon = 34$ in the constant asymptotics scheme. The resulting picture is much less clear than in the id-parametrized case. The leading eigenvalue is still the same, but we obtain another relevant perturbation with $\theta \approx 0.2$. Furthermore, there are no consistent irrelevant exponents across several values of a_{\max} in the constant asymptotics scheme. Instead, the influence of complex eigenvalues begins for larger values and seemingly interferes with the irrelevant part as found in the id parametrization.

Using running asymptotics elucidates the situation to some extent: In addition to the eigenvalues detected in the id parametrization, the sqrt parametrization yields new perturbations with eigenvalues roughly half way between the ones found previously. This is in accordance with the spectra obtained in the large- N_f limit and around the Gaussian fixed point. There we could likewise

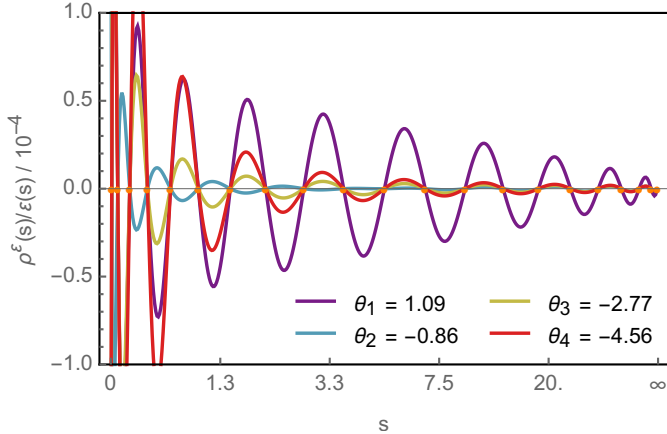


Figure 19: Relative residuals of the eigenperturbations obtained in the running asymptotics scheme using the id parametrization. Parameters: $N_f = 2$, $n_{\max}^\varepsilon = 20$.

Table 2: Critical exponents for different regulators and flavor numbers. The label ‘sqrt exp.’ refers to the exponential regulator (1.11), while different α values label regulators of the type (1.12). The eigenperturbations were obtained in the id parametrization with expansion order $n_{\max}^\varepsilon = 20$.

regulator	$N_f = 1$				$N_f = 2$				$N_f = 4$			
	θ_1	θ_2	θ_3	η_ψ	θ_1	θ_2	θ_3	η_ψ	θ_1	θ_2	θ_3	η_ψ
sqrt exp.	1.23	-0.73	-2.51	0.028	1.09	-0.86	-2.79	0.012	1.04	-0.93	-2.91	0.005
$\alpha = 2.0$	1.26	-0.70	-2.55	0.034	1.10	-0.83	-2.79	0.014	1.04	-0.92	-2.92	0.006
$\alpha = 2.5$	1.26	-0.70	-2.56	0.035	1.10	-0.83	-2.80	0.014	1.04	-0.92	-2.92	0.006

observe that allowing half-integer powers of \mathfrak{s} in the perturbations resulted in extra eigenvalues lying in between. All these observations substantiate the claim that the spectra are preferably computed using id-parametrized Chebyshev series for the perturbations. Allowing instead for non-analytic eigenperturbations leads to spurious additional solutions that are prone to lack uniform convergence [104].

Dependence on the regulator. In principle and contrary to the fixed point locations, the critical exponents are universal quantities and should thus be independent of the regularization scheme [69, 70]. On a general basis, though, this only holds if the effective action includes all interactions compatible with the symmetry group of the considered model. Since practical calculations usually demand for truncations of the theory space, a spurious regulator dependence is introduced. As a rough estimate of the truncation error, we can therefore compute universal quantities using different regulators and analyze the deviations. Nevertheless, this always sets a lower bound for the truncation error only; the actual deviation may be arbitrarily larger if the truncation misses essential operators in the effective action.

In Tab. 2 we collect the critical exponents obtained for different regulators and flavor numbers. Besides the first three scaling exponents θ_1 , θ_2 , and θ_3 , we also compare the anomalous dimension $\eta_\psi = \eta_*(0)$. The first line, labeled ‘sqrt exp.’, corresponds to the regulator (1.11), whereas the other two lines belong to regulators of the form (1.12), labeled by their values for the parameter α . We point out that all these regulators suppress low-energy modes exponentially. Using other, non-analytic shape functions, especially the linear type (1.10), turned out to be unfeasible numerically because of resulting nonsmooth loop integrands, so that we were unable to achieve satisfactory precision of the solutions.

The qualitative picture remains the same for other flavor numbers (also beyond $N_f = 4$) and regulators, meaning that there is always one relevant perturbation and a spacing of approximately 2 between the leading eigenvalues in the id parametrization.

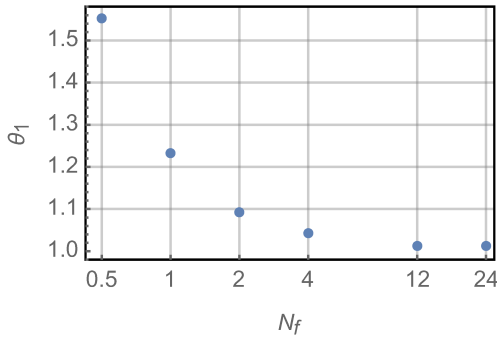
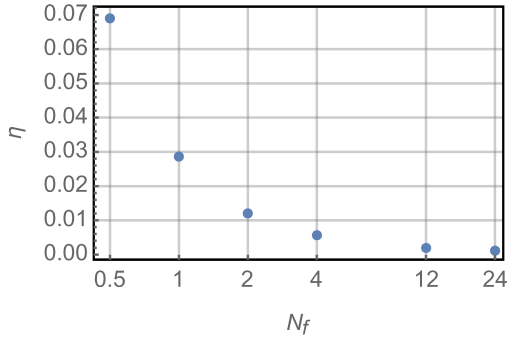
a.**b.**

Figure 20: Comparison of (a) leading exponents and (b) anomalous dimensions for different flavor numbers.

The observed variation among the different regulators is largest for the anomalous dimension. Moreover, we note that the differences seemingly decrease as N_f is increased, which is understood because the fluctuations become more homogeneous for larger N_f , approaching the limit $N_f \rightarrow \infty$ where only the $\mathfrak{s}2$ -diagram contributes. Since the latter does not involve an integration of the coupling function in the \mathfrak{s} -channel approximation, the regulator dependence is expected to reduce. Quite generally, the differences are greater between the two types of shape functions than between the different choices of α for the second type (1.12).

Comparison to previous results. We briefly come back to the behavior of leading exponents and anomalous dimensions for different flavor numbers, plotted in Fig. 20. Empirically, we observe a monotonic decay of both quantities to their large- N_f values as the flavor number grows. For the leading exponent, this means that it approaches the value 1 from above. Unfortunately, this does not comply with predictions of $1/N_f$ -expansions [39, 57], where it was found that

$$\theta_1 \simeq 1 - \frac{0.270}{N_f} + \frac{1.366}{N_f^2} + \dots, \quad (3.60)$$

stating that θ_1 should approach 1 from below as $N_f \rightarrow \infty$. Critical exponents for the Gross-Neveu model have also been computed using numerous other approaches, *e.g.* bosonized FRG [26, 27, 30, 60, 61], perturbation theory [37–40, 43, 44], conformal bootstrap (CBS) [56, 57, 59], and Monte Carlo (MC) simulations [47, 48, 51–55]. We compare a selection of these findings in Tab. 3. As values for this work, we take the exponents obtained from the regulator (1.11) (first line in Tab. 2) because this regulator generally showed the smallest residuals for fixed expansion order of the Chebyshev series, and estimate the error from the variation for other choices of regularization.

Especially for these small flavor numbers, the differences between the results from the various methods are quite large and the overall picture is rather inconclusive. Nevertheless, and even though the convergence to the large- N_f limit occurs from the wrong direction, our results generally fit within the variational bounds set by the other approaches. Compared with the bosonized FRG results, whose methodology is closest to ours, we observe quantitative deviations of 10...15% for θ_1 and of about 50% for η_ψ . A weakness of our approach is that we do not explicitly model the dynamics of the order parameter $\langle \bar{\psi} \psi \rangle$ of the phase transition described by the Gross-Neveu fixed point. Since the contributions of these order parameter fluctuations are assumed to be dominant particularly for the leading exponent θ_1 , we cannot actually expect to find high-precision estimates of the critical quantities. This may also explain the asymptotic convergence of θ_1 to its limiting value from above as $N_f \rightarrow \infty$.

* * *

Studying the pure Gross-Neveu model with momentum-dependent interactions qualitatively confirmed many previously obtained results. In particular, we verified the existence of a nontrivial, critical fixed point with a relevant exponent of order 1. On a general level, we worked out that the

Table 3: Critical exponents of the $N_f = 1$ and $N_f = 2$ Gross-Neveu models as found by various methods. Abbreviations: CBS (conformal bootstrap), exp. (expansion), FRG/bos. (functional renormalization group, bosonization), MC (Monte Carlo).

$N_f = 1$		$N_f = 2$			
method	θ_1	η_ψ	method		
			θ_1		
FRG (<i>here</i>)	1.23(3)	0.028(7)	FRG (<i>here</i>)	1.09(1)	0.012(2)
FRG/bos. [61]	1.075(4)	0.0645	FRG/bos. [30]	0.9821	0.0320
$1/N_f$ [19, 39, 40]	1.361	0.105	FRG/bos. [61]	0.994(2)	0.0276
$4-\varepsilon$ exp. [38]	1.160	0.110	$1/N_f$ [19, 39, 40]	0.962	0.044
MC [52]	1.25(3)	–	$2+\varepsilon$ exp. [43]	0.931	0.082
MC [53]	1.30(5)	–	$4-\varepsilon$ exp. [38]	1.055	0.0065
CBS [59]	0.76	0.084	MC [48]	1.00(4)	–
			MC [51]	1.22(3)	0.37(1)
			CBS [59]	0.88	0.044

flow of the Gross-Neveu coupling is dominated by interactions in the Mandelstam \mathfrak{s} -channel, which formed the basis of our subsequent analysis implementing reduced momentum dependence. In this approximation, we derived an exact solution for the large- N_f limit and computed fixed points and critical exponents using pseudospectral expansions in terms of Chebyshev rational functions for finite N_f . Although the reduction to a pure \mathfrak{s} -channel dependence is to some extent ambiguous, the resulting fixed point solutions and critical exponents turned out to be very stable upon variations of the external momentum configuration, indicating that the \mathfrak{s} -channel parametrizes the important features of the interaction. Furthermore, our investigations revealed a certain non-analyticity of the coupling functions in the variable \mathfrak{s} , which is presumably of mathematical nature or caused by the incomplete momentum dependence and the nonlocality of the interaction.

We will now set about enlarging the theory space and consider the flow of all non-derivative four-fermion vertices consistent with the symmetries of the Thirring model. Thereby we will encounter the Gross-Neveu fixed point again and will also shed some more light on the questions of closedness of the truncation for the effective action studied in the current section.

4 Thirring model

The Gross-Neveu model discussed in the previous section features one type of four-fermion interactions, namely a scalar, flavor-singlet vertex. We will now turn to the different but related Thirring model [36], whose defining microscopic action involves a vector-type interaction and reads

$$S[\psi, \bar{\psi}] = \int d^d x \left[\bar{\psi}(x) i \not{d} \psi(x) + \frac{\bar{g}_{\text{Th}}}{2N_f d_\gamma} (\bar{\psi}(x) \gamma_\mu \psi(x))^2 \right]. \quad (4.1)$$

As described in Section 2.1, the Thirring model in the reducible representation of the Clifford algebra shares all the symmetries of the reducible Gross-Neveu model, but actually has a larger $U(2N_f)$ symmetry. It was originally introduced as an example for an exactly solvable quantum field theory in $d = 2$ spacetime dimensions [36]. In the following, we will instead work with its three-dimensional variant, *i.e.* $d = 3$.

Due to its close relation [16, 42, 45, 121, 122] to quantum electrodynamics in three dimensions (QED₃) [123], the Thirring model describes aspects of (2+1)-dimensional condensed matter systems like, once again, graphene [17, 124] or high- T_c superconducting cuprates [22, 23]. Moreover, it is interesting on its own because of open questions regarding, *e.g.*, the critical flavor number for spontaneous chiral symmetry breaking mentioned in the Introduction. While the formation of a chiral condensate is prohibited for infinite N_f [24, 42], various studies using different methods report different values for the critical flavor number $N_{f,\text{crit}}$ below which the symmetry is dynamically broken: Dyson-Schwinger equations for the fermion propagator [24, 45], $1/N_f$ expansions [121], FRG calculations [31, 32], and lattice Monte Carlo simulations [25, 29] have yielded values between $N_{f,\text{crit}} = 2 \dots 7$. Other Dyson-Schwinger studies [41] find chiral symmetry breaking for all finite N_f , whereas recent lattice calculations [33, 54] suggest that there is no symmetry breaking for any integer flavor number in the reducible representation at all. While we will not be able to definitely settle this question, we will reinforce the observation of an increasing influence of the Nambu-Jona-Lasinio (NJL) interaction compared to the Thirring interaction for small N_f , providing one possible explanation for the occurrence of a critical N_f [31, 32].

4.1 Flow of the coupling functions

Weyl decomposition and effective action. We already observed in Section 2.1 that there is one additional, non-derivative four-fermion vertex sharing the symmetries of the Thirring model, namely the pseudoscalar $(\bar{\psi} \gamma_{45} \psi)^2$. To obtain a more complete picture and seeing as this pseudoscalar vertex influences the Thirring vertex significantly, we will add that interaction to our effective action below.

In addition we found that the N_f -flavor Thirring model has an overall $U(2N_f)$ flavor and chiral symmetry. From a computational point of view it is therefore beneficial to decompose the N_f four-component Dirac spinors $\psi, \bar{\psi}$ in the reducible representation into $2N_f$ two-component Weyl spinors $\chi, \bar{\chi}$ transforming according to the irreducible representation [32, 94]. This is achieved by means of the chiral projectors $P_\pm = \frac{1}{2}(\mathbf{1} \pm \gamma_{45})$ and is particularly convenient in a representation where γ_{45} is diagonal. After the decomposition, the vertices become [32, 94]

$$\bar{\psi} \gamma_{45} \psi \equiv \bar{\chi} \chi \quad \text{and} \quad \bar{\psi} \gamma_\mu \psi \equiv \bar{\chi} \sigma_\mu \chi \quad (4.2)$$

with σ_μ denoting the Pauli matrices,

$$\sigma_1 = \begin{pmatrix} 0 & 1 \\ 1 & 0 \end{pmatrix}, \quad \sigma_2 = \begin{pmatrix} 0 & -i \\ i & 0 \end{pmatrix}, \quad \sigma_3 = \begin{pmatrix} 1 & 0 \\ 0 & -1 \end{pmatrix}. \quad (4.3)$$

The pseudoscalar vertex has thus been transformed into a scalar Gross-Neveu vertex. Hence the irreducible Gross-Neveu-Thirring model defines the same symmetry class as the reducible Thirring model. A basis of the Dirac/Weyl space in the irreducible representation is then given by $\{\mathbf{1}, \sigma_1, \sigma_2, \sigma_3\}$. Our ansatz for the effective average action is obtained by combining these two

interactions and parametrizing each of them by a momentum-dependent coupling function. We thus let

$$\begin{aligned}\Gamma_k[\chi, \bar{\chi}] = & - \int_p Z(p^2) \bar{\chi}(p) \not{p} \chi(p) + \int_{p_2, p_3, p_4} \frac{\bar{g}_{\text{GN}}(p_1, p_2, p_3, p_4)}{2\tilde{N}} \bar{\chi}(-p_1) \chi(p_2) \bar{\chi}(-p_3) \chi(p_4) \\ & + \int_{p_2, p_3, p_4} \frac{\bar{g}_{\text{Th}}(p_1, p_2, p_3, p_4)}{2\tilde{N}} \bar{\chi}(-p_1) \sigma_\mu \chi(p_2) \bar{\chi}(-p_3) \sigma_\mu \chi(p_4).\end{aligned}\quad (4.4)$$

As before, we do not denote the k -dependence of the wave function renormalization Z and the coupling functions \bar{g}_{GN} and \bar{g}_{Th} explicitly. Similar to the Gross-Neveu case, the Thirring coupling must also satisfy the symmetry $\bar{g}_{\text{Th}}(p_1, p_2, p_3, p_4) = \bar{g}_{\text{Th}}(p_3, p_4, p_1, p_2)$. Although we expressed our model in the irreducible representation now, we will still think of the underlying reducible Thirring model when speaking of flavor numbers, *etc.*, in order to conform with the literature. In other words, N_f denotes the number of reducible flavors, and $\tilde{N} = 4N_f$ as in Section 3.

Flow equations. Using the effective average action (4.4), we can derive the flow equations for g_{GN} and g_{Th} as described in Section 2.2. By a calculation similar to the Gross-Neveu case, details of which can be found in Appendix B.3, we find that

$$\begin{aligned}\partial_t g_{\text{GN}} = & \left[1 + 2\eta^{(4)} + \sum_j p_j \cdot \nabla_{p_j} \right] g_{\text{GN}} - {}_0^{\tilde{N}} B^{\mathfrak{s}2}[g_{\text{GN}}, g_{\text{GN}}] + {}_0^2 B^{\mathfrak{s}1}[g_{\text{GN}}, g_{\text{GN}}] + {}_0^3 B_{\leftrightarrow}^{\mathfrak{s}1}[g_{\text{GN}}, g_{\text{Th}}] \\ & + {}_0^1 B_{\leftrightarrow}^{\mathfrak{t}}[g_{\text{GN}}, g_{\text{Th}}] + {}_0^2 B^{\mathfrak{t}}[g_{\text{Th}}, g_{\text{Th}}] - {}_0^1 B_{\leftrightarrow}^{\mathfrak{u}}[g_{\text{GN}}, g_{\text{Th}}] + {}_0^2 B^{\mathfrak{u}}[g_{\text{Th}}, g_{\text{Th}}],\end{aligned}\quad (4.5a)$$

$$\begin{aligned}\partial_t g_{\text{Th}} = & \left[1 + 2\eta^{(4)} + \sum_j p_j \cdot \nabla_{p_j} \right] g_{\text{Th}} - {}_{-\tilde{N}} B^{\mathfrak{s}2}[g_{\text{Th}}, g_{\text{Th}}] - {}_{-1}^1 B_{\leftrightarrow}^{\mathfrak{s}1}[g_{\text{GN}}, g_{\text{Th}}] + {}_{-2}^2 B^{\mathfrak{s}1}[g_{\text{Th}}, g_{\text{Th}}] \\ & + {}_{1/2}^0 B^{\mathfrak{t}}[g_{\text{GN}}, g_{\text{GN}}] + {}_{-1/2}^1 B_{\leftrightarrow}^{\mathfrak{t}}[g_{\text{GN}}, g_{\text{Th}}] + {}_{1/2}^2 B^{\mathfrak{t}}[g_{\text{Th}}, g_{\text{Th}}] \\ & - {}_{1/2}^0 B^{\mathfrak{u}}[g_{\text{GN}}, g_{\text{GN}}] + {}_{-1/2}^1 B_{\leftrightarrow}^{\mathfrak{u}}[g_{\text{GN}}, g_{\text{Th}}] - {}_{1/2}^2 B^{\mathfrak{u}}[g_{\text{Th}}, g_{\text{Th}}],\end{aligned}\quad (4.5b)$$

where we suppressed the η -dependence of the diagram functionals for brevity. As a first observation we remark that all four types of diagrams worked out in the general analysis of Section 2.2 enter the flow equations now, *i.e.* there are also \mathfrak{t} - and \mathfrak{u} -channel processes contributing. Nevertheless, the \mathfrak{s} -channel is still dominating: For the flow of g_{GN} , there are more \mathfrak{s} -channel diagrams than \mathfrak{t} - or \mathfrak{u} -channel ones, and the functionals ${}_0^1 B_{\leftrightarrow}^{\mathfrak{t}}[g_{\text{GN}}, g_{\text{Th}}]$ and ${}_0^1 B_{\leftrightarrow}^{\mathfrak{u}}[g_{\text{GN}}, g_{\text{Th}}]$ come with opposite signs, such that they are expected to cancel partly. For the flow of g_{Th} , this is the case for the \mathfrak{t} - and \mathfrak{u} -channel diagrams both of order $(g_{\text{GN}})^2$ and of order $(g_{\text{Th}})^2$. Yet we can anticipate a richer momentum structure of fixed points and perturbations compared to the pure Gross-Neveu model.

The anomalous dimension function receives contributions from both couplings, too. Evaluating the traces in Eq. (2.36) (*cf.* Appendix B.4 for details), we obtain

$$\eta = \Sigma^1[g_{\text{GN}}; \eta] - \Sigma^1[g_{\text{Th}}; \eta] + \tilde{N} \Sigma^2[g_{\text{Th}}; \eta].\quad (4.6)$$

In particular, the Thirring coupling also contributes a term via the Σ^2 diagram which persists even in the large- N_f limit. As a sanity check, observe that Eqs. (4.5a) and (4.6) reduce to the pure Gross-Neveu relations (3.4) and (3.5) if $g_{\text{Th}} \equiv 0$.

4.2 Limiting cases

Pointlike limit. As the simplest limit case, we first consider constant couplings, *i.e.* pointlike interactions [31, 32, 94]. Using the reduction formula (2.29) for the diagram functionals, we conclude that the anomalous dimension vanishes and the flow equations for the coupling constants are given by

$$\partial_t g_{\text{GN}} = g_{\text{GN}} + \frac{4v_d}{\tilde{N}} \ell_1^{(F)}(0; 0) \left[(-\tilde{N} + 2) g_{\text{GN}}^2 + 6g_{\text{GN}}g_{\text{Th}} + 4g_{\text{Th}}^2 \right],\quad (4.7a)$$

$$\partial_t g_{\text{Th}} = g_{\text{Th}} + \frac{4v_d}{\tilde{N}} \ell_1^{(F)}(0; 0) \left[\frac{\tilde{N} + 2}{3} g_{\text{Th}}^2 + 2g_{\text{GN}}g_{\text{Th}} \right],\quad (4.7b)$$

in agreement with Refs. [94, 95]. We see that the pure Gross-Neveu model forms an invariant subspace in this limit: Setting $g_{\text{Th}} \equiv 0$, the equations remain consistent and Eq. (4.7a) reduces

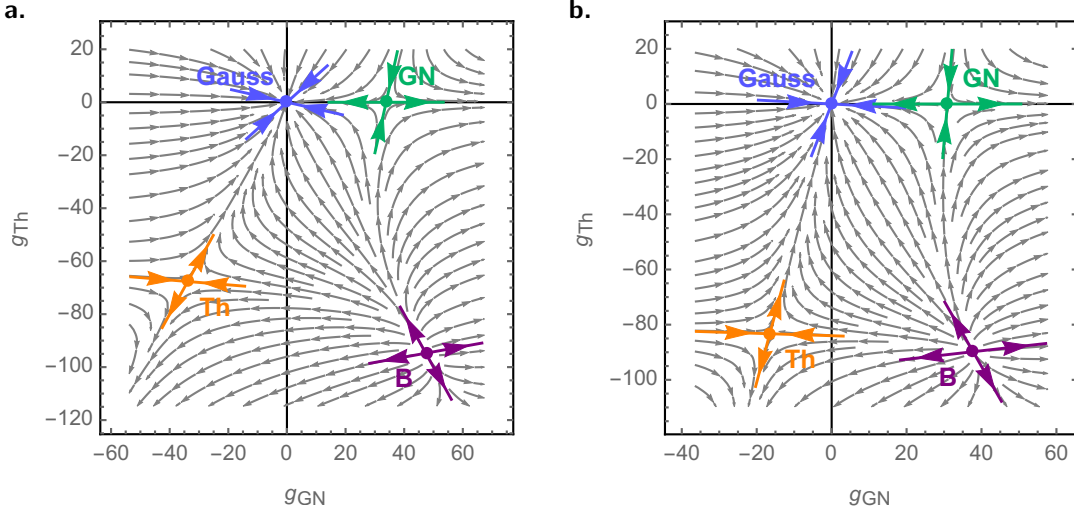


Figure 21: Fixed points, eigenperturbations, and example flows in the pointlike Gross-Neveu-Thirring space for (a) $N_f = 4$ and (b) $N_f = 12$. The GN fixed point always lies on the Gross-Neveu axis, the Th fixed point approaches the Thirring axes only as $N_f \rightarrow \infty$.

to Eq. (3.6). Hence the Gross-Neveu fixed point (GN) still exists and lies at the same position in theory space as in the pointlike pure Gross-Neveu model. In addition, we now find two more nontrivial fixed points at

$$\text{Th :} \quad g_{\text{GN},*} = \frac{\tilde{N}^2 - \sqrt{\tilde{N}^2 + 112\tilde{N} + 256}(\tilde{N} + 2) - 14\tilde{N} + 112}{2c^{(F)}\frac{\tilde{N}-2}{\tilde{N}}(\tilde{N}^2 + 4\tilde{N} + 40)},$$

$$g_{\text{Th},*} = -\frac{3\tilde{N}^2}{c^{(F)}\left(\tilde{N}^2 + \sqrt{\tilde{N}^2 + 112\tilde{N} + 256} + \tilde{N} + 16\right)}, \quad (4.8a)$$

$$\text{B :} \quad g_{\text{GN},*} = \frac{\tilde{N}^2 + \sqrt{\tilde{N}^2 + 112\tilde{N} + 256}(\tilde{N} + 2) - 14\tilde{N} + 112}{2c^{(F)}\frac{\tilde{N}-2}{\tilde{N}}(\tilde{N}^2 + 4\tilde{N} + 40)},$$

$$g_{\text{Th},*} = \frac{3\tilde{N}^2}{c^{(F)}\left(-\tilde{N}^2 + \sqrt{\tilde{N}^2 + 112\tilde{N} + 256} - \tilde{N} - 16\right)}, \quad (4.8b)$$

which we will refer to as the Thirring (Th) and B fixed points, respectively [17, 31, 32]. Here $c^{(F)} = 4v_d\ell_1^{(F)}(0;0)$. The resulting theory space topology is plotted in Fig. 21 for $N_f = 4$ ($\tilde{N} = 16$) and $N_f = 12$ ($\tilde{N} = 48$). In fact, Fig. 2 already showed the same theory space for $N_f = 2$ ($\tilde{N} = 8$). The Th fixed point lies on the Thirring axis $g_{\text{GN}} = 0$ for $N_f = \infty$, but wanders off toward negative values of g_{GN} as N_f is decreased. Both GN and Th are critical fixed points in the sense that they have one relevant direction, and the B fixed point has two relevant directions. The Gaussian fixed point remains irrelevant. A detailed discussion of the pointlike purely fermionic Gross-Neveu-Thirring model may be found in Ref. [31].

s-Channel approximation. We argued above that the s-channel still dominates the flows of g_{GN} and g_{Th} . Seeing as we need to reduce the complexity of Eqs. (4.5), we will employ an s-channel approximation once more and assume $g_{\text{GN}} = g_{\text{GN}}(\mathfrak{s})$, $g_{\text{Th}} = g_{\text{Th}}(\mathfrak{s})$. Again, we must fix a momentum configuration, which will generally be one of those from Fig. 7, to close the flow equations for this reduced dependence. Of course, we will have to check stability of the results under variation of the configuration again, too. The flow equations become

$$\partial_t g_{\text{GN}} = \left[1 + 2\eta^{(4)}\right]g_{\text{GN}} + 2\mathfrak{s}g'_{\text{GN}} - {}_0^{\tilde{N}}B^{\mathfrak{s}2}[g_{\text{GN}}, g_{\text{GN}}] + {}_0^2B^{\mathfrak{s}1}[g_{\text{GN}}, g_{\text{GN}}] + {}_0^3B^{\mathfrak{s}1}[g_{\text{GN}}, g_{\text{Th}}] + {}_0^1B_{\leftrightarrow}^{\mathfrak{t}}[g_{\text{GN}}, g_{\text{Th}}] + {}_0^2B^{\mathfrak{t}}[g_{\text{Th}}, g_{\text{Th}}] - {}_0^1B_{\leftrightarrow}^{\mathfrak{u}}[g_{\text{GN}}, g_{\text{Th}}] + {}_0^2B^{\mathfrak{u}}[g_{\text{Th}}, g_{\text{Th}}], \quad (4.9a)$$

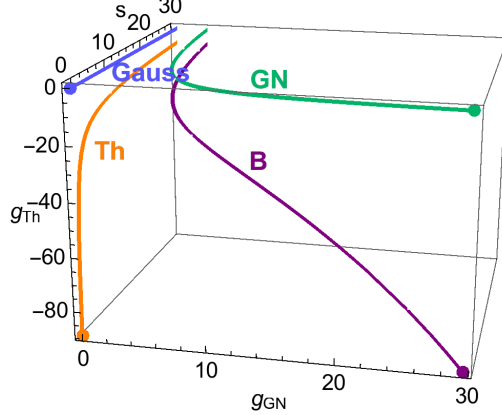


Figure 22: Large- N_f fixed points of the Gross-Neveu-Thirring model in the \mathfrak{s} -channel approximation. The points mark the positions of the fixed points in the pointlike limit, which match the function values at $\mathfrak{s} = 0$ as they should for $N_f = \infty$.

$$\begin{aligned} \partial_t g_{\text{Th}} = & \left[1 + 2\eta^{(4)} \right] g_{\text{Th}} + 2\mathfrak{s} g'_{\text{Th}} + \frac{\tilde{N}}{N} B^{\mathfrak{s}2}[g_{\text{Th}}, g_{\text{Th}}] - \frac{1}{2} B_{\leftrightarrow}^{\mathfrak{s}1}[g_{\text{GN}}, g_{\text{Th}}] + \frac{2}{2} B^{\mathfrak{s}1}[g_{\text{Th}}, g_{\text{Th}}] \\ & + \frac{1}{2} B^{\mathfrak{t}}[g_{\text{GN}}, g_{\text{GN}}] + \frac{1}{2} B_{\leftrightarrow}^{\mathfrak{t}}[g_{\text{GN}}, g_{\text{Th}}] + \frac{1}{2} B^{\mathfrak{t}}[g_{\text{Th}}, g_{\text{Th}}] \\ & - \frac{1}{2} B^{\mathfrak{u}}[g_{\text{GN}}, g_{\text{GN}}] + \frac{1}{2} B_{\leftrightarrow}^{\mathfrak{u}}[g_{\text{GN}}, g_{\text{Th}}] - \frac{1}{2} B^{\mathfrak{u}}[g_{\text{Th}}, g_{\text{Th}}]. \end{aligned} \quad (4.9b)$$

It is instructive to take another look at the diagram functionals (3.21) in the \mathfrak{s} -channel approximation. The $\mathfrak{s}2$ -diagram is obviously independent of the choice of momentum configuration. For the $\mathfrak{s}1$ -diagram, the \mathcal{Q} integration is trivial in the parallel configuration, and the \mathfrak{t} - and \mathfrak{u} -favored orthogonal configurations yield the same value up to variations in η , as already noted in Section 3.5. Regarding the \mathfrak{t} - and \mathfrak{u} -diagrams, we first remark that their contributions agree (neglecting η) in the parallel and symmetric configurations because $\mathfrak{t} = \mathfrak{u}$ in both, and both are invariant under $p_3 \longleftrightarrow p_4$. Those contributions to the flow equations that come with opposite signs in the \mathfrak{t} - and \mathfrak{u} -channels will therefore approximately cancel in these configurations. On the contrary, we have the two orthogonal configurations, where either $\mathfrak{t} = \mathfrak{s}$, $\mathfrak{u} = 0$ (\mathfrak{t} -favored) or $\mathfrak{t} = 0$, $\mathfrak{u} = \mathfrak{s}$ (\mathfrak{u} -favored). Consequently, either of the two channels is set off against the other. Together, those four momentum configurations should therefore give a good impression of the overall variation and uncertainty of the \mathfrak{s} -channel approximation.

Regarding the anomalous dimension function, we notice that the self-energy diagram functional Σ^2 vanishes in the \mathfrak{s} -channel approximation because the integrand is odd in the loop momentum. Hence we are left with

$$\eta = \Sigma^1[g_{\text{GN}}; \eta] - \Sigma^1[g_{\text{Th}}; \eta]. \quad (4.10)$$

For the remainder of Section 4, we will be concerned with solving these \mathfrak{s} -channel approximated Eqs. (4.9) and (4.10).

Large- N_f limit. In the limit $N_f \rightarrow \infty$, we are still in the pleasing situation of being able to compute the fixed point coupling functions exactly. As in the pure Gross-Neveu case, the anomalous dimension function vanishes and only the $\mathfrak{s}2$ -diagrams remain in the flow equations. Consequently, the equations decouple and both take the form (3.35) with $a_1 = 1$, $a_2 = 0$ for g_{GN} and $a_1 = -1$, $a_2 = 1$ for g_{Th} . Thus the formal solution (3.38) can be carried over immediately. For the GN fixed point, $g_{\text{Th}} = 0$ and using the linear regulator (1.10), the explicit solution (3.40) still holds for g_{GN} . For the Th fixed point, $g_{\text{GN}} = 0$ and the explicit form of g_{Th} is a modified version of (3.40) due to different values of a_1 and a_2 . Since the expressions are even lengthier than the ones for the Gross-Neveu coupling, we do not spell them out explicitly here. We merely note that maximum regularity requires $g_\infty = -1/32$ for g_{Th} . Finally, the B fixed point is obtained by combining the nontrivial solutions for g_{GN} and g_{Th} . A plot of all four fixed points of the Gross-Neveu-Thirring model in the large- N_f limit is shown in Fig. 22.

As Eq. (3.44) is still valid as a solution of the linearized flow equation for both g_{GN} and g_{Th} , the spectra can be adopted similarly. Since we can perturb in the GN and Th directions independently,

the spectrum is the union of eigenvalues in both directions. Assuming maximum regularity as before, the GN and Th fixed points thus have one relevant exponent $\theta_1 = 1$ each, whereas the B fixed point has two relevant exponents, $\theta_1 = \theta_2 = 1$.

4.3 Finite- N_f fixed points and spectra

Having explored these limiting cases, we come back to the momentum-dependent model for finite flavor number in the \mathfrak{s} -channel approximation, characterized by Eqs. (4.9) and (4.10). Compared to the large- N_f limit, the situation is considerably more complex because all four types of diagram functionals contribute to the flow equations of the couplings, and all involve integrals of the unknown functions g_{GN} , g_{Th} , and η .

Overview of the fixed point structure. To compute fixed point functions, we proceed in the same way as for the pure Gross-Neveu model and expand the unknown functions as series of Chebyshev rational functions (3.47). By the pseudospectral method, we reduce the integro-differential equations to a system of nonlinear algebraic equations for the Chebyshev coefficients $g_{\text{GN},n}$, $g_{\text{Th},n}$, and η_n . As before, we then solve this system numerically using a Newton-Raphson iteration. Details of this procedure for the enhanced model can be found in Appendix B.6. For all subsequently presented solutions, we employed the exponential regulator (1.11) again. The expansion orders were at least $n_{\text{max}}^g = 40$, $n_{\text{max}}^\eta = 12$. For small flavor numbers, we increased them up to $n_{\text{max}}^g = 45$, $n_{\text{max}}^\eta = 20$ when necessary to achieve acceptable accuracy.

We show a selection of fixed point coupling functions for different flavor numbers in Fig. 23. The actual solutions for the four momentum configurations of Fig. 7 are plotted as solid lines. To visualize the deviation among them, we additionally display elliptic tubes around the mean of these configurations with principle axes given by the standard deviations. The overall picture satisfies our expectation from the limiting cases and the pure Gross-Neveu model: We can distinguish four different regions of fixed point solutions which approximately coincide with the positions in the pointlike limit, and the coupling functions decay as $\mathfrak{s} \rightarrow \infty$.

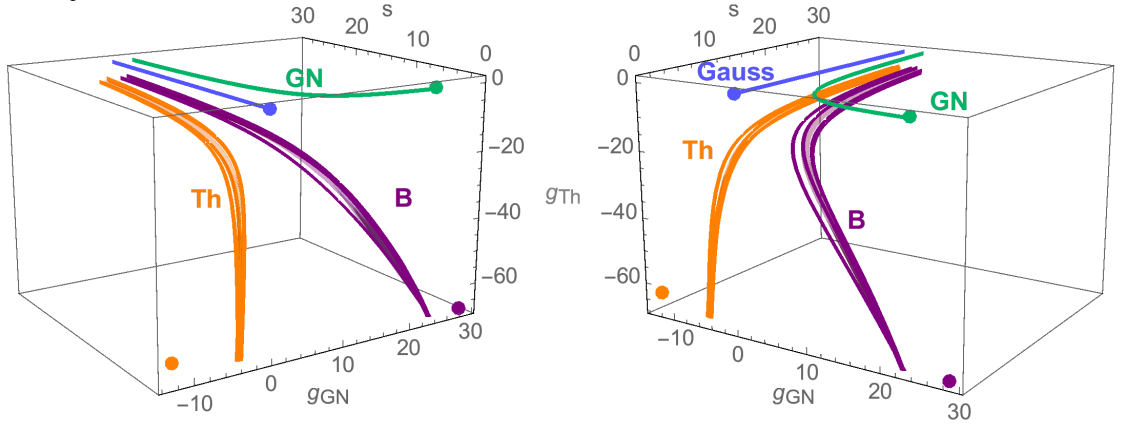
For relatively large flavor numbers, *e.g.* $N_f = 12$ in Fig. 23a, the variation with momentum configuration is very small for all fixed points and the solutions are close to the infinite- N_f solution (*cf.* Fig. 22). This is a manifestation of the fact that the \mathfrak{s} -channel approximation is closed in this limit. For smaller values of N_f , the GN fixed point remains stable when varying the momentum configuration, similarly to the situation observed in Section 3.5. However, the deviations between configurations increase significantly for the Th and B fixed points. In fact we cannot even assure the existence of the B fixed point in the current approximation since we were unable to find solutions for all configurations when $N_f < 2$.

The general picture is very similar for the anomalous dimension functions plotted in Fig. 24. The variation increases again for smaller values of N_f . Interestingly, it is largest for the Th fixed point and rather small for the B fixed point. We will analyze all three nontrivial fixed points in more detail below after having established the corresponding spectra.

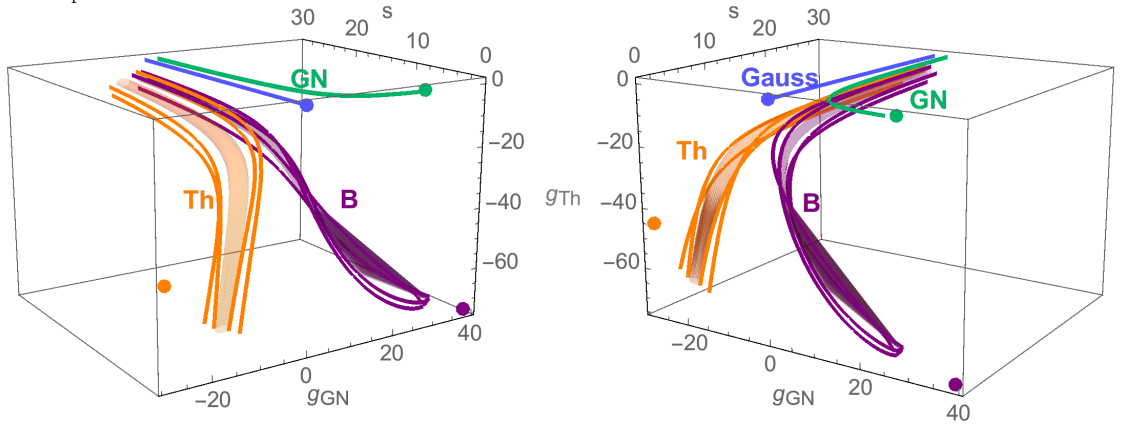
Computation of critical exponents. In order to compute spectra of the fixed points, we will use the same methods as for the pure Gross-Neveu model again. Perturbing around a fixed point solution with $g_{\text{GN}}(\mathfrak{s}) = g_{\text{GN},*}(\mathfrak{s}) + e^{-\theta t} \varepsilon_{\text{GN}}(\mathfrak{s})$ and $g_{\text{Th}}(\mathfrak{s}) = g_{\text{Th},*}(\mathfrak{s}) + e^{-\theta t} \varepsilon_{\text{Th}}(\mathfrak{s})$ and expanding the flow equations (4.9) to first order in ε , we arrive at the eigenvalue equations

$$\begin{aligned} -\theta \varepsilon_{\text{GN}} = & \left[1 + 2\eta^{(4)} + 2\mathfrak{s} \partial_{\mathfrak{s}} \right] \varepsilon_{\text{GN}} - {}_0^{\tilde{N}} B_{\leftrightarrow}^{\mathfrak{s}2} [g_{\text{GN},*}, \varepsilon_{\text{GN}}] \\ & + {}_0^2 B_{\leftrightarrow}^{\mathfrak{s}1} [g_{\text{GN},*}, \varepsilon_{\text{GN}}] + {}_0^3 B_{\leftrightarrow}^{\mathfrak{s}1} [g_{\text{GN},*}, \varepsilon_{\text{Th}}] + {}_0^3 B_{\leftrightarrow}^{\mathfrak{s}1} [\varepsilon_{\text{GN}}, g_{\text{Th},*}] \\ & + {}_0^1 B_{\leftrightarrow}^{\mathfrak{t}} [g_{\text{GN},*}, \varepsilon_{\text{Th}}] + {}_0^1 B_{\leftrightarrow}^{\mathfrak{t}} [\varepsilon_{\text{GN}}, g_{\text{Th},*}] + {}_0^2 B_{\leftrightarrow}^{\mathfrak{t}} [g_{\text{Th},*}, \varepsilon_{\text{Th}}] \\ & - {}_0^1 B_{\leftrightarrow}^{\mathfrak{u}} [g_{\text{GN},*}, \varepsilon_{\text{Th}}] - {}_0^1 B_{\leftrightarrow}^{\mathfrak{u}} [\varepsilon_{\text{GN}}, g_{\text{Th},*}] + {}_0^2 B_{\leftrightarrow}^{\mathfrak{u}} [g_{\text{Th},*}, \varepsilon_{\text{Th}}], \end{aligned} \quad (4.11a)$$

a. $N_f = 12$



b. $N_f = 3$



c. $N_f = 2$

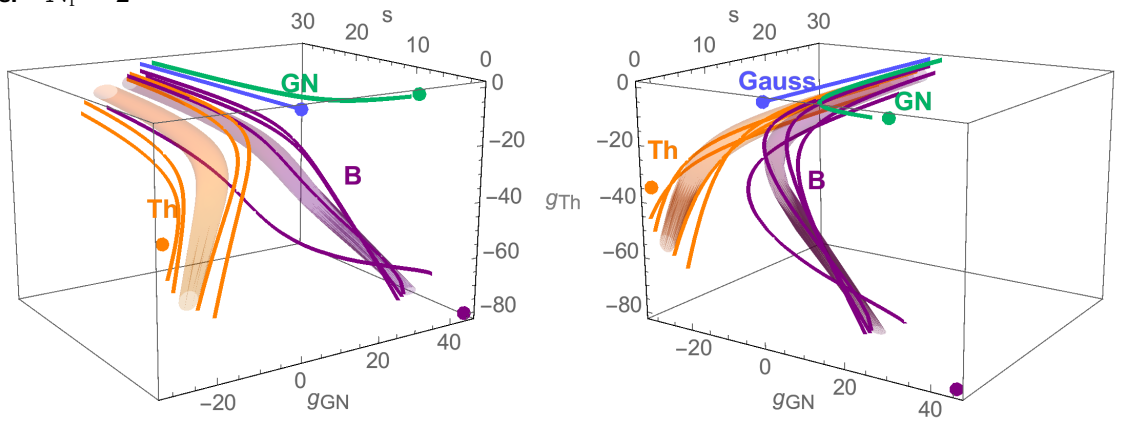


Figure 23: Fixed point coupling functions of the Gross-Neveu-Thirring model for various flavor numbers. The solid lines correspond to the four different momentum configurations while the semi-transparent tubes visualize the mean plus one standard deviation between these configurations. The points mark the fixed point positions in the pointlike limit.

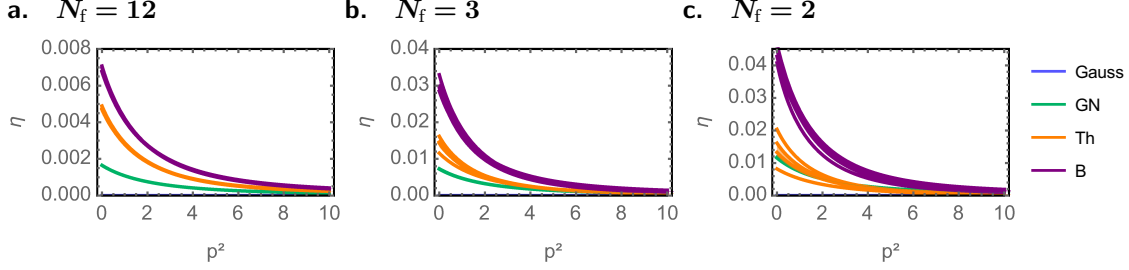


Figure 24: Fixed point anomalous dimension functions of the Gross-Neveu-Thirring model for various flavor numbers and the four different momentum configurations.

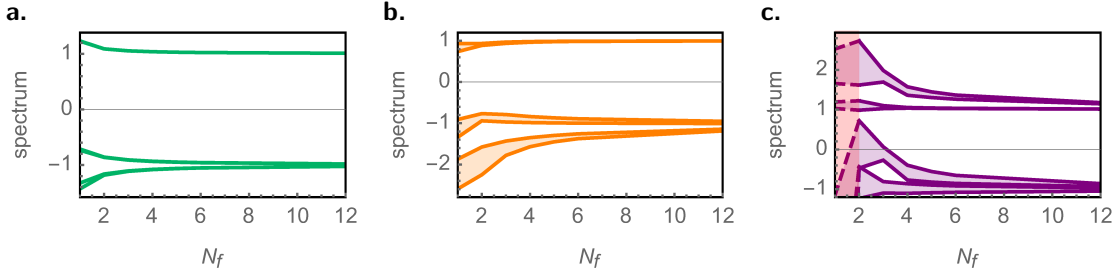


Figure 25: Leading eigenvalues of the (a) GN, (b) Th, and (c) B fixed points. The shaded area corresponds to the range spanned by the minimum and maximum value obtained for different momentum configurations. The additional red shading at $N_f = 1 \dots 2$ in (c) is to indicate that these results are disputable due to diminished or even missing convergence of fixed point solutions.

$$\begin{aligned}
-\theta \varepsilon_{\text{Th}} = & \left[1 + 2\eta^{(4)} + 2\mathfrak{s} \partial_{\mathfrak{s}} \right] \varepsilon_{\text{Th}} + \frac{\tilde{N}}{N} B_{\leftrightarrow}^{\mathfrak{s}2} [g_{\text{Th},*}, \varepsilon_{\text{Th}}] \\
& - \frac{1}{2} B_{\leftrightarrow}^{\mathfrak{s}1} [g_{\text{GN},*}, \varepsilon_{\text{Th}}] - \frac{1}{2} B_{\leftrightarrow}^{\mathfrak{s}1} [\varepsilon_{\text{GN}}, g_{\text{Th},*}] + \frac{2}{2} B_{\leftrightarrow}^{\mathfrak{s}1} [g_{\text{Th},*}, \varepsilon_{\text{Th}}] \\
& + \frac{1}{2} B_{\leftrightarrow}^{\mathfrak{t}} [g_{\text{GN},*}, \varepsilon_{\text{GN}}] - \frac{1}{2} B_{\leftrightarrow}^{\mathfrak{t}} [g_{\text{GN},*}, \varepsilon_{\text{Th}}] - \frac{1}{2} B_{\leftrightarrow}^{\mathfrak{t}} [\varepsilon_{\text{GN}}, g_{\text{Th},*}] + \frac{2}{2} B_{\leftrightarrow}^{\mathfrak{t}} [g_{\text{Th},*}, \varepsilon_{\text{Th}}] \\
& - \frac{1}{2} B_{\leftrightarrow}^{\mathfrak{u}} [g_{\text{GN},*}, \varepsilon_{\text{GN}}] - \frac{1}{2} B_{\leftrightarrow}^{\mathfrak{u}} [g_{\text{GN},*}, \varepsilon_{\text{Th}}] - \frac{1}{2} B_{\leftrightarrow}^{\mathfrak{u}} [\varepsilon_{\text{GN}}, g_{\text{Th},*}] - \frac{2}{2} B_{\leftrightarrow}^{\mathfrak{u}} [g_{\text{Th},*}, \varepsilon_{\text{Th}}].
\end{aligned} \tag{4.11b}$$

Contrary to the large- N_f case, we cannot consider perturbations in the g_{GN} and g_{Th} directions independently because the equations do not decouple. To extract the eigenvalues, we then expand the eigenperturbations as a series of Chebyshev rational functions with a scaling prefactor (3.55) as before. However, we restrict to the fixed maximum growth scheme with $a_{\max} = \text{const}$ because it is computationally more efficient and the extracted exponents proved to match with the running asymptotics scheme for the Gross-Neveu model studied in the previous section. Evaluating the linearized flow equations (4.11) on the collocation grid $\{\mathfrak{s}_m\}$, we obtain an algebraic eigenvalue equation of the form (3.56) again, but now with components for both g_{GN} and g_{Th} , schematically

$$-\theta \begin{pmatrix} \mathbf{P} & \mathbf{0} \\ \mathbf{0} & \mathbf{P} \end{pmatrix} \begin{pmatrix} \varepsilon_{\text{GN}} \\ \varepsilon_{\text{Th}} \end{pmatrix} = \begin{pmatrix} \mathbf{J}_{\text{GN,GN}} & \mathbf{J}_{\text{GN,Th}} \\ \mathbf{J}_{\text{Th,GN}} & \mathbf{J}_{\text{Th,Th}} \end{pmatrix} \begin{pmatrix} \varepsilon_{\text{GN}} \\ \varepsilon_{\text{Th}} \end{pmatrix}. \tag{4.12}$$

For explicit expressions of the Jacobians, we refer to Appendix B.6. By calculating the eigenvalues for different values of a_{\max} and checking consistency, we can extract the spectra of the fixed points.

A plot of the leading eigenvalues of the three nontrivial fixed points is presented in Fig. 25. For each eigenvalue, we show its minimum and maximum value for different momentum configurations. Again, the values essentially coincide for the GN fixed point, and they vary only moderately at the Th fixed point for small N_f . Both of them have one relevant exponent as in the pointlike and large- N_f limits. The B fixed point shows stronger variations and seemingly also a qualitative change of behavior seeing as a third relevant exponent turns up in some configuration below $N_f \lesssim 3$. In any case, the large- N_f limit is reflected nicely as the eigenvalues approach the values found in Section 4.2. Let us now have a closer look at the three interacting fixed points individually.

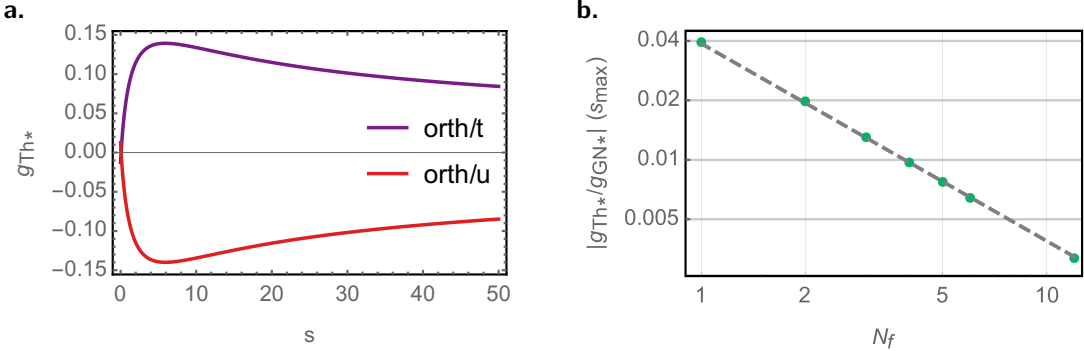


Figure 26: Violation of the invariance subspace property of the Gross-Neveu model; (a) Thirring coupling at the Gross-Neveu fixed point in the orthogonal configurations for $N_f = 2$. Note that $g_{Th} \equiv 0$ in the parallel and symmetric configurations; (b) ratio of Thirring and Gross-Neveu couplings at the maximum of the Thirring coupling as a function of N_f (log-log plot).

Gross-Neveu fixed point. We recall that, in the pointlike approximation, the Gross-Neveu vertex forms an invariant subspace of theory space, meaning that the coupling g_{GN} does not contribute alone to the flow of any of the other symmetry-compatible vertices [95] and in particular not to the flow of g_{Th} in Eq. (4.7). The flow equations of the fully momentum-dependent model (4.5) tell us that this does not hold in general: There are t - and u -channel processes of order g_{GN}^2 entering the flow of g_{Th} , which happen to cancel in the pointlike limit. Consequently, the Gross-Neveu coupling does not parametrize an invariant subspace any longer because setting $g_{Th} \equiv 0$ in Eqs. (4.7), we cannot find a consistent general fixed point solution $g_{GN,*}$. This should serve as a word of caution when restricting the theory space to pure Gross-Neveu interactions as it was done in many previous studies and also in Section 3 of this work.

Nevertheless, the violation of this invariance is reassuringly mild, at least in the s -channel approximation. On the level of the plots in Fig. 23, there is no visible difference. To illustrate how far the fixed point solutions actually leave the Gross-Neveu subspace, we characterize the Thirring coupling at the Gross-Neveu fixed point in Fig. 26. The example for $N_f = 2$ in Panel (a) shows $g_{Th,*}$ for the orthogonal configurations, where its value is about two orders of magnitude smaller than $g_{GN,*}$. For the parallel and symmetric configurations, where $t = u$, the corresponding diagrams of order g_{GN}^2 in Eq. (4.5b) cancel such that $g_{Th,*} \equiv 0$ at the Gross-Neveu fixed point. Panel (b) shows the ratio of the Thirring and Gross-Neveu couplings at the maximum of the Thirring coupling, *i.e.* $\left| \frac{g_{Th,*}(s_{\max})}{g_{GN,*}(s_{\max})} \right|$ with s_{\max} such that $|g_{Th,*}(s)| \leq |g_{Th,*}(s_{\max})|$ for all s . This coupling ratio reaches up to 4% for $N_f = 1$ and decays like $1/N_f$ with the flavor number. Hence the restriction to g_{GN} alone remains a good approximation.

Regarding the spectrum, the resulting picture is basically unaffected compared to the pure Gross-Neveu calculation in Section 3.6, apart from the extra eigenvalues in the irrelevant part of the spectrum due to the additional Thirring degree of freedom in the perturbations. For the relevant exponent, we obtain the same numerical values.

With hindsight, the Gross-Neveu fixed point remains largely independent of the Thirring vertex even in the momentum-dependent model within the considered precision. Hence a reduction to the pure Gross-Neveu model is justified if one is interested in the Gross-Neveu universality class, at least in the irreducible representation of γ matrices. In the reducible representation, the two additional vertices in (2.3) may in principle lead to more invariance-violating terms, although we expect these terms to be of similar order as the Thirring corrections.

Thirring fixed point. As for the Th fixed point solution, the variation with momentum configuration is much larger and becomes significant for small flavor numbers. Fig. 23 shows that the s -channel approximation is rather crude and cannot capture all essential dependencies. As expected, the outermost Th solutions correspond to the two orthogonal configurations where the influence of either of the remaining two Mandelstam channels is maximally exposed against the other, and the parallel and symmetric configurations lie in between. The same holds true for

Table 4: Characteristics of the Thirring model for various flavor numbers and compared to results from other methods.

a. Critical exponents with error bounds given by the variation with the external momentum configuration. This provides a lower bound of the error only and does not include deviations between different regularization schemes. In addition, the differences between the distances to the NJL and Thirring subspaces at $\mathfrak{s} = 0$ and $\mathfrak{s} = \infty$ are given.

N_f	θ_1	η_ψ	$\Delta_{\text{NJL-Th}}^0$	$\Delta_{\text{NJL-Th}}^\infty$
1	0.84(10)	0.004(9)	-0.59(11)	-0.67(4)
2	0.91(2)	0.014(6)	-0.13(24)	-0.54(16)
3	0.95(2)	0.013(2)	0.19(12)	-0.36(32)
4	0.97(1)	0.012(1)	0.34(7)	-0.28(42)
5	0.983(4)	0.010(1)	0.42(4)	-0.16(42)
6	0.989(3)	0.0088(4)	0.47(3)	-0.06(39)
12	0.9967(3)	0.0047(1)	0.59(1)	0.27(25)

b. Comparison between exponents obtained by different methods for $N_f = 2$. Regarding the comparability of FRG and MC results, also note the remarks in the main text. Abbreviations: FRG/-bos. (functional renormalization group, bosonization), MC (Monte Carlo).

method	θ_1	η_ψ
FRG (here)	0.91(2)	0.014(6)
FRG/bos. [32]	0.4	—
MC, staggered [49]	1.41(8)	—
MC, staggered [50]	1.18(1)	0.37(1)

the anomalous dimensions (Fig. 24), where we observe considerable variation between the configurations for small momenta. From top to bottom, the curves in both figures belong to the t -favored orthogonal, symmetric, parallel, and u -favored orthogonal configurations, respectively. We conclude that momentum dependence becomes increasingly important as N_f becomes smaller, and that it does not suffice to consider just the \mathfrak{s} -channel, let alone the pointlike limit, to resolve all features. Nevertheless, the qualitative picture is consistent and the additional momentum dependence does not change the theory space topologically.

This notion is reinforced by looking at the critical exponents in Fig. 25b. Deviations between the momentum configurations become visible only for small N_f and are stronger in the subleading exponents, whose accuracy is naturally lower. The leading exponent, however, varies only little down to $N_f = 2$, where the differences affect the second decimal place and are presumably still smaller than those from regulator variations for fixed momentum configuration. Exponents for various flavor numbers are listed in Tab. 4a with error ranges corresponding to the configurational variation bands in Figs. 24 and 25b. For the anomalous dimension $\eta_\psi = \eta(0)$, the differences between the momentum configurations are larger. The general trend is again a decreasing value with increasing N_f , eventually converging to $\eta_\psi = 0$ as $N_f \rightarrow \infty$. The value for $N_f = 1$, however, is out of line since η_ψ becomes smaller here and actually turns negative in some configurations, namely the parallel and u -favored orthogonal ones. Seeing as this does not occur in all configurations, we cannot certify it to be a physical effect and a finer resolution of momentum dependence will be needed to settle this question.

Comparing to Monte Carlo simulations is less straightforward than one might think. Early studies usually used staggered fermions [25, 28, 49, 50, 125, 126], and some of the reported results are listed in Tab. 4b. However, it is unclear whether the symmetries of the lattice models coincide with the continuum Thirring model or rather fall into the Gross-Neveu universality class, *i.e.* whether or not the Thirring fixed point governs the IR behavior of the lattice models [31, 51]. In particular certain popular lattice actions for Gross-Neveu and Thirring models were shown to have the same symmetries and critical exponents [51, 127]. Moreover, the $U(2N_f)$ symmetry is not manifest in the formulation with staggered fermions and only emerges in the continuum limit. Recent studies using domain-wall [54] or SLAC [33] fermions, where $U(2N_f)$ -invariance is built into the lattice action, do not find a Thirring fixed point for integer N_f at all. On the contrary, chiral symmetry breaking is observed for odd numbers of Weyl spinors in the irreducible representation, corresponding to half-integer N_f in the reducible formulation [33]. Then again, the lattice studies usually work with a pure Thirring model where no further interaction vertex is considered. Since we know that the Th fixed point does not lie directly in the Thirring subspace for finite N_f , small distortions between

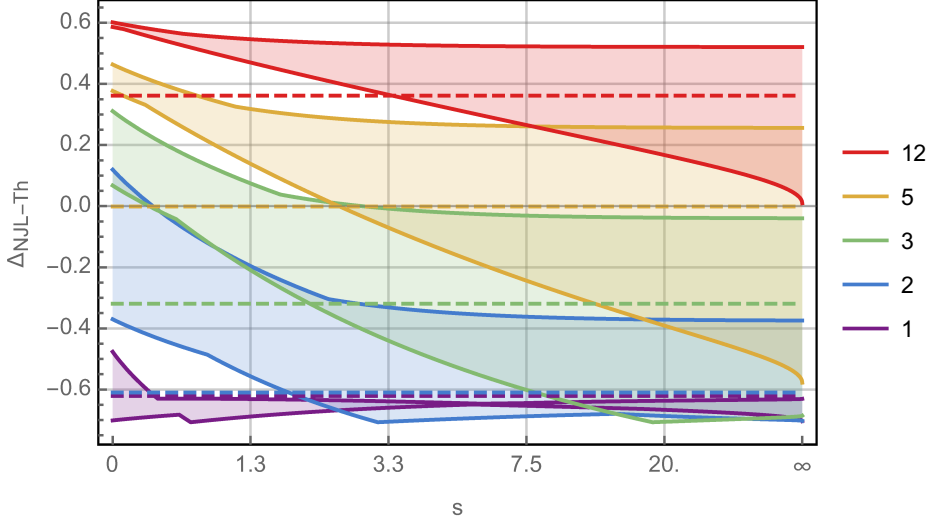


Figure 27: Comparison of the distance of the Th fixed point solution from the NJL and Thirring subspaces for various flavor numbers. The shaded areas depict the variation among momentum configurations. Note that the kinks in the boundary are caused by the absolute value in the definition of d_{NJL} and the fact that the configuration with minimum/maximum value for $\Delta_{\text{NJL-Th}}$ changes with s . The dashed lines indicate the values found in the pointlike limit.

the methods are expected and the Monte Carlo simulations may, for instance, feel a stronger influence of the B fixed point. Nevertheless, by projecting onto the Thirring subspace in the FRG computation, we still expect to find a fixed point.

Critical flavor number. Another observation already made in the pointlike limit [31, 32] is that the Th fixed point wanders away from the Thirring subspace and towards an NJL-type subspace as N_f decreases. In the irreducible representation, the NJL vertex is given by the scalar flavor nonsinglet [32]

$$g_{\text{NJL}}(p_1, p_2, p_3, p_4) \bar{\chi}^i(-p_1) \chi^j(p_4) \bar{\chi}^j(-p_3) \chi^i(p_2).$$

By a Fierz transformation (2.6), we can relate it to the Gross-Neveu and Thirring couplings and obtain

$$g_{\text{NJL}}(p_1, p_2, p_3, p_4) = -\frac{1}{2} [g_{\text{GN}}(p_1, p_2, p_3, p_4) + g_{\text{Th}}(p_1, p_2, p_3, p_4)] \quad (4.13)$$

with the above specified convention for the external momenta. Put differently, the NJL subspace is characterized by $g_{\text{GN}} = g_{\text{Th}}$. In the pointlike limit, this condition is achieved for $N_f = 1.75$ [32] as can be seen by equating $g_{\text{GN},*}$ and $g_{\text{Th},*}$ in Eq. (4.8a). The distance of a point $(g_{\text{GN}}, g_{\text{Th}})$ in theory space to the NJL subspace is thus given by

$$d_{\text{NJL}} := \frac{|g_{\text{Th}} - g_{\text{GN}}|}{\sqrt{2}}, \quad (4.14)$$

which is a function of the external momenta or, in our case, the Mandelstam variable s . In a similar fashion, we can define the distance from the Thirring subspace as $d_{\text{Th}} := |g_{\text{GN}}|$. In Ref. [32] it was argued that the presence or absence of chiral symmetry breaking is caused by a competition between the NJL and Thirring interactions, where the former supports the formation of a chiral condensate, but the latter does not. To assess this trade-off, we compare the distances of the Th fixed point solution from the NJL and Thirring subspaces in Fig. 27. More precisely, we plot the difference $d_{\text{NJL}} - d_{\text{Th}}$ and divide it by the location of the fixed point as a function of s :

$$\Delta_{\text{NJL-Th}} := \frac{d_{\text{NJL}} - d_{\text{Th}}}{\sqrt{g_{\text{GN}}^2 + g_{\text{Th}}^2}}. \quad (4.15)$$

As before, we indicate the variation between the different momentum configurations by a shaded area. Negative values mean that the solution is closer to the NJL subspace, whereas for positive values it is closer to the Thirring subspace. The dashed lines in the figure show the values of this

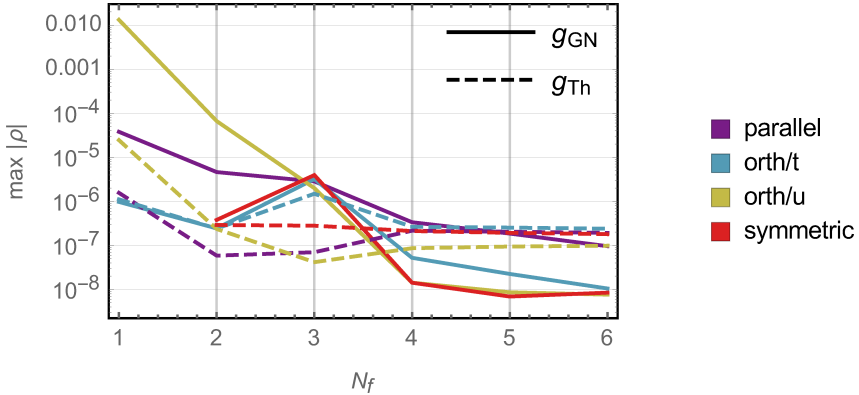


Figure 28: Absolute residuals of the B fixed point solutions for different flavor numbers and momentum configurations. The solid lines correspond to the g_{GN} components, the dashed ones to the g_{Th} components.

difference as found in the pointlike limit. We emphasize that the value $N_f = 5.01$ where $d_{\text{NJL}} = d_{\text{Th}}$ lies very close to the critical value $N_{f,\text{crit}} = 5.1(7)$ reported in Ref. [32] and obtained by keeping track of the chiral order parameter $\langle \bar{\psi} \psi \rangle$ directly. In the momentum-dependent model using the s -channel approximation, we observe that the fixed point solutions tend to be closer to the Thirring subspace for small values of s . This suggests $N_{f,\text{crit}}$ to be slightly smaller than the pointlike value, but extracting a precise number is difficult due to the significant configurational variations and the fact that our approach does not give direct access to the order parameter. In particular, since the variations of $\Delta_{\text{NJL-Th}}$ with momentum configuration increase tremendously as $s \rightarrow \infty$, there are values of s for which the pointlike difference lies within the bounds set by the momentum configurations for all flavor numbers. Since $\Delta_{\text{NJL-Th}}$ is a relative measure, this increase is to be attributed in parts to the fact that $g_{\text{GN}}, g_{\text{Th}} \rightarrow 0$ as $s \rightarrow \infty$. Explicit estimates and variations for $\Delta_{\text{NJL-Th}}$ at $s = 0$ and $s = \infty$ are listed in Tab. 4a.

In any case, an indicator for chiral symmetry breaking to occur is $d_{\text{NJL}} \lesssim d_{\text{Th}}$. Requiring this condition for *some* s and *all* momentum configurations leads to $3 < N_{f,\text{crit}} < 4$. If we require that it hold at $s = 0$ for *some* momentum configuration, we find $2 < N_{f,\text{crit}} < 3$. Requiring it for *all* s and *all* momentum configurations gives $6 < N_{f,\text{crit}} < 12$. Qualitatively, these observations and the mere presence of the Th fixed point thus reinforce the existence of a critical flavor number.

B fixed point. Let us finally discuss the B fixed point, which is to some extent more mysterious than the other two nontrivial fixed points. As with the Th fixed point, the variation between the couplings (Fig. 23) for different momentum configurations increases significantly when N_f becomes smaller. The anomalous dimensions (Fig. 24), by contrast, exhibit much less deviations even for small flavor numbers. However, most disconcerting about the B fixed point is the loss of precision for the fixed point solutions as illustrated in Fig. 28.

The plot shows the maximum absolute residual of the B fixed point solutions for our four standard momentum configurations and one to six flavors, where the expansion orders are fixed at $n_{\text{max}}^g = 40$, $n_{\text{max}}^{\eta} = 12$. Apparently, the residuals increase for all configurations as N_f is lowered, and they do so particularly dramatically for the u -favored orthogonal configuration. This should be contrasted with the behavior at the Th fixed point, where no such increase of the approximation error is observed and the absolute residuals stay below 10^{-7} for all N_f at the same expansion order. Moreover, and especially for $N_f = 1, 2$, it became much harder to find solutions in the suspected region of the B fixed point at all and more fine-tuning of the initial guesses was required compared to the other fixed points or larger flavor numbers. In fact, we were even unable to reach a converging solution for $N_f = 1$ in the symmetric configuration.

From the plots in Figs. 23b and c, the B fixed point solutions appear to merge into the Th solution as $s \rightarrow \infty$. Indeed, some of the configurations cross over from $g_{\text{GN}} > 0$ to $g_{\text{GN}} < 0$ at these small flavor numbers, experiencing a root in the g_{GN} coupling. Nevertheless, there is no clear pattern regarding the positions of these roots. From asymptotic considerations (*cf.* Section 3.3) we know that all four fixed points eventually converge to $g_{\text{GN}} = g_{\text{Th}} = 0$ as $s \rightarrow \infty$. The observations here

suggest that there may be a prior amalgamation of the Th and B fixed points. With the increase of residuals for small N_f in mind, however, this merger could also be an artifact indicating that the solver gets stuck at two different fixed points for small and large values of \mathfrak{s} .

Likewise, the spectrum at the B fixed point (Fig. 25c) shows greater uncertainties compared to the Th (let alone the GN) fixed point. The red shading for $N_f = 1\dots 2$ is to indicate that the large residuals and the lack of convergence in the symmetric configuration cast doubts on whether the obtained functions are actual solutions. In any case, the fixed point has two relevant directions for large N_f as in the pointlike limit and the bosonized formulation [32]. At $N_f = 2, 3$, an additional third relevant exponent occurs in the u -favored orthogonal configuration. Since this is also the regime where the residuals of the corresponding fixed-point solutions begin to increase, it remains again unclear whether this extra relevant direction is physical.

4.4 Connection to the bosonized formulation

We already compared our results of the previous section with those obtained in earlier studies using a dynamically bosonized version of the Gross-Neveu-Thirring model [32, 94]. Here we would like to clarify the relation between the two formulations by considering a mean-field approximation of the bosonized model, similar to the presentation in Section 3.2 for the pure Gross-Neveu model.

Effective average action. The Hubbard-Stratonovich transformation for the Thirring vertex works analogously to the Gross-Neveu case, only that we need a vector boson $V = (V_\mu)$ to couple to the fermionic Thirring current. In the lowest order LPA', the effective average action for the bosonized version of Eq. (4.4) then takes the form

$$\begin{aligned} \Gamma_k[\phi, V, \chi, \bar{\chi}] = & \int_p \left[-Z_\chi \bar{\chi}(p) \not{p} \chi(p) + \frac{1}{2} \phi(-p) (Z_\phi p^2 + \bar{m}_\phi^2) \phi(p) \right. \\ & + \frac{1}{2} (Z_V p^2 + \bar{m}_V^2) V_\mu(-p) V_\mu(p) + \frac{1}{2} (\bar{A}_V - Z_V) p_\mu p_\nu V_\mu(-p) V_\nu(p) \left. \right] \\ & + \int_{p, p'} [i \bar{h}_\phi \phi(-p - p') \bar{\chi}(-p) \chi(p') - \bar{h}_V V_\mu(-p - p') \bar{\chi}(-p) \sigma_\mu \chi(p')] , \end{aligned} \quad (4.16)$$

where Z_V and \bar{A}_V parametrize the transversal and longitudinal components of the kinetic term, similar to the conventions of Ref. [32]. This bosonized effective action illustrates the connection between the Thirring model and QED₃. The vector boson V_μ here couples to the fermion fields in a similar way as the photon there. However, the vector mass term as well as the longitudinal kinetic term proportional to \bar{A}_V (“gauge-fixing term”) in the action (4.16) explicitly break the U(1) gauge symmetry.

At this order, the scalar and vector bosons do not couple directly, so that the mean field result (3.17) for the scalar ϕ still holds. To obtain the corresponding relation for the vector boson, we again solve the equations of motion, $\delta \Gamma_k / \delta V_\mu(q) = 0$, leading to

$$V_\mu(-q) = \frac{\bar{h}_V}{Z_V q^2 + \bar{m}_V^2} \int_p \left[\bar{\chi}(q + p) \sigma_\mu \chi(p) + \frac{Z_V - \bar{A}_V}{\bar{A}_V q^2 + \bar{m}_V^2} q_\mu \bar{\chi}(q + p) \not{p} \chi(p) \right]. \quad (4.17)$$

This links the vector boson V_μ to the fermion vector-current condensates proportional to $\bar{\chi} \sigma_\mu \chi$.

Effective four-fermion interactions. Substituting this mean-field relation for the vector boson and the previously obtained result for the scalar boson into the effective action (4.16), we get back a purely fermionic action of the form

$$\begin{aligned} \Gamma_k[\cdot, \cdot, \chi, \bar{\chi}] = & - \int_p Z_\chi \bar{\chi}(p) \not{p} \chi(p) + \frac{1}{2} \int_{p_2, p_3, p_4} \frac{\bar{h}_\phi^2}{Z_\phi(p^s)^2 + \bar{m}_\phi^2} \bar{\chi}(-p_1) \chi(p_2) \bar{\chi}(-p_3) \chi(p_4) \\ & - \frac{1}{2} \int_{p_2, p_3, p_4} \frac{\bar{h}_V^2}{Z_V(p^s)^2 + \bar{m}_V^2} \bar{\chi}(-p_1) \sigma_\mu \chi(p_2) \bar{\chi}(-p_3) \sigma_\mu \chi(p_4) \\ & + \frac{1}{2} \int_{p_2, p_3, p_4} \frac{\bar{h}_V^2 (\bar{A}_V - Z_V)(1 + \bar{A}_V - Z_V)}{[\bar{A}_V(p^s)^2 + \bar{m}_V^2]^2} \bar{\chi}(-p_1) \not{p}^s \chi(p_2) \bar{\chi}(-p_3) \not{p}^s \chi(p_4) , \end{aligned} \quad (4.18)$$

where $p^s = p_3 + p_4$. Hence the bosonized model encodes an s -channel momentum dependence in the Thirring vertex, too. The effective coupling function takes the same form as in the Gross-Neveu case, *cf.* Eq. (3.19), apart from a minus sign due to different sign conventions. In addition, the vector boson parametrizes a further interaction vertex resembling the square of the kinetic term, $(\bar{\chi} p^s \chi)^2$. This type of interaction is present if $\bar{A}_V \neq Z_V$ and is not resolved in our momentum-dependent Gross-Neveu-Thirring model (4.4). Its appearance here provides one possible explanation for the increased deviations between the various momentum configurations in the s -channel approximation observed in the previous section. Hence the vertex should be a primary candidate to be included in advanced investigations of the momentum-dependent setting.

* * *

Investigating the Thirring model with momentum-dependent couplings in a truncation that is complete at the level of non-derivative four-fermion interactions confirmed many previously found properties of the model's theory space. As in the pointlike and bosonized formulations, we find three interacting fixed points, two of which have a single relevant direction and control the IR behavior of the Gross-Neveu and Thirring models, respectively. The third fixed point has two relevant directions at large flavor numbers as in the pointlike limit, but may pick up additional relevant operators as the flavor number reaches $N_f \approx 3$. Nevertheless, since convergence of fixed point solutions worsens for small N_f , we cannot definitely establish the existence of this fixed point for all flavor numbers and momenta.

Contrary to the pointlike or bosonized formulations, the Gross-Neveu vertex does not define an invariant subspace in a fully momentum-dependent treatment. The violations of this invariance property are, however, minute, and can safely be neglected at least at the current order of truncation, where the momentum dependence is well-covered by the s -channel approximation. By contrast, additional interaction channels contribute significantly to the flow in the vicinity of the Thirring fixed point. This effect increases as N_f becomes smaller, corroborating the importance of momentum fluctuations in this limit. Stronger variations with momentum configuration suggest that the dependence is not reliably parametrized in the s -channel approximation, pointing to missing contributions from other channels or vertices. By analogy with the bosonized model, one such important vertex may be given by a kinetic term squared.

Regarding the question of a critical flavor number for chiral symmetry breaking, our findings support results from previous FRG studies that discerned competing NJL- and Thirring-type interactions as a reason for the transition. Due to limitations of the purely fermionic formalism in the employed truncation, in particular the inaccessibility of the chiral order parameter, we cannot provide precise estimates for the critical N_f , but the results suggest values of the same order as in previous studies.

5 Conclusions

In this thesis, we examined the renormalization group flow of fermionic quantum field theories in a vertex expansion of the effective average action. In particular, we investigated the momentum-dependent coupling functions of the Gross-Neveu and Thirring models, two popular and widely applied theories with a quartic fermionic self-interaction, in (2+1) spacetime dimensions. These models are frequently used to describe electronic properties of condensed matter systems such as graphene and high-temperature cuprate superconductors, to approximate low-energy regimes of fundamental interactions, or to exemplify asymptotic safety and chiral symmetry breaking in high-energy physics.

To our knowledge, this work is the first extensive study of these relativistic fermion systems with momentum-dependent interaction couplings. In this regard we were able to extend the characterization of the momentum dependence compared to previous FRG examinations using pointlike interactions and bosonization techniques. Connecting to these earlier works helped to clarify in what way momentum dependence of the interactions is encoded there. While many of the findings in the pointlike setting could be confirmed, we observed a few modifications or complications in the momentum-dependent formulation that we will comment on below in more detail again. Similarly, a comparison with results obtained by different methods yielded qualitative agreement in many aspects, but some differences remained.

According to the Wetterich equation, the foundation of the FRG formalism used here, the Feynman diagrams contributing to the flow of vertex functions have a one-loop structure. Under rather general assumptions, we showed that the renormalization flow of four-fermion interactions is driven by four different processes, which we labeled by the Mandelstam variables s , t , and u characterizing the momentum transfer across the loop. Thereby, the s -channel, associated with the propagation of flavor-contracted composite states, turned out to be dominating in many respects. First of all, there are two s -channel diagrams as against just one t - and u -channel diagram, respectively. As a consequence, s -channel processes contribute the majority of terms to the flow of the Gross-Neveu and Thirring coupling functions. In addition, these happen to be the only diagrams remaining in the limit of large flavor number N_f . Moreover, the partially bosonized formulations investigated in the literature effectively resolve an s -channel momentum dependence, too.

In a similar fashion we worked out the contributions of four-fermion vertices to the flow of the momentum-dependent fermionic wave function renormalization, *i.e.* a generalized anomalous dimension. Here we found two different processes occurring, both of which vanish in the pointlike limit, so that the inclusion of momentum dependence leads to a nontrivial extension in the purely fermionic formulation.

Due to momentum-dependent anomalous dimension and couplings, the RG flows are given by a set of multidimensional, nonlinear, integro-differential equations, which to solve in generality would require a tremendous computational effort. To reduce complexity and inspired by the dominance of the s -channel, we thus employed a restriction of the coupling functions' momentum dependence to the Mandelstam variable s . With the exception of the infinite- N_f limit, the flow equations of the considered models are not closed under this reduction, so that we additionally needed to choose a particular configuration of the external momenta to fix the equations unambiguously. Varying this configuration allowed us to assess the influence of other interaction channels and the quality of the s -channel approximation.

The infinite- N_f limit, however, does not show this ambiguity, and here we were indeed able to solve the associated fixed point equations exactly and provide closed analytic expressions for the Gross-Neveu and Thirring coupling functions. In the theory space spanned by these two couplings, we found a total of four fixed points as in the pointlike limit. These are the trivial Gaussian fixed point, one interacting fixed point in both the Gross-Neveu and Thirring subspaces, labeled GN and Th, respectively, and the combination of these two, labeled B. The solutions are bounded functions that decay to zero as s is increased. Nevertheless, they are not analytic in s , with series expansions involving half-integer powers of the variable both as $s \rightarrow 0$ and $s \rightarrow \infty$, a fact that may be ascribed to the singular character of the Mandelstam variable s as a function of

the constituting momenta and to the nonlocality of the interaction in the momentum-dependent setting. The latter observation underlines the nonperturbative character of our FRG approach. The resulting critical exponents corresponding to the fixed point solutions are bounded from above, but quantization of the spectrum as in the bosonized language is only achieved by enforcing a maximum regularity condition for the fixed point coupling and perturbations. Then again, this condition is automatically fulfilled for finite flavor numbers, so that this extra requirement is a peculiarity of the infinite- N_f limit. Eventually, we find one relevant direction for both the GN and Th fixed points, and consequently two relevant directions for the B fixed point, in qualitative and quantitative agreement with previous investigations using different approaches.

For finite N_f , the flow equations become more involved and we needed to switch to numerical methods to extract fixed point solutions and their critical properties. Our main tool were pseudospectral expansions of couplings and anomalous dimensions in terms of Chebyshev rational functions, which allowed us to obtain high-precision solutions of the fixed point and linearized flow equations. We found that the overall fixed point structure resembles the infinite- N_f and pointlike limits in the sense there are four fixed points, with the GN and Th fixed points remaining critical, *i.e.* they retain their single relevant direction. The coupling and anomalous dimension functions decay to zero as $\mathfrak{s} \rightarrow \infty$, hence all fixed points merge into the Gaussian one in this limit.

The GN fixed point is the controlling interacting fixed point of the Gross-Neveu model. Before we examined it in an extended theory space with additional Thirring coupling, we investigated the pure Gross-Neveu model with just a scalar four-fermion vertex in some detail. This way we were able to test the approximation scheme and to assess the quality of solutions depending on various parameters such as expansion orders, compactification scale, momentum parametrization and configuration, *etc.* In any case, *i.e.* in both the pure Gross-Neveu and the Gross-Neveu-Thirring models, the fixed point proved to be largely insensitive to variations of the momentum configuration, indicating that the \mathfrak{s} -channel approximation captures the essential features of the momentum dependence. Besides the above mentioned reasons, this stability of solutions backs up the \mathfrak{s} -channel approximation *a posteriori*. In the pure Gross-Neveu model, there are in fact no contributions from the t - and u -channels to the flow of the coupling function, reinforcing the dominance of the \mathfrak{s} -channel. While this changes when including the Thirring vertex, the modifications are only minute. Consequently, the pointlike and bosonized approximations appear to be well justified.

There is, however, a conceptionally important observation from the momentum-dependent analysis affecting pointlike approximations. In the latter, it is found that the Gross-Neveu vertex forms an invariant subspace with respect to other four-fermion interactions such as the Thirring vertex, which has been used to warrant the omission of other vertices in studies of the Gross-Neveu model in the past. Crucially, this invariant subspace property does not survive once the full momentum dependence of coupling functions is considered because, for instance, the Thirring flow receives contributions from pure Gross-Neveu interactions. These happen to cancel in the pointlike limit, but not in the general case nor in the \mathfrak{s} -channel approximation. Notwithstanding, the violations of the invariance are very minor and decrease with increasing flavor number. Even for $N_f = 1$, the relative departure from the Gross-Neveu subspace in the Thirring direction amounts to 4% maximum. Furthermore, these modifications do not affect the resulting critical exponents. As for the physics of the Gross-Neveu model, the restriction to the single defining vertex thus remains a legitimate approximation.

Regarding critical exponents, our calculations show deviations from previous results. The most striking one concerns the convergence of the leading eigenvalue θ_1 to its large- N_f limit. From $1/N_f$ expansions, it is known that the limiting value should be approached from below, whereas we find a monotonic decay as a function of the flavor number. Apart from that, quantitative deviations compared to results obtained by other methods arise for small flavor numbers. These range between 10...15% for θ_1 and reach up to 50% for the anomalous dimension η_ψ . It should be mentioned, though, that the other methods studied so far do not provide an entirely consistent picture in this regard either. The anomalous dimension remains positive for all N_f and converges to its limiting value $\eta_\psi = 0$ as $N_f \rightarrow \infty$, too. We point out that limited precision of our numerical estimates is to be attributed in parts to the missing direct modeling of the fermion condensate $\langle \bar{\psi} \psi \rangle$. Being the order parameter of the chiral phase transition described by the GN fixed point, it is expected to

contribute crucially to the correlation function exponents θ_1 and η_ψ . Here bosonized formulations of the theory have an advantage.

In the Thirring model, by contrast, processes other than \mathfrak{s} -channel ones play a more important part. For finite N_f , the Th fixed point wanders off the Thirring axis, but it continues to be the controlling fixed point of the Thirring model. The variation of fixed point solutions among different momentum configurations increases significantly for small N_f and leads to numerical deviations for technically universal quantities such as critical exponents. This supports the general notion that the momentum dependence becomes increasingly important for small flavor numbers. Hence one reason for the increased deviations is the greater significance of \mathfrak{t} - and \mathfrak{u} -channels. In the \mathfrak{s} -channel approximation, these are insufficiently incorporated, which is emphasized by the observation that the difference is largest between the two orthogonal momentum configurations that exclusively single out the dependence on either \mathfrak{t} or \mathfrak{u} against the other. Therefore, ideally, one would want to include both variables as arguments of the coupling functions, but currently this seems to be too ambitious from a computational point of view. A compromise could be to include one of the two or a weighted average. Another reason for the variations with momentum configuration is suggested by the bosonized formulation of the Thirring model. Here we noticed that the mean-field approximation encodes a second four-fermion vertex besides the Thirring interaction. This extra vertex, having the structure of a kinetic term squared, potentially carries important information about the momentum dependence in the Thirring model. Adding it to the considered theory space could therefore be another reasonable extension of this work.

As mentioned above, the Th fixed point exists as a critical point with one relevant direction for all N_f in our analysis. The relevant eigenvalue $\theta_1 \approx 1$ exhibits surprisingly little variation upon changing the external momentum configuration. Except for $N_f = 1$, the differences are in fact smaller than the anticipated regularization dependence. As N_f is increased, the infinite- N_f limit is now approached from below and the variation between momentum configurations reduces as expected. Likewise, the subleading eigenvalues converge to their limiting values with diminished variations. For the anomalous dimensions η_ψ , these variations are generally larger and the overall trend is again that η_ψ decreases with growing N_f as in the Gross-Neveu model. However, the case of one fermion flavor stands out here, too, because η_ψ turns negative in some configurations, a phenomenon whose origin is not yet fully understood. In any case, $N_f = 1$ is a puzzling limit also at the third interacting fixed point B.

Seeing as the Th fixed point departs from the Thirring axis, our findings suggest that chiral symmetry breaking is in principle possible for all finite values of N_f . However, a competition between the inhibiting Thirring subspace and the encouraging NJL subspace as found in Ref. [32] appears reasonable from our findings. Based on similar arguments, the critical flavor number below which spontaneous symmetry breaking occurs should lie between $N_{f,\text{crit}} = 2 \dots 12$, which is admittedly a rather crude estimate and does not help to settle this question on a quantitative level. Anyhow, this observation complies with Dyson-Schwinger and perturbative calculations [24, 45] as well as early lattice simulations [25, 28, 49, 50]. Nevertheless, it disagrees with recent Monte Carlo studies [33, 54, 55] that do not observe chiral symmetry breaking at integer flavor numbers, which is unfortunate because these recent lattice simulations were the first ones to use fermion implementations that manifestly obey the symmetries of the continuum Thirring model.

From a physical point of view, the B fixed point is less interesting because it does not directly govern the IR behavior of a particular model or describe a known second-order phase transition. Notwithstanding, it is important for the overall topology of the theory space in our truncation and may remotely affect theories defined in the Thirring subspace. Similar to the Th fixed point, the B fixed point exhibits growing variations with momentum configuration for small flavor numbers. These are actually considerably stronger because they also affect the leading eigenvalues significantly: The number of relevant directions of the fixed point for $N_f \lesssim 3$, where a third one emerges in some configurations, is inconclusive. Such a third relevant direction could hint at further fixed points since the corresponding eigenflows must eventually approach an IR limit; however, the extra fixed point might also lie at infinity.

Another issue with the B fixed point concerns the increasingly poor convergence of our solution method for small flavor numbers. First, the residuals of the fixed point solutions for fixed expansion order increase dramatically for all configurations and most noticeably the \mathfrak{u} -favored orthogonal one,

which is a development absent at the GN or Th fixed points. Second, we needed to fine-tune the initial guesses provided to the solver much more thoroughly to find solutions at all and even failed to do so in the symmetric configuration for $N_f = 1$. Third, we observed a sign change of fixed point solutions in the Gross-Neveu coupling for larger values of \mathfrak{s} , meaning that the B fixed point appeared to merge into the Th fixed point. These findings could either mean that the B fixed point vanishes for small flavor numbers in certain configurations of the external momenta or that it diversifies, potentially developing a continuum, such that the solver jumps between two or more solutions in subsequent iterations. Either way, a more sophisticated answer to this questions will require an advanced resolution of the coupling functions' momentum dependence.

All in all, our momentum-dependent analysis agrees with previous FRG studies in many aspects and confirms the validity of derivative expansions and bosonization techniques to parametrize momentum dependences. The obtained theory space is topologically similar, showing the same number of fixed points and separatrices. Regarding the computation of critical exponents, the bosonized language is in fact superior because it gives direct access to the order parameters of the phase transitions associated with critical fixed points. On the other hand, the fully momentum dependent treatment of four-fermion interactions revealed some caveats of pointlike approximations, most notably the occurrence of additional terms in the flow equations and the resulting breakdown of invariance symmetries in theory space.

Immediate generalizations of our studies could extend the momentum dependence of coupling functions or include other four-fermion vertices such as the extra one entailed in the bosonized formulation of the Thirring model. Both extensions are expected to locate the Th and B fixed points more precisely. To address the question of dynamical mass generation, it could also be intriguing to compute momentum-dependent wave function renormalizations in the vicinity of the Th fixed point. This would provide access to the fermion propagator, whose pole structure encodes the fermion mass.

Acknowledgments

First and foremost, I would like to thank my supervisor Holger Gies for his supportive and sophisticated guidance through this master thesis project. I greatly appreciate the numerous physical insights and that he was always approachable and open for questions and discussions. Furthermore, I also thank Omar Zanusso for consenting to examine this thesis.

Besides I would like to give my special thanks to Benjamin Knorr, who accompanied this research from the beginning, contributed many great ideas along the way and made valuable comments on the manuscript. Not least, he was always available and willing to help with problems or requests.

I also want to thank my fellow workmates Alessandro, Christian – thanks a lot for proofreading the draft, too –, Julia, Julian, Micha, and Riccardo for plenty of chats and discussions about physics and nonphysics issues and amusing lunch and coffee breaks.

All the more, I would like to thank my family and friends for their support and distraction, both of which proved to be crucial for academic and personal prosperity.

A Abbreviations and conventions

Serving as a quick reference, we collect various abbreviations and conventions used throughout the thesis in this appendix. They are sorted alphabetically by key word.

Diagram functionals. The diagrams for the self-renormalization of a four-fermion interaction can occur in four different variants. These can be characterized by the Mandelstam variables \mathfrak{s} , \mathfrak{t} , and \mathfrak{u} , where the \mathfrak{s} -channel has two realizations. They are depicted in Fig. 4. The mathematical expressions for these Feynman diagrams are

$$\begin{aligned} {}_{a_2}^{a_1} B^{\mathfrak{s}2}[g_1, g_2; \eta](p_i) := \frac{1}{\tilde{N}} \int_q {}_{a_2}^{a_1} K_1^{(F)}(p_3 + p_4, q; \eta) [g_1(p_1, p_2, q', -q) g_2(q, -q', p_3, p_4) \\ + (q \longleftrightarrow -q')]_{q' = q + p_3 + p_4}, \end{aligned} \quad (\text{A.1a})$$

$$\begin{aligned} {}_{a_2}^{a_1} B^{\mathfrak{s}1}[g_1, g_2; \eta](p_i) := \frac{1}{\tilde{N}} \int_q {}_{a_2}^{a_1} K_1^{(F)}(p_3 + p_4, q; \eta) [g_1(p_1, p_2, q', -q) g_2(p_3, -q', q, p_4) \\ + (q \longleftrightarrow -q')]_{q' = q + p_3 + p_4}, \end{aligned} \quad (\text{A.1b})$$

$$\begin{aligned} {}_{a_2}^{a_1} B^{\mathfrak{t}}[g_1, g_2; \eta](p_i) := \frac{1}{\tilde{N}} \int_q {}_{a_2}^{a_1} K_1^{(F)}(p_2 + p_3, q; \eta) [g_1(p_1, q', -q, p_4) g_2(-q', p_2, p_3, q) \\ + (q \longleftrightarrow -q')]_{q' = q + p_2 + p_3}, \end{aligned} \quad (\text{A.1c})$$

$$\begin{aligned} {}_{a_2}^{a_1} B^{\mathfrak{u}}[g_1, g_2; \eta](p_i) := \frac{1}{\tilde{N}} \int_q {}_{a_2}^{a_1} K_1^{(F)}(p_2 + p_4, q; \eta) [g_1(p_1, q', p_3, -q) g_2(-q', p_2, q, p_4) \\ + (q \longleftrightarrow -q')]_{q' = q + p_2 + p_4}. \end{aligned} \quad (\text{A.1d})$$

with $\tilde{N} = N_f d_\gamma$. Here the left/top and right/bottom vertices are denoted by g_1 and g_2 , respectively, and the symbol “ $+(q \longleftrightarrow -q')$ ” means that all previous terms on the same bracket level have to be added with q and $-q'$ interchanged. The self-energy contributions from four-fermion vertices, sketched in Fig. 5, are parametrized by the diagram functionals

$$\Sigma^1[g; \eta](p^2) := -\frac{1}{\tilde{N}} \int_q \left(\frac{q \cdot p}{q^2 p^2} \right) \frac{\partial_t r_1(q^2) - \eta(q^2) r_1(q^2)}{[1 + r_1(q^2)]^2} g(-p, -q, q, p), \quad (\text{A.2a})$$

$$\Sigma^2[g; \eta](p^2) := -\frac{1}{\tilde{N}} \int_q \left(\frac{q \cdot p}{q^2 p^2} \right) \frac{\partial_t r_1(q^2) - \eta(q^2) r_1(q^2)}{[1 + r_1(q^2)]^2} g(-p, p, -q, q). \quad (\text{A.2b})$$

In the \mathfrak{s} -channel approximation, the diagram functionals reduce to

$${}_{a_2}^{a_1} B^{\mathfrak{s}2}[g_1, g_2; \eta](p_i) = \frac{2}{N} g_1(\mathfrak{s}) g_2(\mathfrak{s}) \sigma_{d-2} \int d(q, u) {}_{a_2}^{a_1} K(\mathfrak{s}, q, u; \eta), \quad (\text{A.3a})$$

$${}_{a_2}^{a_1} B^{\mathfrak{s}1}[g_1, g_2; \eta](p_i) = \frac{1}{N} g_1(\mathfrak{s}) \int d(q, u, \Omega) {}_{a_2}^{a_1} K(\mathfrak{s}, q, u; \eta) [g_2([q + p_3]^2) + g_2([q + p_4]^2)], \quad (\text{A.3b})$$

$$\begin{aligned} {}_{a_2}^{a_1} B^{\mathfrak{t}}[g_1, g_2; \eta](p_i) = \frac{1}{\tilde{N}} \int d(q, u, \Omega) {}_{a_2}^{a_1} K(\mathfrak{t}, q, u; \eta) \\ \times [g_1([q - p_1]^2) g_2([q + p_2]^2) + g_1([q - p_4]^2) g_2([q + p_3]^2)], \end{aligned} \quad (\text{A.3c})$$

$$\begin{aligned} {}_{a_2}^{a_1} B^{\mathfrak{u}}[g_1, g_2; \eta](p_i) = \frac{1}{\tilde{N}} \int d(q, u, \Omega) {}_{a_2}^{a_1} K(\mathfrak{u}, q, u; \eta) \\ \times [g_1([q - p_1]^2) g_2([q + p_2]^2) + g_1([q - p_3]^2) g_2([q + p_4]^2)], \end{aligned} \quad (\text{A.3d})$$

where the coordinate system for the loop integrals is chosen such that the z -component points along the momentum transfer vector $p^{\mathfrak{m}}$. Note that one has to fix a momentum configuration in order to resolve the arguments entering the coupling functions in the integrands. The self-energy diagram Σ^2 vanishes in this approximation. For Σ^1 , we obtain

$$\Sigma^1[g; \eta](p^2) = - \int d(q, u) \frac{\sigma_{d-2}}{\tilde{N}(2\pi)^d} \left(\frac{u}{\sqrt{p^2} q} \right) \frac{\partial_t r_1(q^2) - \eta(q^2) r_1(q^2)}{[1 + r_1(q^2)]^2} g(q^2 + p^2 + 2q\sqrt{p^2}u). \quad (\text{A.4})$$

Fourier transformation. Our conventions for the Fourier transformation and its inverse are:

$$\psi(x) = \int \frac{d^d p}{(2\pi)^d} \psi(p) e^{ip \cdot x} \quad \Leftrightarrow \quad \psi(p) = \int d^d x \psi(x) e^{-ip \cdot x}, \quad (\text{A.5a})$$

$$\bar{\psi}(x) = \int \frac{d^d p}{(2\pi)^d} \bar{\psi}(p) e^{-ip \cdot x} \quad \Leftrightarrow \quad \bar{\psi}(p) = \int d^d x \bar{\psi}(x) e^{ip \cdot x}. \quad (\text{A.5b})$$

Gamma matrices. Please refer to Appendix B.1.

Indices. Spacetime indices are denoted by Greek letters $\mu, \nu, \rho, \sigma, \alpha, \beta, \dots = 1, \dots, d$. Flavor indices use Latin letters $i, j, \dots = 1, \dots, N_f$ and are usually suppressed. Both follow Einstein summation, *i.e.* indices appearing twice in a product are to be summed over. Dirac indices are suppressed throughout this work. Chebyshev coefficients are usually labeled by Latin indices m, n, \dots , and no summation convention is assumed.

Integrals. For momentum integrals, we use the following abbreviations:

$$\int_q \equiv \int \frac{d^d q}{(2\pi)^d}, \quad (\text{A.6})$$

$$\int d(q, u, \Omega) \equiv \int_0^\infty dq q^{d-1} \int_{-1}^1 du (1-u^2)^{\frac{d-3}{2}} \int_{S_{d-2}} d\Omega, \quad (\text{A.7})$$

$$\int d(q, u) \equiv \int_0^\infty dq q^{d-1} \int_{-1}^1 du (1-u^2)^{\frac{d-3}{2}}. \quad (\text{A.8})$$

Moreover, we define the following related constants:

- surface of the d -dimensional unit sphere (in \mathbb{R}^{d+1}):

$$\sigma_d := \frac{2\pi^{(d+1)/2}}{\Gamma\left(\frac{d+1}{2}\right)}; \quad (\text{A.9})$$

- angular contributions of the d -dimensional momentum integral:

$$v_d := \frac{1}{4} \frac{\sigma_{d-1}}{(2\pi)^d} = \frac{1}{2^{d+1} \pi^{d/2} \Gamma\left(\frac{d}{2}\right)}. \quad (\text{A.10})$$

Mandelstam variables. The Mandelstam variables are defined as

$$\mathfrak{s} = (p_1 + p_2)^2 = (p_3 + p_4)^2, \quad \mathfrak{t} = (p_1 + p_4)^2 = (p_2 + p_3)^2, \quad \mathfrak{u} = (p_1 + p_3)^2 = (p_2 + p_4)^2. \quad (\text{A.11})$$

Metric. We work exclusively in Euclidean space with metric $(\delta_{\mu\nu}) = \text{diag}(1, \dots, 1)$.

Momentum vectors and configurations. External momenta of propagators and four-fermion interactions are usually denoted by p and p_1, \dots, p_4 , respectively. In general, $p_1 \equiv -p_2 - p_3 - p_4$, and all momenta are measured as flowing into the vertex. Loop momenta are usually labeled q .

We use four standard momentum configurations to close the definition of diagram functionals in the \mathfrak{s} -channel approximation. In all of them, $p_1^2 = \dots = p_4^2 = \frac{\mathfrak{s}}{2+2\cos\angle(p_3, p_4)}$. Apart from this, they are characterized by

- parallel: $\mathfrak{t} = 0$, $\mathfrak{u} = 0$, *i.e.* $p_1, p_2 \uparrow\downarrow p_3, p_4$;
- \mathfrak{t} -favored orthogonal: $\mathfrak{t} = \mathfrak{s}$, $\mathfrak{u} = 0$, *i.e.* $p_1 \cdot p_2 = p_3 \cdot p_4 = p_1 \cdot p_4 = p_2 \cdot p_3 = 0$ and $p_1 = -p_3$, $p_2 = -p_4$;
- \mathfrak{u} -favored orthogonal: $\mathfrak{t} = 0$, $\mathfrak{u} = \mathfrak{s}$, *i.e.* $p_1 \cdot p_2 = p_3 \cdot p_4 = p_1 \cdot p_3 = p_2 \cdot p_4 = 0$ and $p_1 = -p_4$, $p_2 = -p_3$;
- symmetric: $\mathfrak{s} = \mathfrak{t} = \mathfrak{u}$, *i.e.* $p_i \cdot p_j = -\frac{1}{3} \sqrt{p_i^2 p_j^2} = -\frac{\mathfrak{s}}{4}$.

These configurations are depicted in Fig. 7.

Pauli matrices. The Pauli matrices are given by

$$\sigma_1 = \begin{pmatrix} 0 & 1 \\ 1 & 0 \end{pmatrix}, \quad \sigma_2 = \begin{pmatrix} 0 & -i \\ i & 0 \end{pmatrix}, \quad \sigma_3 = \begin{pmatrix} 1 & 0 \\ 0 & -1 \end{pmatrix}. \quad (\text{A.12})$$

Propagators. For the regularized inverse bosonic propagator, we define

$$B(p^2) := p^2 Z(p^2) \left[1 + r_k^{(B)}(p^2) \right] + \bar{m}^2. \quad (\text{A.13})$$

Similarly, we define the denominator of the regularized (massless) fermionic propagator,

$$F(p^2) := p^2 Z(p^2) \left[1 + r_k^{(F)}(p^2) \right]. \quad (\text{A.14})$$

Note that the regularized fermionic propagator is then $\not{p}/F(p^2)$.

Threshold functions. For the threshold functions, *i.e.* the regularized loop integrals in the point-like limit, we follow the conventions of Refs. [32, 94].

Threshold kernel. The fermionic one-loop threshold kernel, which is the momentum dependent generalization of the threshold function $\ell_1^{(F)}(0; \eta)$, is defined by

$$\frac{a_1}{a_2} K_1^{(F)}(p, q; \eta) := \frac{1}{\tilde{N}} \left(\frac{(a_1 + a_2)q^2 + a_1(q \cdot p) - a_2 \frac{(q \cdot p)^2}{p^2}}{q^2(q + p)^2} \right) \frac{\partial_t r_1(q^2) - \eta(q^2)r_1(q^2)}{[1 + r_1(q^2)]^2 [1 + r_1([q + p]^2)]} \quad (\text{A.15})$$

The relation to the threshold function is $\int_q \frac{1}{0} K_1^{(F)}(0, q; \eta) = \frac{2v_d}{\tilde{N}} \ell_1^{(F)}(0; \eta)$. In the single-channel approximations, we define the kernel as

$$\frac{a_1}{a_2} K(\mathfrak{m}, q, u; \eta) := \frac{2}{\tilde{N}(2\pi)^d} \frac{(a_1 + a_2)q^2 + a_1 q \sqrt{\mathfrak{m}} u - a_2 a^2 u}{q^2(q^2 + \mathfrak{m} + 2q\sqrt{\mathfrak{m}} u)} \frac{\partial_t r_1(q^2) - \eta(q^2)r_1(q^2)}{[1 + r_1(q^2)]^2 [1 + r_1(q^2 + \mathfrak{m} + 2q\sqrt{\mathfrak{m}} u)]}, \quad (\text{A.16})$$

with the z -component of the loop momentum q pointing along the momentum transfer vector p and absorbing an additional factor of $2/(2\pi)^d$ compared to $K_1^{(F)}$. In this expression, \mathfrak{m} stands for any of the Mandelstam variables \mathfrak{s} , \mathfrak{t} , \mathfrak{u} . The integrated threshold kernel is given by

$$\frac{a_1}{a_2} K(\mathfrak{m}) := \sigma_{d-2} \int d(q, u) \frac{a_1}{a_2} K(\mathfrak{m}, q, u; 0). \quad (\text{A.17})$$

Units. We choose natural units with $\hbar = c = 1$. All quantities are measured in dimensions of mass/energy/momentum.

B Computational details

In this appendix, we will gather technical details of the calculations of flow equations and spectra carried out in Sections 3 and 4. Section B.1 is a collection of some required properties of the gamma matrices, Section B.2 contains integral identities used to project out those components from the right-hand side of the Wetterich equation which are present in the chosen truncations. In Sections B.3 and B.4 we will close the gaps in the derivation of flow equations and anomalous dimension functions between the general considerations of Section 2 and the specific models of the subsequent sections. Details of the computation of fixed points and spectra in the Gross-Neveu model (Section 3) and the Gross-Neveu-Thirring model (Section 4) will be given in Sections B.5 and B.6.

B.1 Gamma matrices

Clifford algebra. The defining relation for the Dirac space matrices $\gamma_\mu \in \mathbb{C}^{d_\gamma \times d_\gamma}$ ($\mu = 1, \dots, d$) is

$$\{\gamma_\mu, \gamma_\nu\} = 2\delta_{\mu\nu}, \quad (\text{B.1})$$

ensuring that they generate a Clifford algebra. Since this requires the existence of d linearly independent, mutually anticommuting matrices, the minimum dimension d_γ of the γ matrices depends on the dimension of spacetime. Of course, there may be physical reasons to use a representation with d_γ larger than the minimum value as for the case of graphene and cuprate superconductors discussed in the main text. We call such representations *reducible* as opposed to the *irreducible* representations with minimal d_γ .

In $d = 3$ dimensions, we need $d_\gamma \geq 2$. An irreducible representation, which we also use in Section 4, is given by the Pauli matrices (4.3). Four-dimensional reducible representations are straightforwardly obtained from irreducible representations in $d = 4$ by simply omitting one of the corresponding γ matrices. In the following, we will collect a few identities that proved useful when deriving flow equations and simplifying the products of Dirac space matrices in Eq. (2.21). A more comprehensive list of properties of γ matrices may be found in Appendix E of Ref. [128].

Arbitrary representation. The following relations follow directly from the Clifford algebra (B.1) and are therefore independent of the representation. We begin with the trace identities:

$$\text{tr}(\gamma_\mu \gamma_\nu) = d_\gamma \delta_{\mu\nu}, \quad (\text{B.2a})$$

$$\text{tr}(\gamma_\mu \gamma_\nu \gamma_\rho \gamma_\sigma) = d_\gamma (\delta_{\mu\nu} \delta_{\rho\sigma} - \delta_{\mu\rho} \delta_{\nu\sigma} + \delta_{\mu\sigma} \delta_{\nu\rho}). \quad (\text{B.2b})$$

In *even* spacetime dimensions, the trace of any odd number of γ matrices vanishes. However, this does not hold in *odd* dimensions. We will provide explicit expressions for required traces in the irreducible representation in $d = 3$ in the next paragraph. For products involving a contraction of a certain index, we find

$$\gamma_\alpha \gamma_\mu \gamma_\alpha = -(d-2)\gamma_\mu, \quad (\text{B.3a})$$

$$\gamma_\alpha \gamma_\mu \gamma_\nu \gamma_\alpha = 4\delta_{\mu\nu} + (d-4)\gamma_\mu \gamma_\nu, \quad (\text{B.3b})$$

$$\gamma_\alpha \gamma_\mu \gamma_\nu \gamma_\rho \gamma_\alpha = 4(-\delta_{\mu\nu} \gamma_\rho + \delta_{\mu\rho} \gamma_\nu - \delta_{\nu\rho} \gamma_\mu) - (d-6)\gamma_\mu \gamma_\nu \gamma_\rho. \quad (\text{B.3c})$$

Irreducible representation in $d=3$. In the irreducible representation in $d = 3$ dimensions in terms of the Pauli matrices (*i.e.* $d_\gamma = 2$), any product of $\gamma_\mu = \sigma_\mu$ matrices can be reduced to first order in σ_μ by means of

$$\sigma_\mu \sigma_\nu = \delta_{\mu\nu} + i\varepsilon_{\mu\nu\rho} \sigma_\rho. \quad (\text{B.4})$$

For instance, we have

$$\sigma_\mu \sigma_\nu \sigma_\rho = i\varepsilon_{\mu\nu\rho} + \sigma_\mu \delta_{\nu\rho} - \sigma_\nu \delta_{\rho\mu} + \sigma_\rho \delta_{\mu\nu} \quad (\text{B.5a})$$

For the trace of three Pauli matrices, we thus obtain

$$\text{tr}(\sigma_\mu \sigma_\nu \sigma_\rho) = 2i\varepsilon_{\mu\nu\rho}. \quad (\text{B.6})$$

B.2 Loop integrals with spherical symmetry

In order to arrive at the flow equations for the couplings, we have to project the field operators on the right-hand side of Eq. (2.19) onto the vertices present in our ansatz (2.9) and subsequently match the left- and right-hand sides of the Wetterich equation (1.17). Thereby we will frequently encounter integrals of the form

$$\int_q f(q^2, q \cdot p) q_\mu (q + p)_\nu ,$$

where p is a momentum vector and f an arbitrary function depending on the norm of the loop momentum as well as the angle between q and p . Speaking in terms of the diagrams in Fig. 4, the vectors q and p will correspond to the loop momentum and the momentum transfer, respectively. Let us define the transversal and longitudinal projectors of the vector p ,

$$\pi_{\mu\nu}^L = \frac{p_\mu p_\nu}{p^2} \quad \text{and} \quad \pi_{\mu\nu}^T = \delta_{\mu\nu} - \frac{p_\mu p_\nu}{p^2} . \quad (\text{B.7})$$

We can then decompose any vector into parallel and orthogonal components with respect to p . For the first type of integrals, we obtain

$$\int_q f(q^2, q \cdot p) q_\mu = \int_q f(q^2, q \cdot p) (\pi_{\mu\nu}^L + \pi_{\mu\nu}^T) q_\nu = \frac{p_\mu}{p^2} \int_q f(q^2, q \cdot p) (q \cdot p) , \quad (\text{B.8})$$

where the transversal component drops out because the integral needs to be invariant under Lorentz transformations that leave the external momentum unaffected, *i.e.* rotations around p . In particular,

$$\int_q f(q^2) (q \cdot p) q_\mu = \frac{p_\mu}{p^2} \int_q f(q^2) (q \cdot p)^2 = \frac{\sigma_{d-1}}{d} p_\mu \int_0^\infty dq q^{d+1} f(q^2) . \quad (\text{B.9})$$

For the second type of integrals needed, we make an ansatz of the form

$$\int_q f(q^2, q \cdot p) q_\mu q_\nu = \pi_{\mu\nu}^L \int_q f(q^2, q \cdot p) a^L(q^2, p^2, q \cdot p) + \pi_{\mu\nu}^T \int_q f(q^2, q \cdot p) a^T(q^2, p^2, q \cdot p) ,$$

which is justified by the requirement of Lorentz invariance again, whereby the result must be a rank-2 tensor parametrized by the external momentum vector p . Acting with the longitudinal and transversal projectors on this equation gives us consistency equations that determine the coefficient functions a^L and a^T , leading to

$$\int_q f(q^2, q \cdot p) q_\mu q_\nu = \pi_{\mu\nu}^L \int_q f(q^2, q \cdot p) \frac{(q \cdot p)^2}{p^2} + \pi_{\mu\nu}^T \frac{1}{d-1} \int_q f(q^2, q \cdot p) \left[q^2 - \frac{(q \cdot p)^2}{p^2} \right] . \quad (\text{B.10})$$

Collecting these two integral relations, we arrive at the useful result

$$\begin{aligned} \int_q f(q^2, q \cdot p) q_\mu (q + p)_\nu &= \frac{\delta_{\mu\nu}}{d-1} \int_q f(q^2, q \cdot p) \left[q^2 - \frac{(q \cdot p)^2}{p^2} \right] \\ &\quad + \frac{p_\mu p_\nu}{p^2} \int_q f(q^2, q \cdot p) \left[\frac{d}{d-1} \frac{(q \cdot p)^2}{p^2} + q \cdot p - \frac{1}{d-1} q^2 \right] . \end{aligned} \quad (\text{B.11})$$

B.3 Flow equations

Let us now take a closer look at the flow equations for the Gross-Neveu and Thirring vertices. Our effective action thus comprises the couplings g_{GN} and g_{Th} as in Eq. (4.4), but we do not restrict to a particular representation of the Clifford algebra yet. According to the general analysis of Section 2.2, the diagrams to be considered include either two Gross-Neveu vertices, or two Thirring vertices, or one Gross-Neveu and one Thirring vertex.

Gross-Neveu vertices. We begin with diagrams featuring two Gross-Neveu interactions, *i.e.* $g_A = g_B = g_{\text{GN}}$ and $\mathcal{O}_A = \mathcal{O}_B = \mathbf{1}$ in (2.21). In the $\mathfrak{s}2$ -channel, we obtain a vertex of the Gross-Neveu type with a weight of

$$-N_f \text{tr}(\not{q}' \not{q}) = -(q \cdot q') N_f d_\gamma. \quad (\text{B.12})$$

According to relation (2.25), this prompts the a_1 -parametrized type of the $\mathfrak{s}2$ -diagram and thus contributes a term $-\tilde{B}_0^{\mathfrak{s}2}[g_{\text{GN}}, g_{\text{GN}}]$ to the flow of g_{GN} . Notice that we do not denote the η dependence of the diagram functional explicitly. The fermion bilinears in the $\mathfrak{s}1$ -channel are

$$\bar{\psi} \psi \bar{\psi} \not{q}' \not{q} \psi = q \cdot q' \bar{\psi} \psi \bar{\psi} \psi + q'_\mu q_\nu \bar{\psi} \psi \bar{\psi} \gamma_{\mu\nu} \psi \quad (\text{B.13})$$

with $\gamma_{\mu\nu} = \frac{1}{2} [\gamma_\mu, \gamma_\nu]$. Here we omitted the momentum dependence of the spinor fields, too, to keep the notation slim; their order is understood as given in Eq. (2.21). A vertex of the second type is not considered in our ansatz (2.9), but the first one will contribute to the flow of g_{GN} with an overall ${}^2 B_0^{\mathfrak{s}1}[g_{\text{GN}}, g_{\text{GN}}]$ diagram. The t -channel bilinear structure is

$$\bar{\psi} \not{q}' \psi \bar{\psi} \not{q} \psi = (q + p_2 + p_3)_\mu q_\nu \bar{\psi} \gamma_\mu \psi \bar{\psi} \gamma_\nu \psi. \quad (\text{B.14})$$

These do not contribute to the flow of g_{GN} , but give potential contributions to the Thirring vertex. To find them, we need to pick out those terms for which the loop integral is proportional to $\delta_{\mu\nu}$. Consulting Eq. (B.11) and comparing with Eq. (2.25), we see that this gives an a_2 -parametrized contribution of the t -diagram with a weight of $\tilde{d} = \frac{1}{d-1}$, *i.e.* the flow of g_{Th} receives a term ${}^0 \tilde{B}_d^t[g_{\text{GN}}, g_{\text{GN}}]$. The structure in the u -channel is identical except for an extra minus sign, such that there is a term $-{}^0 \tilde{B}_d^u[g_{\text{GN}}, g_{\text{GN}}]$ added to the flow of g_{Th} .

In the case of the pure Gross-Neveu model as studied in Section 3, this already completes the analysis for the one coupling present. Including the appropriate scaling term, the corresponding flow equation is

$$\partial_t g_{\text{GN}} = \left[d - 2 + 2\eta^{(4)} \right] g_{\text{GN}} + \sum_{j=1}^4 p_j \cdot \nabla_{p_j} g_{\text{GN}} - \tilde{B}_0^{\mathfrak{s}2}[g_{\text{GN}}, g_{\text{GN}}] + {}^2 B_0^{\mathfrak{s}1}[g_{\text{GN}}, g_{\text{GN}}]. \quad (\text{B.15})$$

For the remaining analysis, we restrict our computations to $d = 3$ dimensions and the irreducible representation of the Clifford algebra in terms of Pauli matrices.

Mixed vertices. Let us next turn to diagrams involving one Gross-Neveu and one Thirring interaction. We immediately see that the $\mathfrak{s}2$ -channel is not called by mixed diagrams because it would lead to mixed vertices, which are not incorporated in the ansatz (2.9). We begin our study of the other channels with $g_A = g_{\text{GN}}$, $\mathcal{O}_A = \mathbf{1}$ and $g_B = g_{\text{Th}}$, $\mathcal{O}_B = \gamma_\mu$. The first $\mathfrak{s}1$ -type, line 2 of the integral in (2.21), features bilinears of the form

$$\bar{\psi} \psi \bar{\psi} \sigma_\alpha \not{q}' \not{q} \sigma_\alpha \psi = q'_\mu q_\nu \bar{\psi} \psi \bar{\psi} \sigma_\alpha [\delta_{\mu\nu} + i q'_\mu q_\nu \varepsilon_{\mu\nu\beta} \sigma_\beta] \sigma_\alpha \psi = q'_\mu q_\nu \bar{\psi} \psi \bar{\psi} [3\delta_{\mu\nu} - i \varepsilon_{\mu\nu\rho} \sigma_\rho] \psi. \quad (\text{B.16})$$

Disallowing mixed vertices once again, we thus end up with a contribution ${}^3 B_0^{\mathfrak{s}1}[g_{\text{GN}}, g_{\text{Th}}]$ to the flow of g_{GN} . In the second $\mathfrak{s}1$ -type, line 3 of the integral in (2.21), the bilinear structure is

$$\bar{\psi} \sigma_\alpha \psi \bar{\psi} \not{q}' \sigma_\alpha \not{q} \psi = q'_\mu q_\nu \bar{\psi} \sigma_\alpha \psi \bar{\psi} [\sigma_\mu \delta_{\alpha\nu} + \sigma_\nu \delta_{\mu\alpha} - \sigma_\alpha \delta_{\mu\nu} + i \varepsilon_{\mu\alpha\nu} \sigma_\nu] \psi. \quad (\text{B.17})$$

There is no input to the flow of g_{GN} , but the Thirring coupling receives contributions of the form ${}_{a_2}^{a_1} B_0^{\mathfrak{s}1}[g_{\text{Th}}, g_{\text{GN}}]$ in two ways: The term proportional to $\delta_{\mu\nu}$ gives $a_1 = -1$, whereas the remaining to δ -terms lead to $a_2 = \frac{2}{d-1} = 1$. Hence it follows a term $-{}_{-1}^1 B_0^{\mathfrak{s}1}[g_{\text{Th}}, g_{\text{GN}}]$ for the flow of g_{Th} . In the t -channel, the situation of bilinears is

$$\bar{\psi} \not{q}' \sigma_\alpha \psi \bar{\psi} \sigma_\alpha \not{q} \psi = q'_\mu q_\nu \bar{\psi} \sigma_\mu \sigma_\alpha \psi \bar{\psi} \sigma_\alpha \sigma_\nu \psi = q'_\mu q_\nu \bar{\psi} [\delta_{\mu\alpha} + i \varepsilon_{\mu\alpha\beta} \sigma_\beta] \psi \bar{\psi} [\delta_{\alpha\nu} + i \varepsilon_{\alpha\nu\gamma} \sigma_\gamma] \psi. \quad (\text{B.18})$$

Contributions to the flow of g_{GN} arise from the term proportional to $\delta\delta$, namely ${}^1 B_0^t[g_{\text{GN}}, g_{\text{Th}}]$. Furthermore, the term proportional to $\varepsilon\varepsilon$ will contribute to the flow of g_{Th} by means of ${}_{a_2}^{a_1} B_0^t$ diagrams. To quantify it, we use that

$$\varepsilon_{\mu\alpha\beta} \varepsilon_{\alpha\nu\gamma} = -\delta_{\mu\nu} \delta_{\beta\gamma} + \delta_{\mu\gamma} \delta_{\beta\nu}. \quad (\text{B.19})$$

The first term leads to $a_1 = 1$, while the second term gives $a_2 = -\frac{1}{d-1} = -\frac{1}{2}$, with the extra minus sign originating from the factor i^2 . The overall contribution is thus ${}_{-1/2}^1 B^t[g_{GN}, g_{Th}]$. Finally, the bilinears in the u -channel are again very similar to the t -channel ones, namely

$$\bar{\psi} q' \sigma_\alpha \psi \bar{\psi} \sigma_\alpha q \psi = q'_\mu q_\nu \bar{\psi} \sigma_\alpha \sigma_\mu \psi \bar{\psi} \sigma_\alpha \sigma_\nu \psi \psi. \quad (B.20)$$

Apparently, we have to interchange $\mu \leftrightarrow \alpha$ in the Kronecker and Levi-Civita symbols of the first bilinear in (B.18), which does not affect the g_{GN} -flow term, but gives a negative sign for the g_{Th} -flow term. Together with the additional minus for the u -channel contributions from (2.21), we obtain a term ${}_{-0}^1 B^u[g_{GN}, g_{Th}]$ for the flow of g_{GN} and a term ${}_{-1/2}^1 B^u[g_{GN}, g_{Th}]$ for the flow of g_{Th} .

There remain the terms with the indices A and B and thus the roles of the Gross-Neveu and Thirring couplings interchanged, *i.e.* $g_A = g_{Th}$, $\mathcal{O}_A = \gamma_\mu$ and $g_B = g_{GN}$, $\mathcal{O}_B = \mathbf{1}$. The effect is that we obtain the same diagrams as above with $g_{GN} \longleftrightarrow g_{Th}$. For the $\mathfrak{s}1$ -channel, this is immediately clear because the terms are obviously symmetric under the exchange of couplings. In the t - and u -channels, we have to swap the indices $\mu \leftrightarrow \alpha$ in the first and $\nu \leftrightarrow \alpha$ in the second fermion bilinear in Eqs. (B.18) and (B.20). As this leaves the products $\delta\delta$ and $\varepsilon\varepsilon$ invariant, we receive indeed the same weights for the diagrams as before with $g_{GN} \longleftrightarrow g_{Th}$.

Thirring vertices. Finally, we will address the diagrams involving two Thirring vertices such that $g_A = g_{Th}$, $\mathcal{O}_A = \gamma_\mu$ and $g_B = g_{Th}$, $\mathcal{O}_B = \gamma_\nu$. The $\mathfrak{s}2$ -channel contributes a term to the flow of g_{Th} with weight

$$-N_f \text{tr}(q' \sigma_\alpha q \sigma_\beta) = -q'_\mu q_\nu N_f d_\gamma (\delta_{\mu\alpha} \delta_{\nu\beta} - \delta_{\mu\nu} \delta_{\alpha\beta} + \delta_{\mu\beta} \delta_{\nu\alpha}). \quad (B.21)$$

The term proportional to $\delta_{\mu\nu} \delta_{\alpha\beta}$ leads to $a_1 = \tilde{N}$, while the other two terms give $a_2 = -\tilde{N} \frac{2}{d-1} = -\tilde{N}$. Together, the flow of g_{Th} receives a contribution ${}_{-\tilde{N}}^{\tilde{N}} B^{\mathfrak{s}2}[g_{Th}, g_{Th}]$. In the $\mathfrak{s}1$ -channel, we encounter bilinears of the form

$$\begin{aligned} \bar{\psi} \sigma_\alpha \psi \bar{\psi} \sigma_\beta q' \sigma_\alpha q \sigma_\beta \psi &= q'_\mu q_\nu \bar{\psi} \sigma_\alpha \psi \bar{\psi} \sigma_\beta \sigma_\mu \sigma_\alpha \sigma_\nu \sigma_\beta \psi \\ &= q'_\mu q_\nu \bar{\psi} \sigma_\alpha \psi \bar{\psi} [\sigma_\alpha \delta_{\mu\nu} - \sigma_\mu \delta_{\alpha\nu} - \sigma_\nu \delta_{\alpha\mu} + 3i\varepsilon_{\mu\alpha\nu}] \psi. \end{aligned} \quad (B.22)$$

The term proportional to $\delta_{\mu\nu}$ gives $a_1 = 1$, the other two δ terms yield $a_2 = -\frac{2}{d-1} = -1$, and the ε term does not contribute. Consequently, we obtain a diagram ${}_{-2}^2 B^{\mathfrak{s}1}[g_{Th}, g_{Th}]$ for the flow of g_{Th} , the factor of 2 arising from the fact that there are two $\mathfrak{s}1$ -channel terms in Eq. (2.21). In the t -channel, the spinor bilinears are

$$\begin{aligned} \bar{\psi} \sigma_\alpha q' \sigma_\beta \psi \bar{\psi} \sigma_\beta q \sigma_\alpha \psi &= q'_\mu q_\nu \bar{\psi} \sigma_\alpha \sigma_\mu \sigma_\beta \psi \bar{\psi} \sigma_\beta \sigma_\nu \sigma_\alpha \psi \\ &= q'_\mu q_\nu \bar{\psi} [\sigma_\alpha \delta_{\mu\beta} + \sigma_\beta \delta_{\mu\alpha} - \sigma_\mu \delta_{\alpha\beta} + i\varepsilon_{\alpha\mu\beta}] \psi \bar{\psi} [\sigma_\beta \delta_{\nu\alpha} + \sigma_\alpha \delta_{\nu\beta} - \sigma_\nu \delta_{\alpha\beta} + i\varepsilon_{\beta\nu\alpha}] \psi. \end{aligned} \quad (B.23)$$

Let us refer to the terms in the left and right square brackets by L1 through L4 and R1 through R4, respectively, and analyze the 16 possible products. Our first observation is that the terms where either $L4$ or $R4$ is multiplied with any of the first three terms on the opposite side will not contribute because they lead to mixed vertices. Of the remaining ten terms, the only one entering the flow of the Gross-Neveu coupling is the L4R4 term. Since $\varepsilon_{\alpha\mu\beta}\varepsilon_{\beta\nu\alpha} = (1-d)\delta_{\mu\nu}$, the resulting diagram is ${}_{-0}^2 B^t[g_{Th}, g_{Th}]$. The nine terms left all contribute to the flow of the Thirring coupling. The ones with an a_1 -parametrized contribution are L1R2 and L2R1, *i.e.* $a_1 = 2$. The terms L1R1 and L2R2 have a positive sign while L1R3, L2R3, L3R1, and L3R2 are negative. The term L3R3 is special because it carries a relative weight of $d = 3$ with respect to the other six due to the trace of the Kronecker delta. All in all, the relevant prefactor $a_2 = \frac{2-4+d}{d-1} = \frac{1}{2}$. Hence the contribution to the flow of g_{Th} is ${}_{-1/2}^2 B^t[g_{Th}, g_{Th}]$.

In the u -channel, the structure is again very similar to the t -channel. The fermion bilinears are

$$\bar{\psi} \sigma_\beta q' \sigma_\alpha \psi \bar{\psi} \sigma_\beta q \sigma_\alpha \psi = q'_\mu q_\nu \bar{\psi} \sigma_\beta \sigma_\mu \sigma_\alpha \psi \bar{\psi} \sigma_\beta \sigma_\nu \sigma_\alpha \psi. \quad (B.24)$$

Comparing to (B.23), we see that we have to exchange $\alpha \leftrightarrow \beta$ in the left bracket. This leaves the $\delta\delta$ contributions unchanged and introduces a negative sign for the $\varepsilon\varepsilon$ contribution. Together with the extra minus from Eq. (2.21), we therefore obtain a term ${}_{-0}^2 B^u[g_{Th}, g_{Th}]$ for the flow of g_{GN} and a term ${}_{-1/2}^2 B^t[g_{Th}, g_{Th}]$ for the flow of g_{Th} .

This completes the analysis of the flow equations for the Gross-Neveu-Thirring model. Collecting all contributions, we arrive precisely at the results (4.5a) and (4.5b).

B.4 Anomalous dimension function

A general derivation of the FRG relation for the anomalous dimension of fermion interacting via four-particle vertices was presented in Section 2.3, culminating in Eq. (2.36). Here we will calculate the precise contributions from the interaction vertices considered in Sections 3 and 4.

Gross-Neveu vertex. For the Gross-Neveu interaction, we have $\mathcal{O}_A = \mathbf{1}$ in Eq. (2.36). Hence the first term, proportional to N_f and corresponding to the second diagram in (2.37b), does not contribute because both traces vanish. The prefactor of the second term reduces to

$$\text{tr}(\not{p} \not{q}) = d_\gamma(p \cdot q), \quad (\text{B.25})$$

such that the Gross-Neveu interaction contributes to the anomalous dimension function with the diagram $\Sigma^1[g_{\text{GN}}]$ as stated in Eq. (3.5).

Thirring vertex. For the Thirring vertex, we set $\mathcal{O}_A = \gamma_\alpha$ in Eq. (2.36). The traces appearing in the first term are of the form

$$\text{tr}(\gamma_\mu \gamma_\alpha) = d_\gamma \delta_{\mu\alpha}. \quad (\text{B.26})$$

Thus the contribution here is $\tilde{N} \Sigma^2[g_{\text{Th}}](p)$. For the second term, we simplify

$$\text{tr}(\gamma_\mu \gamma_\alpha \gamma_\nu \gamma_\alpha) = (2-d) d_\gamma \delta_{\mu\nu}. \quad (\text{B.27})$$

Therefore, the anomalous dimension receives another contribution from the Thirring vertex given by $(2-d) \Sigma^1[g_{\text{Th}}]$. In $d = 3$, the anomalous dimension then satisfies the relation (4.6).

B.5 Gross-Neveu model

Diagram functionals. The diagram functionals were already defined in Sections 3 and 4. For convenience, we will introduce a slightly more general notation here, beginning with the threshold kernel (3.20). We add a factor α in front of the regulator derivative, allowing us to switch this term on and off deliberately:

$$\frac{a_1}{a_2} K_\alpha(\mathfrak{s}, q, u; \eta) := \frac{1}{(2\pi)^d} \left[\frac{(a_1 + a_2)q^2 + a_1 q \sqrt{\mathfrak{s}} u - a_2 q^2 u^2}{q^2(q^2 + \mathfrak{s} + 2q\sqrt{\mathfrak{s}}u)} \right] \frac{\alpha \partial_t r_1(q^2) - \eta(q^2) r_1(q^2)}{[1 + r_1(q^2)]^2 [1 + r_1(q^2 + \mathfrak{s} + 2q\sqrt{\mathfrak{s}}u)]}. \quad (\text{B.28})$$

The original definition is thus given by $\alpha = 1$. Regarding the diagram functionals, we substitute this generalized kernel. In the \mathfrak{s} -channel approximation, we then define the following diagram functionals:

$$\frac{a_1}{a_2} B^{\mathfrak{s}2}[g_1, g_2; \eta, \alpha](\mathfrak{s}) := \frac{2}{\tilde{N}} g_1(\mathfrak{s}) g_2(\mathfrak{s}) \sigma_{d-2} \int d(q, u) \frac{a_1}{a_2} K_\alpha(\mathfrak{s}, q, u; \eta), \quad (\text{B.29a})$$

$$\frac{a_1}{a_2} B^{\mathfrak{s}1}[g_1, g_2; \eta, \alpha](\mathfrak{s}) := \frac{1}{\tilde{N}} g_1(\mathfrak{s}) \int d(q, u, \Omega) \frac{a_1}{a_2} K_\alpha(\mathfrak{s}, q, u; \eta) [g_2([q + p_3]^2) + g_2([q + p_4]^2)], \quad (\text{B.29b})$$

$$\begin{aligned} \frac{a_1}{a_2} B^{\mathfrak{t}}[g_1, g_2; \eta, \alpha](\mathfrak{s}) := & \frac{1}{\tilde{N}} \int d(q, u, \Omega) \frac{a_1}{a_2} K_\alpha(\mathfrak{t}, q, u; \eta) \\ & \times [g_1([q - p_1]^2) g_2([q + p_2]^2) + g_1([q - p_4]^2) g_2([q + p_3]^2)], \end{aligned} \quad (\text{B.29c})$$

$$\begin{aligned} \frac{a_1}{a_2} B^{\mathfrak{u}}[g_1, g_2; \eta, \alpha](\mathfrak{s}) := & \frac{1}{\tilde{N}} \int d(q, u, \Omega) \frac{a_1}{a_2} K_\alpha(\mathfrak{u}, q, u; \eta) \\ & \times [g_1([q - p_1]^2) g_2([q + p_2]^2) + g_1([q - p_3]^2) g_2([q + p_4]^2)], \end{aligned} \quad (\text{B.29d})$$

where a fixed momentum configuration is understood. For the relevant self-energy diagram, we denote

$$\Sigma^1[g; \eta, \alpha](p^2) := - \int d(q, u) \frac{\sigma_{d-2}}{\tilde{N}(2\pi)^d} \left(\frac{u}{\sqrt{p^2} q} \right) \frac{\alpha \partial_t r_1(q^2) - \eta(q^2) r_1(q^2)}{[1 + r_1(q^2)]^2} g(q^2 + p^2 + 2q\sqrt{p^2}u) \quad (\text{B.30})$$

in a similar way. Implementing the diagram functionals in this form for arbitrary g - and η -arguments is a convenient starting point for calculations of fixed point equations and spectra. In fact, all loop integrals encountered in the models of this thesis can be expressed in terms of these five functionals.

Fixed point. The defining equations for the coupling and anomalous dimension functions are (3.25) and (3.26). These lead to the residual functionals

$$\rho^g[g, \eta](\mathfrak{s}) := \left[1 + 2\eta \left(\frac{\mathfrak{s}}{2 + 2c_{34}} \right) \right] g(\mathfrak{s}) + 2\mathfrak{s} g'(\mathfrak{s}) - \tilde{N} B^{\mathfrak{s}2}[g, g; \eta, 1](\mathfrak{s}) + 2B^{\mathfrak{s}1}[g, g; \eta, 1](\mathfrak{s}), \quad (\text{B.31a})$$

$$\rho^\eta[g, \eta](p^2) := \eta(p^2) - \Sigma^1[g; \eta, 1](p^2), \quad (\text{B.31b})$$

where $c_{34} = \cos \sphericalangle(p_3, p_4)$ and $a_1 = 1, a_2 = 0$ are suppressed. By plugging in the Chebyshev ansatz (3.47) and evaluating on the collocation grids $\{s_m\}$ and $\{p_m^2\}$, we obtain the residual vector (3.51), $\rho(\mathbf{g}, \boldsymbol{\eta}) = (\rho_1^g, \dots, \rho_{n_{\max}}^g, \rho_1^\eta, \dots, \rho_{n_{\max}}^\eta)$ with

$$\rho_m^g(\mathbf{g}, \boldsymbol{\eta}) := \rho^g \left[\sum g_n P_n, \sum \eta_n P_n \right] (\mathfrak{s}_m), \quad (\text{B.32a})$$

$$\rho_m^\eta(\mathbf{g}, \boldsymbol{\eta}) := \rho^\eta \left[\sum g_n P_n, \sum \eta_n P_n \right] (p_m^2) \quad (\text{B.32b})$$

for the Chebyshev coefficients $\mathbf{g} = (g_n)$, $\boldsymbol{\eta} = (\eta_n)$. To compute the corresponding Jacobian, we first evaluate derivatives of the diagram functionals. Denoting $\delta_y(x) := \delta(x - y)$, we obtain

$$\frac{\delta B^{\mathfrak{m}}[g_1, g_2; \eta, \alpha](\mathfrak{s})}{\delta g_1(\mathfrak{s}')} = B^{\mathfrak{m}}[\delta_{s'}, g_2; \eta, \alpha](\mathfrak{s}), \quad (\text{B.33})$$

$$\frac{\delta B^{\mathfrak{m}}[g_1, g_2; \eta, \alpha](\mathfrak{s})}{\delta g_2(\mathfrak{s}')} = B^{\mathfrak{m}}[g_1, \delta_{s'}; \eta, \alpha](\mathfrak{s}), \quad \frac{\delta B^{\mathfrak{m}}[g_1, g_2; \eta, \alpha](\mathfrak{s})}{\delta \eta(p'^2)} = B^{\mathfrak{m}}[g_1, g_2; \delta_{p'^2}, 0](\mathfrak{s}), \quad (\text{B.34})$$

$$\frac{\delta \Sigma^1[g; \eta, \alpha](p^2)}{\delta g(s')} = \Sigma^1[\delta_{s'}; \eta, \alpha](p^2), \quad \frac{\delta \Sigma^1[g; \eta, \alpha](p^2)}{\delta \eta(p'^2)} = \Sigma^1[g; \delta_{p'^2}, 0](p^2), \quad (\text{B.35})$$

where $\mathfrak{m} = \mathfrak{s}2, \mathfrak{s}1, \mathfrak{t}, \mathfrak{u}$ stands for any of the Mandelstam channels. The Jacobian

$$\mathbf{J} = \begin{pmatrix} \mathbf{J}^{gg} & \mathbf{J}^{g\eta} \\ \mathbf{J}^{\eta g} & \mathbf{J}^{\eta\eta} \end{pmatrix} \quad (\text{B.36})$$

thus becomes

$$J_{mn}^{gg} = \frac{\partial \rho_m^g}{\partial g_n} = \left[1 + 2\eta \left(\frac{\mathfrak{s}_m}{2 + 2c_{34}} \right) \right] P_n(\mathfrak{s}_m) + 2\mathfrak{s}_m P'_n(\mathfrak{s}_m) - 2\tilde{N} B^{\mathfrak{s}2}[g, P_n; \eta, 1](\mathfrak{s}_m) + 2B^{\mathfrak{s}1}[g, P_n; \eta, 1](\mathfrak{s}_m), \quad (\text{B.37a})$$

$$J_{mn}^{g\eta} = \frac{\partial \rho_m^g}{\partial \eta_n} = 2P_n \left(\frac{\mathfrak{s}_m}{2 + 2c_{34}} \right) g(\mathfrak{s}) - \tilde{N} B^{\mathfrak{s}2}[g, g; P_n, 0](\mathfrak{s}_m) + 2B^{\mathfrak{s}1}[g, g; P_n, 0](\mathfrak{s}_m), \quad (\text{B.37b})$$

$$J_{mn}^{\eta g} = \frac{\partial \rho_m^\eta}{\partial g_n} = -\Sigma^1[P_n; \eta, 1](p_m^2), \quad (\text{B.37c})$$

$$J_{mn}^{\eta\eta} = \frac{\partial \rho_m^\eta}{\partial \eta_n} = P_n(p_m^2) - \Sigma^1[g; P_n, 0](p_m^2). \quad (\text{B.37d})$$

Regarding the computational effort, the \mathbf{J}^{gg} component of the Jacobian is clearly the most expensive part of the calculation. First, the Chebyshev functions P_n become increasingly oscillatory with growing n , and we generally need higher precision, *i.e.* higher orders, for the coupling g than for the anomalous dimension η . Second, the diagram functionals $B^{\mathfrak{m}}$ will involve 3-dimensional integrals for all except the parallel momentum configuration, whereas the self-energy integrals Σ are always 2-dimensional. It can therefore be advantageous to compute the Jacobian numerically (*cf.* Appendix D), thereby avoiding oscillatory integrands. However, the achievable precision will in general be lower this way. In practice, a combination of both turned out to be a good compromise, where we use the numerical Jacobian for the first few iterations to reach moderate accuracy, and switch to the analytical Jacobian to fine-tune the result.

Spectrum. For the fixed maximum growth scheme, our computational method was already sketched quite detailed in Section 3.6. We simply calculate the eigenvalues of the matrix $(-\mathbf{P}^{-1}\mathbf{J}^{gg})$ with \mathbf{P} and \mathbf{J}^{gg} given in Eqs. (3.57) and (3.58), where \mathbf{J}^{gg} is a generalization of (B.37a) with additional scaling prefactor.

In the running asymptotics scheme, a_{\max} is no longer constant but replaced by $\frac{2-d-\theta}{2}$, depending on the eigenvalue θ . This renders the eigenvalue equation (3.53) nonlinear, so that we cannot use standard methods to compute spectrum and perturbations. Instead, we will use a Newton-Raphson iteration again to solve for the joint variables $(\theta; \varepsilon_0, \dots, \varepsilon_{n_{\max}^{\varepsilon}})$. The residual function for ε corresponding to Eq. (3.53) is obtained from the linearized version of the fixed point residual (B.31a),

$$\rho^{\varepsilon}(\theta; \varepsilon; \mathfrak{s}) := \theta \varepsilon(\mathfrak{s}) + \int_0^{\infty} d\mathfrak{s}' \left. \frac{\delta \rho^g[g, \eta](\mathfrak{s})}{\delta g(\mathfrak{s}')} \right|_{\substack{g=g_* \\ \eta=\eta_*}} \varepsilon(\mathfrak{s}') . \quad (\text{B.38})$$

Plugging in the ansatz (3.55) for ε and evaluating it on a collocation grid gives us $(n_{\max}^{\varepsilon} + 1)$ equations $\rho_m^{\varepsilon}(\theta; \varepsilon) := \rho^{\varepsilon}(\theta; \varepsilon; \mathfrak{s}_m) = 0$. These are supplemented by the normalization condition (3.59) for the perturbations,

$$\rho^{\theta}(\varepsilon) := 1 - \sum_{n=0}^{n_{\max}^{\varepsilon}} (-1)^n \varepsilon_n , \quad (\text{B.39})$$

such that the total residual vector is $\boldsymbol{\rho} = (\rho^{\theta}; \boldsymbol{\rho}^{\varepsilon})$. The Jacobian of the system $(\rho^{\theta}; \boldsymbol{\rho}^{\varepsilon})$ needed for the Newton-Raphson procedure takes the form

$$\mathbf{J} = \begin{pmatrix} 0 & \mathbf{J}^{\theta\varepsilon} \\ \mathbf{J}^{\varepsilon\theta} & \mathbf{J}^{\varepsilon\varepsilon} \end{pmatrix} . \quad (\text{B.40})$$

Here $J_{mn}^{\varepsilon\varepsilon} = \theta (L + \mathfrak{s}_m)^{\frac{2-d-\theta}{2}} P_n(\mathfrak{s}_m) + J_{mn}^{gg}$, where as before \mathbf{J}^{gg} is given by (3.58) with $a_{\max} = \frac{2-d-\theta}{2}$. Furthermore,

$$J_n^{\theta\rho} = \frac{\partial \rho^{\theta}(\varepsilon)}{\partial \varepsilon_n} = -(-1)^n , \quad (\text{B.41})$$

and

$$J_m^{\varepsilon\theta} = \frac{\partial \rho^{\varepsilon}[g_*, \eta_*; \varepsilon](\mathfrak{s}_m)}{\partial \theta} . \quad (\text{B.42})$$

As described in Section 3.6, we usually performed an additional ‘‘burn-in’’ step for the solver by iterating a few times with fixed θ . In this case, we omitted the first collocation point \mathfrak{s}_0 in favor of the normalization condition, so that the reduced system is given by

$$\boldsymbol{\rho}_{\text{red}} = (\rho^{\theta}; \rho_1^{\varepsilon}, \dots, \rho_{n_{\max}^{\varepsilon}}^{\varepsilon}) , \quad \mathbf{J} = \begin{pmatrix} \mathbf{J}^{\theta\varepsilon} \\ \mathbf{J}_{\text{red}}^{\varepsilon\varepsilon} \end{pmatrix} \quad (\theta \text{ fixed}) . \quad (\text{B.43})$$

Once the residual is reasonably small such that the fluctuations in the eigenvalue are expected to be small, too, we release θ and solve the full system given above.

B.6 Gross-Neveu-Thirring model

Fixed points. The fixed point residuals following from Eqs. (4.5) and (4.6) and expressed in terms of the extended diagram functionals (B.29) and (B.30) read

$$\begin{aligned} \rho^{g_{\text{GN}}}[g_{\text{GN}}, g_{\text{Th}}, \eta](\mathfrak{s}) &:= \left[1 + 2\eta \left(\frac{\mathfrak{s}}{2 + 2c_{34}} \right) \right] g_{\text{GN}}(\mathfrak{s}) + 2\mathfrak{s} g'_{\text{GN}}(\mathfrak{s}) \\ &- \tilde{N}_0 B^{\mathfrak{s}2}[g_{\text{GN}}, g_{\text{GN}}; \eta, 1](\mathfrak{s}) + {}^2_0 B^{\mathfrak{s}1}[g_{\text{GN}}, g_{\text{GN}}; \eta, 1](\mathfrak{s}) + {}^3_0 B_{\leftrightarrow}^{\mathfrak{s}1}[g_{\text{GN}}, g_{\text{Th}}; \eta, 1](\mathfrak{s}) \\ &+ {}^1_0 B_{\leftrightarrow}^{\mathfrak{t}}[g_{\text{GN}}, g_{\text{Th}}; \eta, 1](\mathfrak{s}) + {}^2_0 B^{\mathfrak{t}}[g_{\text{Th}}, g_{\text{Th}}; \eta, 1](\mathfrak{s}) \\ &- {}^1_0 B_{\leftrightarrow}^{\mathfrak{u}}[g_{\text{GN}}, g_{\text{Th}}; \eta, 1](\mathfrak{s}) + {}^2_0 B^{\mathfrak{u}}[g_{\text{Th}}, g_{\text{Th}}; \eta, 1](\mathfrak{s}) , \end{aligned} \quad (\text{B.44a})$$

$$\begin{aligned}
\rho^{g_{\text{Th}}}[g_{\text{GN}}, g_{\text{Th}}, \eta](\mathfrak{s}) &:= \left[1 + 2\eta \left(\frac{\mathfrak{s}}{2 + 2c_{34}} \right) \right] g_{\text{Th}}(\mathfrak{s}) + 2\mathfrak{s} g'_{\text{Th}}(\mathfrak{s}) + {}_{-\tilde{N}}B^{\mathfrak{s}2}[g_{\text{Th}}, g_{\text{Th}}; \eta, 1](\mathfrak{s}) \\
&\quad - {}_{-1}B_{\leftrightarrow}^{\mathfrak{s}1}[g_{\text{GN}}, g_{\text{Th}}; \eta, 1](\mathfrak{s}) + {}_{-2}B^{\mathfrak{s}1}[g_{\text{Th}}, g_{\text{Th}}; \eta, 1](\mathfrak{s}) \\
&\quad + {}_{1/2}B^{\mathfrak{t}}[g_{\text{GN}}, g_{\text{GN}}; \eta, 1](\mathfrak{s}) + {}_{-1/2}B_{\leftrightarrow}^{\mathfrak{t}}[g_{\text{GN}}, g_{\text{Th}}; \eta, 1](\mathfrak{s}) + {}_{1/2}B^{\mathfrak{t}}[g_{\text{Th}}, g_{\text{Th}}; \eta, 1](\mathfrak{s}) \\
&\quad - {}_{1/2}B^{\mathfrak{u}}[g_{\text{GN}}, g_{\text{GN}}; \eta, 1](\mathfrak{s}) + {}_{-1/2}B_{\leftrightarrow}^{\mathfrak{u}}[g_{\text{GN}}, g_{\text{Th}}; \eta, 1](\mathfrak{s}) - {}_{1/2}B^{\mathfrak{u}}[g_{\text{Th}}, g_{\text{Th}}; \eta, 1](\mathfrak{s}), \quad (\text{B.44b}) \\
\rho^{\eta}[g, \eta](p^2) &:= \eta(p^2) - \Sigma^1[g_{\text{GN}}; \eta, 1](p^2) + \Sigma^1[g_{\text{Th}}; \eta, 1](p^2). \quad (\text{B.44c})
\end{aligned}$$

Substituting truncated series of Chebyshev rational functions of the form (3.47) for all three unknown functions and evaluating on the associated collocation grids, we obtain the residual vectors $\rho^{g_{\text{GN}}}(\mathbf{g}_{\text{GN}}, \mathbf{g}_{\text{Th}}, \eta)$, $\rho^{g_{\text{Th}}}(\mathbf{g}_{\text{GN}}, \mathbf{g}_{\text{Th}}, \eta)$, and $\rho^{\eta}(\mathbf{g}_{\text{GN}}, \mathbf{g}_{\text{Th}}, \eta)$ for the Chebyshev coefficient vector $(\mathbf{g}_{\text{GN}}, \mathbf{g}_{\text{Th}}, \eta)$. We point out that some diagrams, *e.g.* ${}^*B_{\leftrightarrow}^{\mathfrak{s}1}[g_{\text{GN}}, g_{\text{Th}}; \eta, 1]$, enter both $\rho^{g_{\text{GN}}}$ and $\rho^{g_{\text{Th}}}$, so that it is beneficial to compute these residuals simultaneously for a given collocation point. To exploit this fact, the expansion orders of g_{GN} and g_{Th} need to agree, which we will always assume here. The Jacobian corresponding to the residual vector $\rho = (\rho^{g_{\text{GN}}}, \rho^{g_{\text{Th}}}, \rho^{\eta})$,

$$\mathbf{J} = \begin{pmatrix} \mathbf{J}^{g_{\text{GN}}g_{\text{GN}}} & \mathbf{J}^{g_{\text{GN}}g_{\text{Th}}} & \mathbf{J}^{g_{\text{GN}}\eta} \\ \mathbf{J}^{g_{\text{Th}}g_{\text{GN}}} & \mathbf{J}^{g_{\text{Th}}g_{\text{Th}}} & \mathbf{J}^{g_{\text{Th}}\eta} \\ \mathbf{J}^{\eta g_{\text{GN}}} & \mathbf{J}^{\eta g_{\text{Th}}} & \mathbf{J}^{\eta\eta} \end{pmatrix}, \quad (\text{B.45})$$

has components

$$\begin{aligned}
J_{mn}^{g_{\text{GN}}g_{\text{GN}}} &= \left[1 + 2\eta \left(\frac{\mathfrak{s}_m}{2 + 2c_{34}} \right) \right] P_n(\mathfrak{s}_m) + 2\mathfrak{s} P'_n(\mathfrak{s}_m) - {}_{\tilde{N}}B_{\leftrightarrow}^{\mathfrak{s}2}[g_{\text{GN}}, P_n; \eta, 1](\mathfrak{s}_m) \\
&\quad + {}_0B_{\leftrightarrow}^{\mathfrak{s}1}[g_{\text{GN}}, P_n; \eta, 1](\mathfrak{s}_m) + {}_0B_{\leftrightarrow}^{\mathfrak{s}1}[P_n, g_{\text{Th}}; \eta, 1](\mathfrak{s}_m) \\
&\quad + {}_0B_{\leftrightarrow}^{\mathfrak{t}}[P_n, g_{\text{Th}}; \eta, 1](\mathfrak{s}_m) - {}_0B_{\leftrightarrow}^{\mathfrak{u}}[P_n, g_{\text{Th}}; \eta, 1](\mathfrak{s}_m), \quad (\text{B.46a}) \\
J_{mn}^{g_{\text{GN}}g_{\text{Th}}} &= {}_0B_{\leftrightarrow}^{\mathfrak{s}1}[g_{\text{GN}}, P_n; \eta, 1](\mathfrak{s}_m) + {}_0B_{\leftrightarrow}^{\mathfrak{t}}[g_{\text{GN}}, P_n; \eta, 1](\mathfrak{s}_m) + {}_0B_{\leftrightarrow}^{\mathfrak{t}}[g_{\text{Th}}, P_n; \eta, 1](\mathfrak{s}_m) \\
&\quad - {}_0B_{\leftrightarrow}^{\mathfrak{u}}[g_{\text{GN}}, P_n; \eta, 1](\mathfrak{s}_m) + {}_0B_{\leftrightarrow}^{\mathfrak{u}}[g_{\text{Th}}, P_n; \eta, 1](\mathfrak{s}_m) \quad (\text{B.46b})
\end{aligned}$$

$$\begin{aligned}
J_{mn}^{g_{\text{GN}}\eta} &= 2P_n \left(\frac{\mathfrak{s}_m}{2 + 2c_{34}} \right) g_{\text{GN}}(\mathfrak{s}_m) - {}_{\tilde{N}}B_{\leftrightarrow}^{\mathfrak{s}2}[g_{\text{GN}}, g_{\text{GN}}; P_n, 0](\mathfrak{s}_m) \\
&\quad + {}_0B_{\leftrightarrow}^{\mathfrak{s}1}[g_{\text{GN}}, g_{\text{GN}}; P_n, 0](\mathfrak{s}_m) + {}_0B_{\leftrightarrow}^{\mathfrak{s}1}[g_{\text{GN}}, g_{\text{Th}}; P_n, 0](\mathfrak{s}_m) \\
&\quad + {}_0B_{\leftrightarrow}^{\mathfrak{t}}[g_{\text{GN}}, g_{\text{Th}}; P_n, 0](\mathfrak{s}_m) + {}_0B_{\leftrightarrow}^{\mathfrak{t}}[g_{\text{Th}}, g_{\text{Th}}; P_n, 0](\mathfrak{s}_m) \\
&\quad - {}_0B_{\leftrightarrow}^{\mathfrak{u}}[g_{\text{GN}}, g_{\text{Th}}; P_n, 0](\mathfrak{s}_m) + {}_0B_{\leftrightarrow}^{\mathfrak{u}}[g_{\text{Th}}, g_{\text{Th}}; P_n, 0](\mathfrak{s}_m) \quad (\text{B.46c})
\end{aligned}$$

$$\begin{aligned}
J_{mn}^{g_{\text{Th}}g_{\text{GN}}} &= - {}_{-1}B_{\leftrightarrow}^{\mathfrak{s}1}[P_n, g_{\text{Th}}; \eta, 1](\mathfrak{s}_m) + {}_{1/2}B_{\leftrightarrow}^{\mathfrak{t}}[g_{\text{GN}}, P_n; \eta, 1](\mathfrak{s}_m) + {}_{-1/2}B_{\leftrightarrow}^{\mathfrak{t}}[P_n, g_{\text{Th}}; \eta, 1](\mathfrak{s}_m) \\
&\quad - {}_{1/2}B_{\leftrightarrow}^{\mathfrak{u}}[g_{\text{GN}}, P_n; \eta, 1](\mathfrak{s}_m) + {}_{-1/2}B_{\leftrightarrow}^{\mathfrak{u}}[P_n, g_{\text{Th}}; \eta, 1](\mathfrak{s}_m) \quad (\text{B.46d})
\end{aligned}$$

$$\begin{aligned}
J_{mn}^{g_{\text{Th}}g_{\text{Th}}} &= \left[1 + 2\eta \left(\frac{\mathfrak{s}_m}{2 + 2c_{34}} \right) \right] P_n(\mathfrak{s}_m) + 2\mathfrak{s}_m P'_n(\mathfrak{s}_m) + {}_{-\tilde{N}}B_{\leftrightarrow}^{\mathfrak{s}2}[g_{\text{Th}}, P_n; \eta, 1](\mathfrak{s}_m) \\
&\quad - {}_{-1}B_{\leftrightarrow}^{\mathfrak{s}1}[g_{\text{GN}}, P_n; \eta, 1](\mathfrak{s}_m) + {}_{-2}B_{\leftrightarrow}^{\mathfrak{s}1}[g_{\text{Th}}, P_n; \eta, 1](\mathfrak{s}_m) + {}_{-1/2}B_{\leftrightarrow}^{\mathfrak{t}}[g_{\text{GN}}, P_n; \eta, 1](\mathfrak{s}_m) \\
&\quad + {}_{1/2}B_{\leftrightarrow}^{\mathfrak{t}}[g_{\text{Th}}, P_n; \eta, 1](\mathfrak{s}_m) + {}_{-1/2}B_{\leftrightarrow}^{\mathfrak{u}}[g_{\text{GN}}, P_n; \eta, 1](\mathfrak{s}_m) - {}_{1/2}B_{\leftrightarrow}^{\mathfrak{u}}[g_{\text{Th}}, P_n; \eta, 1](\mathfrak{s}_m) \quad (\text{B.46e})
\end{aligned}$$

$$\begin{aligned}
J_{mn}^{g_{\text{Th}}\eta} &= 2P_n \left(\frac{\mathfrak{s}_m}{2 + 2c_{34}} \right) g_{\text{Th}}(\mathfrak{s}_m) + {}_{-\tilde{N}}B_{\leftrightarrow}^{\mathfrak{s}2}[g_{\text{Th}}, g_{\text{Th}}; P_n, 0](\mathfrak{s}_m) \\
&\quad - {}_{-1}B_{\leftrightarrow}^{\mathfrak{s}1}[g_{\text{GN}}, g_{\text{Th}}; P_n, 0](\mathfrak{s}_m) + {}_{-2}B_{\leftrightarrow}^{\mathfrak{s}1}[g_{\text{Th}}, g_{\text{Th}}; P_n, 0](\mathfrak{s}_m) \\
&\quad + {}_{1/2}B_{\leftrightarrow}^{\mathfrak{t}}[g_{\text{GN}}, g_{\text{GN}}; P_n, 0](\mathfrak{s}_m) + {}_{-1/2}B_{\leftrightarrow}^{\mathfrak{t}}[g_{\text{GN}}, g_{\text{Th}}; P_n, 0](\mathfrak{s}_m) + {}_{1/2}B_{\leftrightarrow}^{\mathfrak{t}}[g_{\text{Th}}, g_{\text{Th}}; P_n, 0](\mathfrak{s}_m) \\
&\quad - {}_{1/2}B_{\leftrightarrow}^{\mathfrak{u}}[g_{\text{GN}}, g_{\text{GN}}; P_n, 0](\mathfrak{s}_m) + {}_{-1/2}B_{\leftrightarrow}^{\mathfrak{u}}[g_{\text{GN}}, g_{\text{Th}}; P_n, 0](\mathfrak{s}_m) - {}_{1/2}B_{\leftrightarrow}^{\mathfrak{u}}[g_{\text{Th}}, g_{\text{Th}}; P_n, 0](\mathfrak{s}_m) \quad (\text{B.46f})
\end{aligned}$$

$$J_{mn}^{\eta g_{\text{GN}}} = -\Sigma^1[P_n; \eta, 1](p_m^2) \quad (\text{B.46g})$$

$$J_{mn}^{\eta g_{\text{Th}}} = \Sigma^1[P_n; \eta, 1](p_m^2) \quad (\text{B.46h})$$

$$J_{mn}^{\eta\eta} = P_n(p_m^2) - \Sigma^1[g_{\text{GN}}; P_n, 0](p_m^2) + \Sigma^1[g_{\text{Th}}; P_n, 0](p_m^2). \quad (\text{B.46i})$$

Here again, some diagrams occur in both g_{GN} and g_{Th} components, so that these should be computed at one go.

Critical exponents. To extract the spectrum of a fixed point solution, we solve the algebraic eigenvalue equation (4.12). The Jacobians $\mathbf{J}_{A,B}$ are obtained from $\mathbf{J}^{g_A g_B}$ in (B.46) by replacing $P_n(\mathfrak{s}) \longrightarrow (\mathfrak{s} + L)^{a_{\max}} P_n(\mathfrak{s})$. The matrix \mathbf{P} was given in (3.57).

C

Chebyshev functions and the pseudospectral method

The Chebyshev polynomials and their relatives provide orthogonal basis sets for specific \mathcal{L}^2 spaces and are powerful and versatile tools in approximation theory. Here we will collect the main properties relevant for the expansions and methods used in this thesis. Comprehensive overviews of Chebyshev functions and their use in approximation theory can be found, *e.g.*, in Refs. [105, 113].

C.1 Chebyshev polynomials of the first kind

Definition. The Chebyshev polynomials of the first kind are denoted by T_n , $n = 0, 1, \dots$, and defined on the interval $[-1, 1]$ by the recurrence relation

$$T_0(x) = 1, \tag{C.1a}$$

$$T_1(x) = x, \tag{C.1b}$$

$$T_{n+1}(x) = 2x T_n(x) - T_{n-1}(x). \tag{C.1c}$$

Expansions in terms of the T_n are closely related to Fourier cosine series owing to the relation

$$T_n(\cos \theta) = \cos(n\theta). \tag{C.2}$$

However, contrary to the cosine series, the use of Chebyshev polynomials as an expansion basis is not restricted to even and/or periodic functions.

Orthogonality and completeness. The expansion of arbitrary functions in terms of Chebyshev polynomials of the first kind is based on the completeness property in the space $\mathcal{L}^2([-1, 1])$ with measure $dx/\sqrt{1-x^2}$, *i.e.* the space of functions $f : [-1, 1] \rightarrow \mathbb{R}$ that are square-integrable with respect to that measure [113]. Indeed, any such function can be expanded as a series

$$f(x) = \sum_{n=0}^{\infty} f_n T_n(x) \tag{C.3}$$

that converges with respect to the norm

$$\|f\|^2 = \int_{-1}^1 \frac{dx}{\sqrt{1-x^2}} |f(x)|^2. \tag{C.4}$$

Such an expansion is particularly convenient due to the orthogonality property

$$\int_{-1}^1 \frac{dx}{\sqrt{1-x^2}} T_m(x) T_n(x) = \frac{\pi}{c_m} \delta_{mn}, \tag{C.5}$$

where $c_0 = 1$ and $c_{\geq 1} = 2$. Taking the inner product of T_n with the ansatz (C.3) then allows us to extract the coefficients,

$$f_n = \frac{c_n}{\pi} \int_{-1}^1 \frac{dx}{\sqrt{1-x^2}} T_n(x) f(x). \tag{C.6}$$

Clenshaw algorithm. A fast and stable way to compute the value of a Chebyshev series (C.3) truncated at some order n_{\max} is the Clenshaw algorithm [129]. We recursively define the auxiliary coefficients

$$b_{n_{\max}+1} := b_{n_{\max}+2} := 0 \tag{C.7}$$

$$b_n := f_n + 2x b_{n+1}(x) - b_{n+2} \quad (n = n_{\max}, \dots, 1) \tag{C.8}$$

using the Chebyshev coefficients f_n and the evaluation point x . The value of the truncated series at x is then given by

$$\sum_{n=0}^{n_{\max}} f_n T_n(x) = f_0 + b_1 x - b_2. \tag{C.9}$$

Approximation theory and the Galerkin method. A standard problem of approximation theory is to find a function f , *w.l.o.g.* defined on $[-1, 1]$, that satisfies the equation $\rho[f] = 0$ for a given residual functional ρ . In general, this functional may involve algebraic as well as differential and/or integral operations of the argument function. If the solution function f is in $\mathcal{L}^2([-1, 1])$, we should be able to expand it as a series (C.3). Using this ansatz for f and truncating the series at some maximum order n_{\max} reduces the functional equation $\rho[f] = 0$ to an approximated form

$$\rho(f_0, \dots, f_{n_{\max}}; x) := \rho \left[\sum_{n=0}^{n_{\max}} f_n T_n \right] (x) \stackrel{!}{=} 0, \quad x \in [-1, 1]. \quad (\text{C.10})$$

The idea of the Galerkin method is to expand the residual function $\rho(f; x)$ itself as a (truncated) Chebyshev series. Since the residual is to vanish on the whole interval, all its expansion coefficients need to vanish. Using Eq. (C.6) for the coefficients of ρ leads to the defining relation of the Galerkin method,

$$\int_{-1}^1 \frac{dx}{\sqrt{1-x^2}} T_n(x) \rho(f; x) \stackrel{!}{=} 0, \quad n = 0, \dots, n_{\max}. \quad (\text{C.11})$$

This algebraic system of $(n_{\max} + 1)$ equations for the $(n_{\max} + 1)$ unknown coefficients $f_0, \dots, f_{n_{\max}}$ can then be solved by an appropriate method depending on the type of equations.

Pseudospectral method and collocation grids. For the pseudospectral method, the expansion coefficients f_n are approximated by enforcing the residual of f to vanish on a set of discrete points $x_0, x_1, \dots, x_{n_{\max}}$, where n_{\max} is again the maximum order of the truncated series (C.3). The resulting approximating series thus interpolates the function f between these so-called collocation points and converges to the true function on the entire domain as $n_{\max} \rightarrow \infty$ [105]. Popular choices for the collocation points are the roots of $T_{n_{\max}+1}$,

$$x_m = -\cos \left(\frac{(2m+1)\pi}{2(n_{\max}+1)} \right), \quad (\text{C.12a})$$

or its extrema supplemented by the interval end points (*Gauss-Lobatto grid*),

$$x_m = -\cos \left(\frac{m\pi}{n_{\max}} \right). \quad (\text{C.12b})$$

Both options can be shown to satisfy an optimum convergence property because they correspond to the Galerkin method for numerical integration of the inner products (C.11) using an optimum Gauss quadrature rule [105].

C.2 Chebyshev polynomials of the second kind

Definition. For completeness, we note that there exists a second set of orthogonal polynomials on $[-1, 1]$, denoted by U_n , $n = 0, 1, \dots$, called the Chebyshev polynomials of the second kind. These are defined by the recurrence relation

$$U_0(x) = 1, \quad (\text{C.13a})$$

$$U_1(x) = 2x, \quad (\text{C.13b})$$

$$U_{n+1}(x) = 2x U_n(x) - U_{n-1}(x). \quad (\text{C.13c})$$

They are, however, very rarely used as an expansion basis to approximate arbitrary functions.

C.3 Chebyshev rational functions

Definition. In order to expand functions in \mathcal{L}^2 on the semi-infinite interval $[0, \infty)$, we can compactify the domain to $[-1, 1]$ and use the Chebyshev polynomials of the first kind. This leads to the definition of the Chebyshev rational functions

$$R_n(x) = T_n \left(\frac{x-L}{x+L} \right), \quad n = 0, 1, \dots \quad (\text{C.14})$$

Here L is a free real parameter that should roughly reflect the typical length scale of the function to be expanded. The corresponding \mathcal{L}^2 measure is transformed to $dx \sqrt{L/x}/(x+L)$.

Orthogonality. The orthogonality relation for the Chebyshev rational functions follows from the relation (C.5) for the polynomials of the first kind:

$$\int_0^\infty dx \sqrt{\frac{L}{x}} \frac{R_m(x)R_n(x)}{x+L} = \frac{\pi}{c_m} \delta_{mn}. \quad (\text{C.15})$$

Likewise, the orthogonality property can be used to compute the expansion coefficients of a function $f \in \mathcal{L}^2([0, \infty))$ as

$$f_n = \frac{c_n}{\pi} \int_0^\infty dx \sqrt{\frac{L}{x}} \frac{R_n(x)f(x)}{x+L}. \quad (\text{C.16})$$

Finding approximate solutions to equations on $[0, \infty)$ by means of the Galerkin or pseudospectral methods then works completely analogously to the case of Chebyshev polynomials described above.

Collocation grids. Optimal collocation grids are derived from (C.12) by reversing the domain compactification, *i.e.*

$$x_m = L \frac{1 + \hat{x}_m}{1 - \hat{x}_m}, \quad (\text{C.17})$$

where the \hat{x}_m are given by either (C.12a) or (C.12b). Since the latter involves $x_{n_{\max}} = \infty$ as an expansion point, the roots grid (C.12a) is a far more common choice. If we use the square-root parametrization (*cf.* Section 3.5) for our expansion series, *i.e.* $f(y) = \sum_n f_n R_n(\sqrt{y})$, the collocation grid has to be adapted, namely $y_m = x_m^2$.

D Newton-Raphson iteration

The Newton-Raphson procedure is a standard algorithm to iteratively find a solution of an arbitrary system of algebraic equations [130, 131]. Starting from an initial guess, it uses linear approximations to the system's residual function to gradually improve the solution.

Definitions. Consider a system of n variables x_i , collectively denoted by $\mathbf{x} = (x_1, \dots, x_n)$. We are looking for a solution \mathbf{x}_* that satisfies the n equations

$$\rho_i(\mathbf{x}_*) = 0 \quad (i = 1, \dots, n). \quad (\text{D.1})$$

The functions ρ_i are called *residuals*, and we also define the residual vector $\boldsymbol{\rho} = (\rho_1, \dots, \rho_n)$. Assuming that the residual functions are analytic in a neighborhood of the solution, we can expand for \mathbf{x} sufficiently close to \mathbf{x}_* and obtain

$$0 = \boldsymbol{\rho}(\mathbf{x}_*) = \boldsymbol{\rho}(\mathbf{x}) + \mathbf{J}(\mathbf{x})(\mathbf{x}_* - \mathbf{x}) + \mathcal{O}((\mathbf{x}_* - \mathbf{x})^2), \quad (\text{D.2})$$

where the *Jacobian* $\mathbf{J} = (J_{mn})$ is given by

$$J_{ij}(\mathbf{x}) = \frac{\partial \rho_i}{\partial x_j}(\mathbf{x}). \quad (\text{D.3})$$

Multiplying by its inverse and rearranging terms, we find

$$\mathbf{x}_* = \mathbf{x} - \mathbf{J}(\mathbf{x})^{-1} \boldsymbol{\rho}(\mathbf{x}) + \mathcal{O}((\mathbf{x}_* - \mathbf{x})^2). \quad (\text{D.4})$$

This relation forms the basis of the Newton-Raphson iteration. If the initial guess is close to the true solution, the remainder is small. Neglecting it thus leads to a new and hopefully improved guess.

Iteration procedure. The introductory considerations may be formalized as an algorithm that systematically tries to decrease the residual vector $\boldsymbol{\rho}$:

1. let $k := 0$ and define an initial guess $\mathbf{x}^{(0)}$;
2. compute the residual and Jacobian of the current guess:

$$\boldsymbol{\rho}^{(k)} := \boldsymbol{\rho}(\mathbf{x}^{(k)}), \quad (\text{D.5})$$

$$\mathbf{J}^{(k)} := \mathbf{J}(\mathbf{x}^{(k)}); \quad (\text{D.6})$$

3. compute a new guess

$$\mathbf{x}^{(k+1)} := \mathbf{x}^{(k)} - [\mathbf{J}^{(k)}]^{-1} \boldsymbol{\rho}^{(k)}; \quad (\text{D.7})$$

4. check for convergence: if the increment $\Delta \mathbf{x} = \mathbf{x}^{(k+1)} - \mathbf{x}^{(k)}$ and/or the residual $\boldsymbol{\rho}^{(k+1)}$ lie below a certain threshold, return $\mathbf{x}^{(k+1)}$; otherwise, let $k := k + 1$ and resume with step 2.

Possible exit conditions involve a threshold for the absolute and/or relative errors of the step size,

$$|x_i^{(k+1)} - x_i^{(k)}| < \Delta_{\text{abs}} + \Delta_{\text{rel}} |x_i^{(k)}| \quad \text{for all } i = 1, \dots, n, \quad (\text{D.8})$$

or of the residual vector,

$$|\rho_i^{(k+1)} - \rho_i^{(k)}| < \Delta_{\text{abs}} + \Delta_{\text{rel}} |\rho_i^{(k)}| \quad \text{for all } i = 1, \dots, n. \quad (\text{D.9})$$

The latter should only be used when it is sufficient to obtain an approximate solution of equations (D.1). In case that the Jacobian is not accessible analytically or its evaluation is computationally demanding, it can be calculated numerically from the residual function:

$$J_{ij}(\mathbf{x}) \simeq \frac{\rho_i(x_1, \dots, x_{j-1}, (1 + \varepsilon)x_j, x_{j+1}, \dots, x_n) - \rho_i(\mathbf{x})}{\varepsilon x_j}, \quad (\text{D.10})$$

where ε is some small number, for instance the square root of the machine precision [119].

Convergence. Of course, the Newton-Raphson algorithm can only find one solution at a time even though the original system (D.1) may have multiple solutions. Moreover, since the algorithm essentially uses a linear approximation of the residual function in every step, the initial guess needs to be sufficiently close to a solution in order for the iteration to converge. If this is the case, we usually have quadratic convergence [131], every additional iteration doubles the accuracy of the solution (*i.e.* the number of correct decimal places). Of course, natural limitations are set by the precision of the applied floating point type. Consequently, if the computation of residual and Jacobian involves many and/or complicated operations, such that rounding errors accumulate, convergence will generally become worse.

In practice, it may be computationally advantageous to compute the Jacobian numerically using, *e.g.*, finite differences (*cf.* Appendix B.5). Then again, this will usually slow down convergence and limit the achievable precision. Another approach to circumvent these problems is automatic differentiation [132], whereby residuals and Jacobian are computed simultaneously in each iteration step.

E Remarks on the source code

For the solution of fixed point equations and critical exponents for finite flavor numbers, we wrote a C++ program, whose source code is included in the digital submission of this thesis. This appendix serves as a quick introduction to the implementation.

The program is called **GNPFCheb** (Gross-Neveu, Purely Fermionic, Chebyshev expansions) and all source files are located in the **GNPFCheb** folder. It uses two auxiliary libraries *dwmisc* and *dwamf* written by the author, whose source files are also provided in the respective folders. Moreover, it requires the *GNU Scientific Library* (including BLAS) [119], the *Eigen3* library [120], and the *CUBA* library [115–118] (cf. Section E.2).

E.1 Compiling and running the program

Compiling. Before compiling the program, the following paths in the *Makefiles* of *dwamf* and **GNPFCheb** should be set:

`CUBA_DIR`: points to the root directory of the *CUBA* library;

`DWAMF_DIR`: points to the root directory of the *dwamf* library (only in the *Makefile* for **GNPFCheb**);

`DWMISC_DIR`: points to the root directory of the *dwmisc* library.

To compile the program, change to the **GNPFCheb** directory and use `make`. This will subsequently call `make` for the *dwmisc* and *dwamf* libraries, too. Upon success, it will create an executable file **GNPFCheb** in the current directory.

Running. To run the program after compilation, open a terminal, change to the **GNPFCheb** directory and type `./GNPFCheb`. This will start the program with the built-in configuration values unless there is a configuration file `default.cfg` in the same directory. You can also specify a different configuration file as a command-line argument, *e.g.* `./GNPFCheb myconfig.cfg` or read and write configuration values from the command prompt using the `get` and `set` commands. For a list of configuration values, see the next paragraph.

After successfully loading the modules, the program will present you with a command prompt, indicated by the ‘>’ symbol. From here, the various input/output routines, fixed point and eigenvalue solvers, *etc.* can be called using the interactive computing script interface (ICSI) of the *dwamf* library (see Section E.2). For a list of commands, see Section E.4.

Configuration values. The following configuration values may be set:

`AbsoluteErrorGoal`: target absolute error for numerical integrations;

`ChebEx-eta-L`: compactification scale L for Chebyshev rational function expansions of the anomalous dimension functions (cf. Eq. (3.46));

`ChebEx-eta-order`: order n_{\max} of the Chebyshev rational function expansions of the anomalous dimension functions (cf. Eq. (3.47));

`ChebEx-g-L`: compactification scale L for Chebyshev rational function expansions of the coupling functions (cf. Eq. (3.46));

`ChebEx-g-order`: order n_{\max} of the Chebyshev rational function expansions of the coupling functions (cf. Eq. (3.47));

`ChebEx-g-orderL`: order n_{\max}^L of the Chebyshev polynomial expansions of the coupling functions on the left-hand patch of the domain (not used in this thesis);

`ChebEx-g-orderR`: order n_{\max}^R of the Chebyshev rational function expansions of the coupling functions on the right-hand patch of the domain (not used in this thesis);

ChebEx-g-param: default parametrization for Chebyshev rational function expansions of the coupling functions (options: `id`, `sqrt`, `4rt`);

ChebEx-g-sLink: patch link \hat{s} of the Chebyshev expansions of the coupling functions in a two-patch split of the domain (not used in this thesis);

DataDirectory: default directory for input/output of data;

DimGamma: dimension d_γ of the Clifford algebra representation, should be either 2 or 4;

gFPPert-Asymptotic-Exponent: asymptotic scaling exponent a_{\max} in the constant asymptotics scheme (*cf.* Eq. (3.55));

MaxEvaluations: maximum number of sample points for numerical integrations;

Model: the default model to use for computations (see Section E.3 for a list of available models);

MomentumConfiguration-beta: angle between the xy -plane projections of p_3 and p_4 of the chosen momentum configuration;

MomentumConfiguration-c34: cosine of the angle between p_3 and p_4 of the chosen momentum configuration;

NumFlavors: flavor number N_f ;

PlotMaxV: maximum p^2 value for plots of coupling and anomalous dimension functions;

PrecisionGoal: target relative error for numerical integrations;

Root-AbsoluteErrorGoal: target absolute error for algebraic numerical solvers;

Root-MaxIterations: maximum number of iterations for iterative algebraic numerical solvers;

Root-MaxNoResidualDecrease: maximum number of iterations without a decrease of the maximum residual for iterative algebraic numerical solvers;

Root-RelativeErrorGoal: target relative error for algebraic numerical solvers;

Root-Solver: numerical solver type for algebraic equations (standard: `newton`).

E.2 Auxiliary libraries

The *GNPFCheb* program uses five external auxiliary libraries, three of which are publicly available: the *GNU Scientific Library* (including BLAS) [119], the *Eigen3* library [120], and the *CUBA* library [115–118]. Usage was indicated in the main text already. The *GSL* library is used for the solution of algebraic eigensystems and by some routines of the *dwmisc* and *dwamf* libraries. The *Eigen3* library is likewise used for solving algebraic eigenvalue problems and for certain data containers. The *CUBA* library provides the Cuhre algorithm which is used for multidimensional numerical integrations. For details on these software packages, we refer to the official documentations cited above.

dwmisc. The *dwmisc* library is a small C library, whose source files may be found in the corresponding *dwmisc* folder. It provides basic input/output routines (`dataio.*`), a *gnuplot* [133] interface (`plot.*`), wrappers for random number generators (`random.*`), basic statistics (`statistics.*`), and some other utilities. It is mostly used by some of the *dwamf* components and not explicitly referenced from within *GNPFCheb*.

dwamf. The *dwamf* library is a collection of C++ auxiliary structures and routines for standard mathematical problems such as integration, numerical solution of equations, special functions, plotting, *etc.* Its aim is mostly to provide a unified framework to standard tools found in other software packages. The source files are located in the `dwamf` directory.

In the following, we shortly describe the various submodules, but do not go into details of the implementation:

```

conf/
    manages configuration files to be loaded from and saved to disk, implemented internally as
    a key-value hash map.

data/
    provides routines for data input/output and manipulation.

func/
    provides an abstract mathematical function framework (Function.*pp and derived classes,
    Domain.*pp and derived classes) as well as special functions (in particular Chebyshev series,
    functions.*pp).

icsi/
    contains the interactive computing script interface (ICSI, cf. Section E.4).

nint/
    provides various numerical integration schemes and an abstract framework (Integrator.*pp).

nint/
    provides various numerical solvers for systems of algebraic equations and an abstract frame-
    work (AlgebraicSolver.*pp).

plot/
    contains an object-oriented plotting interface to gnuplot [133].

util/
    contains other auxiliary functions and classes.

```

E.3 File structure

Here we will give an overview of the source file structure in the `GNPFCheb` directory and shortly explain the components defined in the respective files. For more details, please refer to the source code directly.

`GNPFCheb.cpp`

is the program's main file containing the entry point `main`. The program is organized in several modules corresponding to the various models and approximations, all of which may be loaded independently in the main file `GNPFCheb.cpp`. The individual model constituents are stored in folders `model-*` and all contain a file `main.cpp` that is to be `#included` by `GNPFCheb.cpp` in order to load the model.

Apart from that, the main file loads a few other definitions shared by all models, namely definitions of the diagram functionals, coupling and anomalous dimension function containers, regulators, and other utilities.

`diagram-functions/`

contains definitions of the diagram functionals for different approximations.

`dgrf_s.cpp`

s -channel approximation

`dgrf_sAtu.cpp`

s - and averaged t/u -channel approximation

```

dgrf_sAtx.cpp
  s- and averaged t/u-channel approximation with neglected  $\phi$  dependence in the loop
  integrals

kernel.cpp
  definition of the threshold kernel

flow-functions/
  defines containers for Chebyshev rational series of coupling functions (GCouplingFunction*.*pp)
  and anomalous dimension functions (AnomalousDimensionFunction*.*pp). Additionally
  defines wrappers of single Chebyshev rational functions (GChebyshevR*.*pp and
  AnomalousDimensionChebyshevR*.*pp). Finally it also defines classes to specify momentum
  configurations (MomentumConfiguration*.*pp).

model-*/
  contains residual functionals, fixed point solvers, and eigenvalue solvers for a particular model
  and approximation.

Available models:

  gn-s
    Gross-Neveu model, s-channel approximation (old implementation), id: gn/s

  gn-s-rev
    Gross-Neveu model, s-channel approximation (diagram function implementation),
    id: gn/s,rev

  gn-sAtu
    Gross-Neveu model, s- and averaged t/u-channel approximation, id: gn/s,tu

  gn-sAtx
    Gross-Neveu model, s- and averaged t/u-channel approximation with neglected  $\phi$ 
    dependence in the loop integrals, id: gn/s,tx

  gnth-s
    Gross-Neveu-Thirring model, s-channel approximation, id: gnth/s

  gnth-sAtu
    Gross-Neveu-Thirring model, s- and averaged t/u-channel approximation, id: gnth/s,tu

  fixedpoint.cpp
    defines residual and Jacobian functions for the fixed point solver.

  linflow.cpp
    defines routines to compute eigenvalues and -perturbations of the linearized flow equa-
    tion.

  main.cpp
    organizes the module, imports the various components.

  residuals.cpp
    defines residual functionals for fixed point solutions and/or eigenperturbations.

regulators/
  contains definitions of various regulator functions.

  exponential.cpp
    regulator type (1.11)

  exponential_a.cpp
    regulator type (1.12)

  linear.cpp
    regulator type (1.10)

```

```

util/
contains various auxiliary routines.

globals.hpp
defines global constants.

headers.hpp
collects the default header files.

io.*pp
defines methods for data input/output.

params.hpp
defines data structs to be passed to nonspecifying methods taking void* arguments.

plot.*pp
defines plotting routines. Requires gnuplot [133]. 

terminal.cpp
connects the program to the dwamf scripting interface by defining additional commands
that link to program routines.

test.cpp
contains test routines.

types.hpp
defines general data structs used in other classes.

util.*pp
defines further auxiliary routines.

```

E.4 Interactive computing script interface

To access the various modules and routines of the program, we use an interactive computing script interface (ICSI) that allows to control the program flow and connects to the different models and routines of the software. The basic framework is part of the *dwamf* library. Syntax and standard commands are explained in the following paragraphs. Additionally, the **GNPFCheb** program offers extra commands that link to the fixed point and eigenvalue solvers, data I/O, *etc.* These are also listed below.

ICSI interpreter. In this paragraph, we will provide a very short introduction to the ICSI syntax. The basic entity of the language are strings. The ICSI interpreter knows four different parsing modes, *command* (CMD), *string* (STR), *math* (MAT), and *raw* (RAW). Depending on the current mode, the input source is interpreted differently. Comments begin with the # symbol and end at the end of the line, *e.g.*

```
# This is a comment.
```

The default mode is **CMD**. In this mode, the interpreter expects a command and an optional list of arguments, separated from each other by white spaces:

```
<command> <argument1> <argument2> ...
```

The following example calls the command **print** with the arguments *Hello* and *World!*, which will print both arguments to the standard output, separated by a new line:

```
> print Hello World!
Hello
World!
```

Here and in the following, the ‘>’ symbol at the beginning of a line denotes the command prompt, followed by the user’s input. A list of standard commands as well as *GNPFCheb*-specific commands can be found in the next two paragraphs. To enter the CMD mode explicitly from within another mode or to evaluate an argument of another command, enclose the corresponding expression in square brackets [...], *e.g.*

```
> print [equal a a]
(true)
```

Here the command `print` is called with one argument, which is the result of the evaluation of the command `equal` for the arguments `a` and `a`. If you only type a single identifier (without arguments) which does not represent a command, this is interpreted as a string literal/identifier and returned as a value. The following examples illustrates this:

```
> print [break]
> print [break2]
break2
```

In both inputs, the result of the evaluation of the square bracket is printed to the screen. However, in the first input, `break` is a command that returns an empty string, whereas in the second input, `break2` does not name a command and is thus interpreted as an identifier.

The **STR** mode is invoked by enclosing the expression to be parsed as a string in single quotation marks (apostrophe), ‘...’. In particular, this allows you to define string literals containing white spaces. For instance,

```
> print 'Hello World!'
Hello World!
```

You can include the result of a command evaluation in a string by switching to the CMD mode within the string literal:

```
> print 'The result of 3 + 5 is [plus 3 5].'
The result of 3 + 5 is 8.
```

If you want to type a square bracket or an apostrophe within a string literal, use the escape character `\`, which adds the character following after it without interpreting its meaning,

```
> print 'A \'string\' and \[square brackets\] need to be
      escaped by \\.'
A 'string' and [square brackets] need to be escaped by \.
```

An important ingredient of any scripting language are variables. The ICSI command for defining a variable is

```
define <identifier> <expression>
```

This links the given expression to the variable named by the identifier. Note that the command evaluates to the expression itself, allowing to process the value if desired:

```
> print [define a 2]
2
```

To access a variables value in the CMD mode, use the *anchor* `$` followed by the identifier, *e.g.*

```
> print $a
2
> print [plus $a 2]
4
```

Note that in order to redefine the variable, you just use the `define` command with the identifier, without the anchor:

```
> define a 'house'  
> print $a  
house
```

If you dereference a variable using the anchor instead, the *variable value* will be interpreted as the identifier for another variable, *i.e.*

```
> define $a 'tree'  
> print $a  
house  
> print $house  
tree
```

In order to insert a variables value inside a string literal, you need to switch to the CMD mode within a string to dereference the variable:

```
> print '$a evaluates to [$a].'  
$a evaluates to house.
```

You can also assign a block of source code to a variable for later evaluation, commonly called a *function* or *method* in programming languages. For example, we can define

```
> define b 10  
> define f 'plus $b 5'
```

As of now, this simply assigns the string *plus \$b 5* to the variable *f*. To use a string as input to the ICSI interpreter and evaluate it, use the command

```
evaluate <string>
```

In the above example,

```
> print [evaluate $f]  
15
```

If you change the value of the variable *b*, the evaluation value of *f* will change accordingly:

```
> define b 3  
> print [evaluate $f]  
8
```

Quite often, you may want to have delayed evaluations within the function body. For instance, we could try to rewrite the above definition of *f* so that it automatically prints out the result,

```
> define f 'print [plus $b 5]'  
> evaluate $f  
8
```

However, if we now change the value of *b*, this change will not be reflected in *f*:

```
> define b 10  
> evaluate $f  
8
```

The reason is that the expression in square brackets in the definition of *f* above was evaluated before assigning the value to the identifier *f*, thus the argument given to the `print` command is stuck at 8. To achieve the desired effect, we have to define the value given to *f* as a raw string, bringing the RAW mode into play.

To enter the **RAW** mode, enclose the expression in braces `{...}`. In the raw mode, no subexpressions will be evaluated and the contents will just be parsed as a single string literal. Nevertheless, the parser does keep track of delimiting characters, *i.e.* if you have CMD or STR mode code denoted by `'...'` or `[...]` inside, these will be treated as a single subentity. For our example above, the function `f` is thus better defined as

```
> define f {print [plus $b 5]}
```

because now

```
> evaluate $f
15
> define b 20
> evaluate $f
25
```

Similarly to the built-in commands, you can pass arguments to your self-defined methods. The syntax is

```
evaluate <string> <argument0> <argument1> ...
```

The provided arguments will be available within the body of your function as the variables `.0`, `.1`, *etc.* Note that the numbering starts at 0. Consider the following example:

```
> define printDoubleDifference {
(....)      print [times 2 [minus $.0 $.1]]
(....)    }
> evaluate $printDoubleDifference 10 4
12
```

The notation `(...)` here merely indicates that the command extends beyond the line break until the closing right brace is encountered. The function `printDoubleDifference` takes two numbers and prints twice their difference to the screen. In this example, we already silently introduced the concept of local variables. While variables defined in the outermost scope are global and can be accessed from anywhere within the program, you may define local variables within a block that are only valid within the scope of the corresponding `evaluate` environment. To define a variable as local, its identifier must start with a dot `.`, and similarly for dereferencing, *i.e.* `$.local` refers a local variable, whereas `$global` inserts the value of a global variable. For instance, we could then add an intermediate step in the definition of the function `printDoubleDifference` and store the difference of the two arguments in a temporary variable,

```
> define printDoubleDifference {
(....)      define .diff [minus $.0 $.1]
(....)      print [times 2 $.diff]
(....)    }
```

with the same effect. Note that the variable `.diff` is not accessible from outside the function `printDoubleDifference`, *i.e.*

```
> print $.diff
ERROR (runtime) Illegal access: Cannot resolve local variable
in global scope.
```

produces a runtime error. Often times it is convenient to label the arguments passed to a function by more explicit identifiers than just their index. Of course, you could simply define local variables one after another, but there exists a shorthand offered by the command

```
of <identifier0> <identifier1> ...
```

which assigns the value of `.0` to `identifier0`, `.1` to `identifier1`, and so on. Our `printDoubleDifference` function above could thus be written as

```

> define printDoubleDifference {
(... )      of .minuend .subtrahend
(... )      define .diff [minus $.minuend $.subtrahend]
(... )      print [times 2 $.diff]
(... )    }

```

Moreover, expressing arithmetic operations in CMD mode is quite clumsy because the strict “command+arguments” syntax is rather unnatural in this case. This is where the MAT mode comes in handy.

To enter the **MAT** mode, enclose the expression in parentheses (...). The MAT mode syntax is very similar to standard calculator/programming conventions and uses predefined precedence rules such as “multiplication before addition” for evaluation. All commands with a mathematical meaning have an operator equivalent, such as **equal** (=), **plus** (+), **times** (*), *etc.*; *cf.* the list of commands below for an overview. Using the MAT mode, we can simplify the expression for the *printDoubleDifference* function further:

```

> define printDoubleDifference {
(... )      of .minuend .subtrahend
(... )      define .diff ($.minuend - $.subtrahend)
(... )      print (2 * $.diff)
(... )    }

```

Note that in order to enter the MAT mode in a string literal (*i.e.* from the STR mode), you have to switch to the CMD mode first. Hence the above example could be compactified to

```

> print 'The result of 3 + 5 is [(3+5)].'
The result of 3 + 5 is 8.

```

whereas

```

> print 'The result of 3 + 5 is (3+5).'
The result of 3 + 5 is (3+5).

```

Finally, we mention a shorthand notation to evaluate user-defined functions. Instead of the \$-anchor, which returns the value of a variable, you can use the @-anchor, which returns the *evaluated* value of a variable. More precisely, @variable expands to **evaluate** \$variable, *e.g.*

```

> @printDoubleDifference 10 4
12

```

This completes our introduction to the ICSI interpreter. For more examples, please refer to the example scripts in Appendix E.5 for the computation of fixed point solutions and spectra in *GNPFCheb*.

Standard commands. The following commands are available in the default *dwamf* runtime environment. You can get additional information on commands by typing ‘**help <command>**’ in the ICSI prompt.

```

break
Leave the currently executing loop.

define <identifier> <value>
Assign the value to the variable labeled by the identifier.

Alias: def

equal <value1> <value2> /<value>/*
Compare the values for equality. Returns (true) if all values are equal, or an empty string otherwise.

Alias: eq
Math mode: <value1> = <value2> /= <value>/*

```

```

evaluate <block> /<argument>/*
  Evaluate the block for the provided arguments.

  Alias: @

foreach <identifier> <list> <block>
  For each value in the list, set the variable characterized by the identifier to that value and
  evaluate the block.

  Alias: for

help <command>
  Display a help message for the specified command.

  Alias: ?

if <condition> <expression> /elif <condition> <expression> /* /else <expression>/?
```

Evaluation of the expression associated with the first matching condition. If none of the conditions apply, the *else* expression is evaluated if provided, otherwise the result is an empty string.

```

import /<file>/*
  Read in one or more script files and execute their instructions.

integer? /<expression>/*
  Check for each of the provided expressions if it represents an integer number and returns the
  list with non-integer expressions replaced by an empty string.

loop <expression>
  Evaluate the expression iteratively until a break statement occurs.

minus <number1> <number2> /<number>/*
  Take the first number and subtract all subsequent numbers from it.

  Alias: subtract
  Math mode: <number1> - <number2> /- <number>/*

number? /<expression>/*
  Check for each of the provided expressions if it represents a number and returns the list with
  non-number expressions replaced by an empty string.

of /<identifier>/*
  Assign the arguments passed to the current block to the variables specified by the identifiers.

  Alias: label-arguments

plus <number1> <number2> /<number>/*
  Add up the provided numbers.

  Alias: sum
  Math mode: <number1> + <number2> /+ <number>/*

print /<expression>/*
  Print all provided expressions separated by line breaks.

quit
  Exit the script.

  Alias: q

range <number1> <number2> /<number(increment)>/*
  Generate a list of numbers from number1 to number2 by cycling through the list of increments
  or using the default increment 1 if no list is provided.

```

```

times <number1> <number2> /<number>/*
  Multiply the provided numbers.

  Alias: product
  Math mode: <number1> * <number2> /* <number>/*

undefine /<identifier>/+
  Clear the definition of one or more variables and return a list of the previously associated
  values.

  Alias: clear, undef

```

```

unequal <value1> <value2>
  Compare the values and return (true) if they differ, or an empty string if they are equal.

  Alias: neq
  Math mode: <value1> != <value2>

```

GNPFCheb-specific commands. The following commands link the ICSI to the *GNPFCheb* routines for computing and managing fixed point solutions and spectra. They are defined in `util/terminal.cpp`.

```

clfeig /model:<model>/? /type:<parametrization>/?
  Compute eigenperturbations and eigenvalues for the specified or default model in the fixed
  maximum asymptotics scheme with the specified or default parametrization. Requires the
  computation of the corresponding linearized flow matrix (stability matrix) via clfmat be-
  forehand.

```

Alias: `compute-linearized_flow_eigensystem`

```

clfmat /model:<model>/? /type:<parametrization>/? /asymptotics:<asymptotics>/?
  Compute the linearized flow matrix in the fixed maximum asymptotics scheme for the spec-
  ified or default model from the currently loaded fixed point solution. For the eigenpertur-
  bations, the specified or default parametrization is used. The asymptotic prefactor may be
  chosen constant (const), power-law-like (pow, exclusively used in this thesis), or exponential
  (exp).

```

Alias: `compute-linearized_flow_matrix`

```

clfueigpairg /type:<parametrization>/? /from:lambda <number>/?
  /from:eps <perturb>/? /using:precc/?+
  Compute an eigenpair  $(\theta, \epsilon)$  in the running asymptotics scheme, starting from the provided
  initial guesses. The perturbation may be empty (default guess), provided as an index referring
  to a fixed maximum growth scheme solution, or an explicit list of Chebyshev coefficients. If
  the precc option is set, an initial iteration with fixed eigenvalue is performed.

```

Alias: `compute-linearized_flow_unbounded_eigenpair_g`

```

clrlfueigpertg
  Clear the list of eigenperturbations found in the running asymptotics scheme.

```

Alias: `clear-linearized_flow_unbounded_eigenperturbations_g`

```

coeffs <function>
  List the Chebyshev coefficients of a fixed point solution function (g*, v*, or eta*). Al-
  ternatively, list the Chebyshev coefficients of an eigenperturbation (ueps:<index>) or all
  eigenvalues (uspecg) found in the running asymptotics scheme.

```

Alias: `list-coefficients`

```

config
  Print the current configuration.

```

Alias: `print-configuration`

```

evalsln <function> <value>
  Evaluate a solution function at the specified value.

  Alias: evaluate-solution

get <key>
  Get the configuration value associated with the provided key

load /<type>/? <file> /as <alias>/?
  Loads a file according to the specified type. For fixed point solutions, the available types are g*, g*/s,tu, v*, g*/s,tu, eta*. If an alias is given, this will become the identifier for the solution function. To load eigensystems, the types are uspecg for spectra and ueigpertg for eigenperturbations.

  If no type is given, the interpreter tries to guess the file type from the extension. In particular, it supports script files (*.cmd) and configuration files (*.cfg).

  Alias: l

plfeigvalg
  Print eigenvalues obtained in the fixed maximum growth scheme.

plfeigvecg
  Print coefficients of the eigenperturbations obtained in the fixed maximum growth scheme.

plfmatg
  Print the current linearized flow matrix.

plot /<function>/*
  Plot the specified functions. Fixed point solutions are identified as g*, g*/s,tu, v*, g*/s,tu, eta*. Eigenperturbations are identified as ueps:<index>. Residual functions are obtained by a R (absolute) or r (relative) prefix for the above identifiers. Compactification of the domain  $[0, \infty)$  is achieved by a postfix c (currently only supported for residuals).

redirect-output <file>
  Direct the standard output (stdout) to the provided file. Setting the file to * restores the default output.

reexpand /type:<parametrization>/? /from:g* <identifier>/?
  /from:v* <identifier>/? /from:eta* <identifier>/?
  Re-expand a given solution function in terms of the provided parametrization.

  Alias: reex

reset
  Discard all computations and reload the program.

save <type> /<file>/?
  Save the result of a computation to the specified file. If no file is provided, the result will be stored to the current data directory with a file name reflecting the type and properties.

  Types for fixed point solution functions are g*, g*/s,tu, v*, g*/s,tu, eta*. Spectra and eigenperturbations in the fixed maximum growth scheme are addressed by specg, specv, specgv and eigvecg, eigvecgv, respectively. Spectra and eigenperturbations in the running asymptotics scheme are addressed by uspecg and ueigvecg, respectively.

scale <function> <factor>
  Scale the specified solution function by the provided factor.

set <key> <value>
  Set the configuration entry with the given key to the specified value.

  Alias: set-configuration-value

```

```

solve /model:<model>/? /type-g:<parametrization>/? /type-eta:<parametrization>/?

/from:g* <file>/? /from:v* <file>/? /from:eta* <file>/?
Compute a fixed point solution for the specified value in the provided parametrizations and
using the specified initial guesses.

```

If no model or parametrizations are provided, the values of the current configuration are used. If no initial guesses are provided, the currently loaded solutions are used.

Upon success, the newly computed solutions become the current working functions.

E.5 Example scripts

Computation of fixed point solutions. The following script computes a fixed point solution of the Gross-Neveu-Thirring model, starting from an initial guess provided as a source file.

```

1  # Compute fixed point solution
2  # Model: Gross-Neveu-Thirring
3
4  # load initial guesses from files
5  # (file names relative to the current data directory)
6  load g* 'init-guess-gGN.gcf' # gGN*
7  load v* 'init-guess-gTh.gcf' # gTh*
8  load eta* 'init-guess-eta.adf' # eta*
9
10 # define orders of the Chebyshev series
11 # and set their configuration values
12 def orderG 40
13 def orderEta 12
14 set ChebEx-g-order $orderG      # coupling functions
15 set ChebEx-eta-order $orderEta # anomalous dimension
16      function
17
18 # call Newton-Raphson solver:
19 #   - Gross-Neveu-Thirring model, s-channel approximation
20 #   - parametrizations: sqrt for couplings, id for anomalous
21 #     dimensions
22 solve model:gnth/s type-g:sqrt type-eta:id
23
24 # save solutions functions to the current data directory
25 save g* '[get DataDirectory]/gGN-nG[$orderG]-nH[$orderEta].gcf'
26 save v* '[get DataDirectory]/gTh-nG[$orderG]-nH[$orderEta].gcf'
27 save eta* '[get DataDirectory]/eta-nG[$orderG]-nH[$orderEta].adf'

```

Computation of spectra for fixed maximum asymptotic growth. Given a fixed point solution of the Gross-Neveu-Thirring model, the following script automates the computation of spectra in the fixed maximum growth scheme for a series of a_{\max} values.

```

1  # Compute spectra of a fixed point solution
2  # for a series of aMax values
3  # Model: Gross-Neveu-Thirring
4
5  # define parameters of the fixed point solution
6  def fpOrderG 40      # expansion order of couplings
7  def fpOrderEta 12    # expansion order of anomalous dimension

```

```

8  def fpSeries 'recpi' # series identifier
9
10 # define parameters of the perturbation
11 def pertOrder 20 # expansion order of the perturbations
12 def pertParam 'id' # parametrization of the perturbations
13 def aMaxValues '[range 0 20]' # aMax values
14
15 # import fixed point solution
16 # (file names relative to the current data directory)
17 load g* 'gGN-nG[$fpOrderG]-nH[$fpOrderEta]-[$fpSeries].gcf'
18 load v* 'gTh-nG[$fpOrderG]-nH[$fpOrderEta]-[$fpSeries].gcf'
19 load eta* 'eta-nG[$fpOrderG]-nH[$fpOrderEta]-[$fpSeries].adf
,
20
21 # set expansion orders for perturbation
22 set ChebEx-g-order $pertOrder
23
24 # walk through list of aMax values and compute and save
25 # spectra
26 for aMax $aMaxValues {
27     # set current aMax value
28     set gFPPert-Asymptotic-Exponent $aMax
29
30     # compute matrix P^(-1) J
31     clfmat model:gnth/s 'type:[$pertParam]' asymptotics:pow
32     # compute eigensystem
33     clfeig model:gnth/s 'type:[$pertParam]' '
34
35     # save spectrum and eigenvectors in current data
36     # directory
37     save specgv '[get DataDirectory]/spectrum-gv-aMax[$aMax
38         ]-nG[$fpOrderG]fp[$pertOrder]pert-nH[$fpOrderEta]-[
39             $pertParam]-[$fpSeries].dat'
40     save eigvecgv '[get DataDirectory]/eigenvectors-gv-aMax[
41         $aMax]-nG[$fpOrderG]fp[$pertOrder]pert-nH[$fpOrderEta
42         ]-[$pertParam]-[$fpSeries].dat'
43
44 }

```

References

- [1] M. E. Peskin and D. V. Schroeder, *An Introduction to Quantum Field Theory* (Westview Press, 1995).
- [2] J. Zinn-Justin, *Quantum Field Theory and Critical Phenomena*, 3rd ed. (Oxford University Press, 1996).
- [3] A. Sfondrini, *Proceedings, 8th Modave Summer School in Mathematical Physics: Modave, Belgium, August 26-September 1, 2012*, PoS **ModaveVIII**, 005 (2012), arXiv:1210.2262 [hep-th].
- [4] S. Weinberg, in *14th International School of Subnuclear Physics: Understanding the Fundamental Constituents of Matter Erice, Italy, July 23-August 8, 1976* (1976) p. 1.
- [5] M. Niedermaier and M. Reuter, *Living Reviews in Relativity* **9**, 5 (2006).
- [6] D. Griffiths, *Introduction to Elementary Particles* (John Wiley & Sons Inc, 1987).
- [7] F. Wilczek, *2nd International Conference on Particle and Fundamental Physics in Space (SpacePart03) Washington, District of Columbia, December 10-12, 2003*, Nucl. Phys. Proc. Suppl. **134**, 3 (2004), [3(2004)], arXiv:astro-ph/0401347 [astro-ph].
- [8] J. Bardeen, L. N. Cooper, and J. R. Schrieffer, *Phys. Rev.* **108**, 1175 (1957).
- [9] H. T. C. Stoof, eprint arXiv:cond-mat/9910441 (1999), cond-mat/9910441.
- [10] E. Fermi, *Il Nuovo Cimento (1924-1942)* **11**, 1 (2008).
- [11] E. Fermi, *Zeitschrift für Physik* **88**, 161 (1934).
- [12] Y. Nambu and G. Jona-Lasinio, *Phys. Rev.* **122**, 345 (1961).
- [13] Y. Nambu and G. Jona-Lasinio, *Phys. Rev.* **124**, 246 (1961).
- [14] D. J. Gross and A. Neveu, *Phys. Rev.* **D10**, 3235 (1974).
- [15] I. F. Herbut, *Phys. Rev. Lett.* **97**, 146401 (2006).
- [16] S. Hands and C. Strouthos, *Phys. Rev. B* **78**, 165423 (2008).
- [17] I. F. Herbut, V. Juričić, and B. Roy, *Phys. Rev. B* **79**, 085116 (2009).
- [18] W. Wu, Y.-H. Chen, H.-S. Tao, N.-H. Tong, and W.-M. Liu, *Phys. Rev. B* **82**, 245102 (2010).
- [19] L. Janssen and I. F. Herbut, *Phys. Rev. B* **89**, 205403 (2014), arXiv:1402.6277 [cond-mat.str-el].
- [20] L. Classen, I. F. Herbut, L. Janssen, and M. M. Scherer, *Phys. Rev. B* **93**, 125119 (2016), arXiv:1510.09003 [cond-mat.str-el].
- [21] D. V. Khvoshchenko and J. Paaske, *Phys. Rev. Lett.* **86**, 4672 (2001).
- [22] M. Franz, Z. Tešanović, and O. Vafek, *Phys. Rev. B* **66**, 054535 (2002).
- [23] I. F. Herbut, *Phys. Rev. B* **66**, 094504 (2002).
- [24] M. Gomes, R. S. Mendes, R. F. Ribeiro, and A. J. da Silva, *Phys. Rev. D* **43**, 3516 (1991).
- [25] S. Hands and B. Lucini, *Phys. Lett. B* **461**, 263 (1999), arXiv:hep-lat/9906008 [hep-lat].
- [26] L. Rosa, P. Vitale, and C. Wetterich, *Phys. Rev. Lett.* **86**, 958 (2001), arXiv:hep-th/0007093 [hep-th].
- [27] F. Hofling, C. Nowak, and C. Wetterich, *Phys. Rev. B* **66**, 205111 (2002), arXiv:cond-mat/0203588 [cond-mat].
- [28] S. Christofi, S. Hands, and C. Strouthos, *Proceedings, 24th International Symposium on Lattice Field Theory (Lattice 2006): Tucson, USA, July 23-28, 2006*, PoS **LAT2006**, 217 (2006), arXiv:hep-lat/0703016 [HEP-LAT].

[29] S. Christofi, S. Hands, and C. Strouthos, Phys. Rev. **D75**, 101701 (2007), arXiv:hep-lat/0701016 [hep-lat].

[30] J. Braun, H. Gies, and D. D. Scherer, Phys. Rev. **D83**, 085012 (2011), arXiv:1011.1456 [hep-th].

[31] H. Gies and L. Janssen, Phys. Rev. **D82**, 085018 (2010), arXiv:1006.3747 [hep-th].

[32] L. Janssen and H. Gies, Phys. Rev. **D86**, 105007 (2012), arXiv:1208.3327 [hep-th].

[33] B. H. Welleghausen, D. Schmidt, and A. Wipf, (2017), arXiv:1708.01160 [hep-lat].

[34] V. P. Gusynin, S. G. Sharapov, and J. P. Carbotte, Int. J. Mod. Phys. **B21**, 4611 (2007), arXiv:0706.3016 [cond-mat.mes-hall].

[35] A. H. Castro Neto, F. Guinea, N. M. R. Peres, K. S. Novoselov, and A. K. Geim, Rev. Mod. Phys. **81**, 109 (2009).

[36] W. E. Thirring, Annals of Physics **3**, 91 (1958).

[37] C. Luperini and P. Rossi, Annals Phys. **212**, 371 (1991).

[38] B. Rosenstein, H.-L. Yu, and A. Kovner, Phys. Lett. **B314**, 381 (1993).

[39] J. A. Gracey, Int. J. Mod. Phys. **A9**, 567 (1994), arXiv:hep-th/9306106 [hep-th].

[40] J. A. Gracey, Int. J. Mod. Phys. **A9**, 727 (1994), arXiv:hep-th/9306107 [hep-th].

[41] D. K. Hong and S. H. Park, Phys. Rev. **D49**, 5507 (1994), arXiv:hep-th/9307186 [hep-th].

[42] S. Hands, Phys. Rev. D **51**, 5816 (1995).

[43] J. A. Gracey, T. Luthe, and Y. Schroder, Phys. Rev. **D94**, 125028 (2016), arXiv:1609.05071 [hep-th].

[44] L. N. Mihaila, N. Zerf, B. Ihrig, I. F. Herbut, and M. M. Scherer, (2017), arXiv:1703.08801 [cond-mat.str-el].

[45] T. Itoh, Y. Kim, M. Sugiura, and K. Yamawaki, Prog. Theor. Phys. **93**, 417 (1995), arXiv:hep-th/9411201 [hep-th].

[46] M. Sugiura, Progress of Theoretical Physics **97**, 311 (1997), /oup/backfile/content_public/journal/ptp/97/2/10.1143/ptp.97.311/2/97-2-311.pdf.

[47] L. Käkkäinen, Nucl. Phys. B Proc. Suppl. **30**, 670 (1993).

[48] L. Käkkäinen, R. Lacaze, P. Lacock, and B. Petersson, Nucl. Phys. **B415**, 781 (1994), [Erratum: Nucl. Phys. B438, 650 (1995)], arXiv:hep-lat/9310020 [hep-lat].

[49] L. D. Debbio, S. Hands, and J. Mehegan, Nuclear Physics B **502**, 269 (1997).

[50] S. Chandrasekharan and A. Li, Phys. Rev. Lett. **108**, 140404 (2012).

[51] S. Chandrasekharan and A. Li, Phys. Rev. **D88**, 021701 (2013), arXiv:1304.7761 [hep-lat].

[52] L. Wang, P. Corboz, and M. Troyer, New J. Phys. **16**, 103008 (2014), arXiv:1407.0029 [cond-mat.str-el].

[53] Z.-X. Li, Y.-F. Jiang, and H. Yao, New J. Phys. **17**, 085003 (2015), arXiv:1411.7383 [cond-mat.str-el].

[54] S. Hands, JHEP **11**, 015 (2016), arXiv:1610.04394 [hep-lat].

[55] D. Schmidt, B. Welleghausen, and A. Wipf, *Proceedings, 34th International Symposium on Lattice Field Theory (Lattice 2016): Southampton, UK, July 24-30, 2016*, PoS **LAT-TICE2016**, 247 (2016), arXiv:1611.00275 [hep-lat].

[56] A. N. Vasiliev, S. E. Derkachov, N. A. Kivel, and A. S. Stepanenko, Theor. Math. Phys. **94**, 127 (1993), [Teor. Mat. Fiz. 94, 179 (1993)].

[57] A. N. Vasiliev and A. S. Stepanenko, *Theor. Math. Phys.* **97**, 1349 (1993), [*Teor. Mat. Fiz.* 97, 364 (1993)].

[58] W. Chen, Y. Makeenko, and G. W. Semenoff, *Annals Phys.* **228**, 341 (1993), arXiv:hep-th/9301069 [hep-th].

[59] L. Iliesiu, F. Kos, D. Poland, S. S. Pufu, and D. Simmons-Duffin, (2017), arXiv:1705.03484 [hep-th].

[60] D. D. Scherer and H. Gies, *Phys. Rev. B* **85**, 195417 (2012), arXiv:1201.3746 [cond-mat.str-el].

[61] B. Knorr, *Phys. Rev.* **B94**, 245102 (2016), arXiv:1609.03824 [cond-mat.str-el].

[62] M. Salmhofer and C. Honerkamp, *Progress of Theoretical Physics* **105**, 1 (2001), /oup/backfile/content_public/journal/ptp/105/1/10.1143/ptp.105.1/2/105-1-1.pdf .

[63] W. Metzner, M. Salmhofer, C. Honerkamp, V. Meden, and K. Schönhammer, *Rev. Mod. Phys.* **84**, 299 (2012).

[64] Y. Tanizaki, G. Fej  s, and T. Hatsuda, *PTEP* **2014**, 043I01 (2014), arXiv:1310.5800 [cond-mat.quant-gas].

[65] Y. Tanizaki and T. Hatsuda, *Int. J. Mod. Phys.* **E26**, 1740027 (2017), arXiv:1402.0283 [cond-mat.quant-gas].

[66] U. Ellwanger and C. Wetterich, *Nucl. Phys.* **B423**, 137 (1994), arXiv:hep-ph/9402221 [hep-ph].

[67] J. Berges, N. Tetradis, and C. Wetterich, *Phys. Rept.* **363**, 223 (2002), arXiv:hep-ph/0005122 [hep-ph].

[68] H. Gies, *Lect. Notes Phys.* **852**, 287 (2012), arXiv:hep-ph/0611146 [hep-ph].

[69] B. Delamotte, *Lect. Notes Phys.* **852**, 49 (2012), arXiv:cond-mat/0702365 [cond-mat.stat-mech].

[70] P. Kopietz, L. Bartosch, and F. Sch  tz, *Introduction to the Functional Renormalization Group* (Springer Berlin Heidelberg, 2010).

[71] O. J. Rosten, *Phys. Rept.* **511**, 177 (2012), arXiv:1003.1366 [hep-th].

[72] J. Braun, *J. Phys. G: Nucl. Part. Phys.* **39**, 033001 (2012).

[73] M. Fierz, *Helvetica Physica Acta* **12**, 3 (1939).

[74] W. Pauli, *Phys. Rev.* **58**, 716 (1940).

[75] M. Srednicki, *Quantum Field Theory* (Cambridge University Pr., 2007).

[76] J. M. Leinaas and J. Myrheim, *Il Nuovo Cimento B (1971-1996)* **37**, 1 (1977).

[77] F. Wilczek, *Phys. Rev. Lett.* **49**, 957 (1982).

[78] K. Osterwalder and R. Schrader, *Communications in Mathematical Physics* **31**, 83 (1973).

[79] L. P. Kadanoff, *Physics* **2**, 263 (1966).

[80] K. G. Wilson, *Rev. Mod. Phys.* **47**, 773 (1975).

[81] C. Wetterich, *Nuclear Physics B* **352**, 529 (1991).

[82] C. Wetterich, *Phys. Lett. B* **301**, 90 (1993).

[83] D. F. Litim, *Phys. Rev. D* **64**, 105007 (2001), arXiv:hep-th/0103195 [hep-th].

[84] D. F. Litim, *Nucl. Phys. B* **631**, 128 (2002), arXiv:hep-th/0203006 [hep-th].

[85] D. J. Gross and F. Wilczek, *Phys. Rev. Lett.* **30**, 1343 (1973).

[86] H. D. Politzer, *Phys. Rev. Lett.* **30**, 1346 (1973).

- [87] M. Bonini, M. D'Attanasio, and G. Marchesini, Nucl. Phys. B **409**, 441 (1993).
- [88] S. Bornholdt and C. Wetterich, Zeitschrift für Physik C Particles and Fields **58**, 585 (1993).
- [89] T. R. Morris, Int. J. Mod. Phys. A **09**, 2411 (1994).
- [90] R. Alkofer and L. von Smekal, Phys. Rep. **353**, 281 (2001), arXiv:hep-ph/0007355 [hep-ph] .
- [91] F. Benitez, J. P. Blaizot, H. Chate, B. Delamotte, R. Mendez-Galain, and N. Wschebor, Phys. Rev. **E80**, 030103 (2009), arXiv:0901.0128 [cond-mat.stat-mech] .
- [92] J.-P. Blaizot, Phil. Trans. Roy. Soc. Lond. **A369**, 2735 (2011), arXiv:1110.3413 [cond-mat.stat-mech] .
- [93] F. Benitez, J. P. Blaizot, H. Chate, B. Delamotte, R. Mendez-Galain, and N. Wschebor, Phys. Rev. **E85**, 026707 (2012), arXiv:1110.2665 [cond-mat.stat-mech] .
- [94] L. Janssen, *Critical phenomena in (2+1)-dimensional relativistic fermion systems*, Ph.D. thesis, University of Jena (2012).
- [95] F. Gehring, H. Gies, and L. Janssen, Phys. Rev. **D92**, 085046 (2015), arXiv:1506.07570 [hep-th] .
- [96] S. Mandelstam, Phys. Rev. **112**, 1344 (1958).
- [97] R. L. Stratonovich, Soviet Physics Doklady **2**, 416 (1957).
- [98] J. Hubbard, Phys. Rev. Lett. **3**, 77 (1959).
- [99] S. Weinberg, Phys. Rev. **118**, 838 (1960).
- [100] J. P. Fink, J. Math. Phys. **9**, 1389 (1968).
- [101] D. A. Slavnov, Theoretical and Mathematical Physics **17**, 1067 (1973).
- [102] V. A. Smirnov, Commun. Math. Phys. **134**, 109 (1990).
- [103] T. R. Morris, Progress of Theoretical Physics Supplement **131**, 395 (1998), /oup/backfile/content_public/journal/ptps/131/10.1143/ptps.131.395/2/131-395.pdf .
- [104] I. H. Bridle and T. R. Morris, Phys. Rev. D **94**, 065040 (2016).
- [105] J. P. Boyd, *Chebyshev & Fourier Spectral Methods* (Springer, 1989).
- [106] B.-y. Guo, J. Shen, and Z.-q. Wang, International Journal for Numerical Methods in Engineering **53**, 65 (2002).
- [107] J. Borchardt and B. Knorr, Phys. Rev. **D91**, 105011 (2015), [Erratum: Phys. Rev. D93,no.8,089904(2016)], arXiv:1502.07511 [hep-th] .
- [108] M. Heilmann, T. Hellwig, B. Knorr, M. Ansorg, and A. Wipf, JHEP **02**, 109 (2015), arXiv:1409.5650 [hep-th] .
- [109] J. Borchardt and B. Knorr, Phys. Rev. **D94**, 025027 (2016), arXiv:1603.06726 [hep-th] .
- [110] J. Borchardt and A. Eichhorn, Phys. Rev. E **94**, 042105 (2016).
- [111] J. Borchardt, *From Condensed Matter to Higgs Physics – Solving Functional Renormalization Group Equations Globally in Field Space*, Ph.D. thesis, University of Jena (2017).
- [112] B. Knorr, (2017), arXiv:1708.06200 [cond-mat.str-el] .
- [113] J. C. Mason and D. C. Handscomb, *Chebyshev Polynomials* (CRC Press, 2003).
- [114] B. Fornberg, *A Practical Guide to Pseudospectral Methods*, Cambridge Monographs on Applied and Computational Mathematics (Cambridge University Press, 1998).
- [115] T. Hahn, Comput. Phys. Commun. **168**, 78 (2005), arXiv:hep-ph/0404043 [hep-ph] .
- [116] T. Hahn, *Advanced computing and analysis techniques in physics research. Proceedings, 10th International Workshop, ACAT05, Zeuthen, Germany, May 22-27, 2005*, Nucl. Instrum. Meth. **A559**, 273 (2006), arXiv:hep-ph/0509016 [hep-ph] .

- [117] T. Hahn, *Proceedings, 16th International workshop on Advanced Computing and Analysis Techniques in physics (ACAT 14): Prague, Czech Republic, September 1-5, 2014*, J. Phys. Conf. Ser. **608**, 012066 (2015), arXiv:1408.6373 [physics.comp-ph] .
- [118] T. Hahn, “Cuba – a library for multidimensional numerical integration,” official website: <http://www.feynarts.de/cuba/>, accessed: 23/06/2017.
- [119] M. Galassi, J. Davies, *et al.*, *GNU Scientific Library*, version 2.3 ed. (2016), official website: <https://www.gnu.org/software/gsl/>, accessed: 10/02/2017.
- [120] G. Guennebaud, B. Jacob, *et al.*, “Eigen v3,” official website: <http://eigen.tuxfamily.org> (2017), accessed: 21/02/2017.
- [121] K.-i. Kondo, Nucl. Phys. **B450**, 251 (1995), arXiv:hep-th/9502070 [hep-th] .
- [122] W. Armour, S. Hands, and C. Strouthos, Phys. Rev. B **81**, 125105 (2010).
- [123] G. W. Semenoff, Phys. Rev. Lett. **53**, 2449 (1984).
- [124] D. Mesterhazy, J. Berges, and L. von Smekal, Phys. Rev. **B86**, 245431 (2012), arXiv:1207.4054 [cond-mat.str-el] .
- [125] S. Kim and Y. Kim, in *Gravitation and cosmology. Proceedings, Pacific Conference, Seoul, Korea, February 1-6, 1996* (1996) pp. 261–269, arXiv:hep-lat/9605021 [hep-lat] .
- [126] L. Del Debbio and S. J. Hands, Nucl. Phys. **B552**, 339 (1999), arXiv:hep-lat/9902014 [hep-lat] .
- [127] I. M. Barbour, N. Psycharis, E. Focht, W. Franzki, and J. Jersák, Phys. Rev. D **58**, 074507 (1998).
- [128] B. de Wit and J. Smith, *Field Theory in Particle Physics, Volume 1* (Elsevier S&T, 2012).
- [129] C. W. Clenshaw, Math. Comp. **9**, 118 (1955).
- [130] K. E. Atkinson and W. Han, *Theoretical Numerical Analysis: A Functional Analysis Framework*, second, corr. ed. (Springer, 2007).
- [131] P. Deuflhard, *Newton Methods for Nonlinear Problems*, Springer Series in Computational Mathematics, Vol. 35 (Springer Berlin Heidelberg, 2011).
- [132] R. D. Neidinger, SIAM Review **52**, 545 (2010), <https://doi.org/10.1137/080743627> .
- [133] T. Williams, C. Kelley, *et al.*, “Gnuplot 4.6: an interactive plotting program,” <http://www.gnuplot.info/> (2013).